



University
of Glasgow

Emhemmed, Adel Saad (2011) *Performance enhancement of G-band micromachined printed antennas for MMIC integration*. PhD thesis.

<http://theses.gla.ac.uk/2379/>

Copyright and moral rights for this thesis are retained by the author

A copy can be downloaded for personal non-commercial research or study, without prior permission or charge

This thesis cannot be reproduced or quoted extensively from without first obtaining permission in writing from the Author

The content must not be changed in any way or sold commercially in any format or medium without the formal permission of the Author

When referring to this work, full bibliographic details including the author, title, awarding institution and date of the thesis must be given

Performance Enhancement of G-band Micromachined Printed Antennas for MMIC Integration

By

Adel Saad Emhemmed

Thesis submitted in fulfilment of the requirements for
the degree of

Doctor of Philosophy

in

Electronics and Electrical Engineering

at

University of Glasgow



January 2011

© A S Emhemmed, 2011

Abstract

The objective of the work of this thesis is to design, fabricate, and characterise high performance micromachined antennas with fixed and reconfigurable bandwidth. The developed integrated antennas are suitable for MMICs integration at millimetre wave frequencies (G-band) on MMICs technology substrates (i.e GaAs, Si, InP). This work is done through a review of the scientific literature on the subject, and the design, simulation, fabrication and experimental verification, of various suitable designs of antenna.

The novel design of the antennas in this work is based on elevated antenna structures in which the radiator is physically micromachined above the substrate. The antenna design schemes offer a suitable method to integrate an antenna with other MMICs. Further, this method eliminates undesired substrate effects, which degrades the antenna performance drastically. Also in this work we have for the first time realized different micromachined antenna topologies with different novel feeding mechanisms - offering more degrees of freedom for antenna design and enhancing the antenna performance. Experimental and simulation results are provided to demonstrate the effectiveness of the proposed antenna designs and topologies in this work.

A new approach for fabricating printed antennas is introduced in this work to fulfil the fabrication process requirements. It provides a new method for the fabrication of 3-D multilevel structures with variable heights, without etching the substrate. Further, the height of the elevated structures can be specified in the process and can vary by several microns, regardless of the substrate used. This can be used to further enhance the bandwidth and gain of the antenna - avoiding substrate thinning and via holes, and increasing the fabrication yield. Thus, the elevated antenna can meet different application requirements and can be utilized as a substrate independent solution.

In this work we have introduced the concept of reconfigurable antennas at millimetre wave band. Also, we have investigated various aspects associated with lowering the pull-down voltage and overcoming the stiction problem of MEMS switches required for the proposed reconfigurable antennas. This was achieved by developing MEMS technology which can be integrated with MMICs fabrication process. Two novel reconfigurable elevated patch antenna topologies were designed to demonstrate the developed technology and their performances were discussed. The result we obtained from this work demonstrates the feasibility of MEMS reconfigurable printed antennas at G-band frequencies. This will open a new field in MMICs technology and increasing system integration capabilities and functionality.

The devolved technology in this thesis could be utilized in many unique applications including short range high data rate communication systems and high-resolution passive and active millimetre-wave imaging.

Acknowledgments

First and foremost I would like to thank the almighty God (ALLAH) for giving me the knowledge, strength and patience to complete this work. I pray that He continues the same with rest of my life.

I would like to express my profound gratitude and appreciation to Dr. Khaled Elgaid for the consistent help, guidance and attention that he devoted throughout the course of this work. Without his frequent encouragements and useful feedback, this work could not have been realised. Extra special thanks to Prof. Iain Thayne for his helpful advices and feedback.

I would like to give a special thanks to Dr. Ian McGregor for his help reading this thesis and providing excellent comments. I wish to thank the wonderful people in the JWNC for their unlimited technical support: Douglas McIntyre, Stephen Thomas, David Gourlay, Helen Mclelland, Robert Harkins, and Lesley Donaldson. My special thanks to Susan Ferguson for introducing me to fabrication and supervising my first fabricated devices.

My special gratitude goes to my sponsor, the Libyan Embassy in London and the Higher Education Ministry of Libya for giving me the opportunity and the scholarship for my studies.

My special thanks go to my beloved parents for their endless encouragement and prayers throughout the educational years of my life. To my wife and my lovely son and daughter: thank you very much for all your patience, understanding and priceless sacrifices.

Publications

- 1) A. S. Emhemmed, I. McGregor, K. Elgaid, "Elevated Conductor Coplanar Waveguide-fed Three-level Proximity-coupled Antenna for G-band Applications," *Microwaves, Antennas & Propagation, IET*, vol. 4, pp. 1910-1915, Nov. 2010.
- 2) A. S. Emhemmed, I. McGregor, K. Elgaid, "MEMS Printed mm-wave Antenna for G-band Applications", *Fifth Libyan Arab International Conference on Electrical and Electronic Engineering*, Vol. 1, pp. 305-318, October 2010.
- 3) A. S. Emhemmed, K. Elgaid, "Broadband Micromachined Microstrip Patch Antenna for G-band Applications," *39th European Microwave Conference, EuMC 2009*, pp. 374-377, Sept 2009.
- 4) A. S. Emhemmed, I. McGregor, K. Elgaid, "200GHz Broadband Proximity Coupled Patch Antenna," *IEEE International Conference on Ultra-Wideband, ICUB 2009*, pp. 404-407, Sept 2009.
- 5) A. S. Emhemmed, K. Elgaid, "G-band Bowtie Dipole Antenna," *3rd European Conference on Antennas and Propagation, EuCAP 2009*, pp. 998-1000. Mar. 2009.
- 6) A. S. Emhemmed, K. Elgaid, L. B. Lok, "Integrated micromachined millimeter wave patch antenna," *IEEE International Workshop on Antenna Technology, iWAT 2009*, pp. 1-4, Mar. 2009.

Table of Contents

Abstract	ii
Acknowledgments	iv
Publications	v
Table of Contents	vi
List of Figures	x
List of Tables	xv
List of Abbreviation	xvi
Author Declaration	xvii
1. Introduction	1
1.1 Motivation	1
1.3 Research Objectives	6
1.4 Thesis Organization	7
2. Antenna Theory and Background of Printed Antennas	8
2.1 Introduction	8
2.2 Basic Antenna Concept	9
2.3 Antenna Modelling Equations	10
2.4 Antenna Radiation Field	15
2.4.1 Antenna Radiation Field Regions	15
2.4.2 Antenna Radiation Pattern	16
2.5 Antenna Parameters	18
2.5.1 Input Impedance and Return Loss	18
2.5.2 Bandwidth (BW)	19
2.5.3 Directivity	20
2.5.4 Antenna Efficiency	21
2.5.5 Antenna Gain	22
2.5.6 Polarisation	22
2.6 Printed Millimetre-Wave Antennas	24
2.7 Printed Patch Antenna	26

2.7.1 Patch Antenna Excitation.....	27
2.7.2 Impedance Bandwidth Enhancement Techniques.....	31
2.7 Substrate Radiation of Printed Antennas	33
2.8 Micromachining Techniques to Reduce Substrate Effects	36
2.9 Conclusion.....	39
3. Elevated Patch Antennas Analysis and Design Process	40
3.1 Introduction	40
3.2 Integration of Elevated Patch Antennas	41
3.2.1 Analysis Model of Elevated Patch Antenna	43
3.2.2 Matching of Antenna Input Impedance	47
3.3 Design Methodology	50
3.3.1 Antennas Design Considerations	50
3.3.2 Antennas Design Approach	52
3.4 Simulation Software	54
3.4.1 Theoretical Basis of HFSS.....	55
3.4.2 Simulation Process Overview in HFSS	56
3.5 Measurement System.....	58
3.6 Conclusion.....	59
4. Antenna Fabrication Processes	60
4.1 Introduction	60
4.2 Lithography	61
4.2.1 Photolithography.....	61
4.2.2 Electron Beam Lithography.....	64
4.3 Metallisation and Lift-off	67
4.3.1 Electron Beam Evaporation System.....	68
4.3.2 Metallisation and Lift-off Process.....	70
4.4 Gold Electroplating.....	71
4.4.1 Electroplating System	71
4.4.2 Electroplating Process	72
4.5 Sample Preparation.....	73
4.6 Fabrication Process of 3-D Printed Antennas	73

4.6.1 Fabrication Process for Two Level Elevated Antennas.....	74
4.6.2 Fabrication Process for three Level Elevated Antennas	77
4.7 Conclusions.....	79
5. Micromachined Elevated Antenna Designs	80
5.1 Introduction	80
5.2 Feeding Mechanisms of Elevated Printed Antennas.....	81
5.2.1 Coplanar Waveguide CPW	81
5.2.2 Elevated Transmission Lines	83
5.3 Elevated Rectangular Patch Antenna	86
5.3.1 Antenna Design.....	86
The configuration of antenna design	86
5.3.2 Analysis of Results	90
5.3.3 Comparison with Conventional Patch Antenna	93
5.4 CPW Fed Elevated Bow-tie Antenna	95
5.4.1 Antenna Design.....	95
5.4.2 Analysis of Result.....	97
5.5 Proximity Coupled Elevated Patch Antenna.....	99
5.5.1 Antenna Design.....	99
5.5.2 Analysis of Result.....	102
5.6 EC-CPW Fed Elevated Patch Antenna.....	104
5.6.1 Antenna Design.....	105
5.6.2 Analysis of Results	107
5.7 EMS Fed Elevated Overlapped Patch Antenna	109
5.7.1 Antenna Design.....	109
5.7.2 Analysis of Results	111
5.8 EC-CPW Fed Three Level Proximity Coupled Antenna.....	113
5.8.1 Antenna Design.....	114
5.8.2 Analysis of Results	116
5.9 Conclusion.....	119
6. Reconfigurable Micromachined Antenna.....	120
6.1 Introduction	120

6.2 Integrated MEMS Switch with Reconfigurable Antennas.....	121
6.3 MEMS Switches.....	122
6.3.1 MEMS Switches types	123
6.3.2 Advantages of the MEMS Switches Over Current Technologies.....	124
6.3.3 Limitations of the MEMS Switches.....	126
6.4 Cantilever Beam Metal-Contact MEMS Switch	127
6.4.1 Working Principle	127
6.4.2 Electromechanical Mode	128
6.4.3 Electrical Model	132
6.5 Design Challenging of Cantilever Beam MEMS Switch	133
6.5.1 Pull-Down Voltage.....	134
6.5.2 Stiction Problem	137
6.6 Proposed a New Cantilever Beam MEMS Switch Design	139
6.7 Fabrication Process of Proposed MEMS Switch.....	144
6.8 Reconfigurable MEMS Antennas	147
6.8.1 Antenna Design.....	147
6.8.2 Tuning Techniques for Frequency Reconfigurable Antennas	148
6.9 Proposed New Reconfigurable Antenna Designs	153
6.9.1 Reconfigurable Elevated Patch Antenna	153
6.9.2 Reconfigurable Proximity Coupled Elevated Patch Antenna.....	158
6.10 Conclusion	163
7. Conclusions and Future Work	164
7.1 Conclusions	164
7.2 Future Work.....	169
References.....	170
Appendix A	183
Appendix B	186

List of Figures

Figure 2 - 1 : antenna and electromagnetic waves generation.	10
Figure 2 - 2 : propagating mechanism of electromagnetic fields.	11
Figure 2 - 3 : procedures for solving antenna radiation problems.	13
Figure 2 - 4 : Typical boundaries for antenna radiation regions.	15
Figure 2 - 5 : 2-D antenna radiation pattern.	17
Figure 2 - 6 : Measuring BW from the antenna return loss.	20
Figure 2 - 7 : comparison of an isotropic antenna and practical antenna radiation pattern.	21
Figure 2 - 8 : types of antenna polarizations.	23
Figure 2 - 9 : microstrip and slot dipole antennas.	25
Figure 2 - 10 : printed patch antenna structure.	27
Figure 2 - 11 : patch antenna with microstrip line feed.	28
Figure 2 - 12 : patch antenna with coaxial probe feed.	29
Figure 2 - 13 : patch antenna with proximity-coupled feed.	29
Figure 2 - 14 : patch antenna aperture coupled feed.	30
Figure 2 - 15 : patch antenna fed with coplanar waveguide.	31
Figure 2 - 16 : techniques used to increase patch antenna bandwidth.	33
Figure 2 - 17 : surface wave in the antenna substrate.	34
Figure 2 - 18 : techniques used to synthesize a low dielectric constant by etching the substrate.	37
Figure 2 - 19 : printed antenna with EPG substrate.	37
Figure 2 - 20 : synthesize a low dielectric constant by elevating the radiators.	38
Figure 2 - 21 : different substrates used to synthesise a low effective dielectric constant.	38
Figure 3 - 1 : Electrical field at the resonant frequency of an elevated rectangular patch antenna.	42
Figure 3 - 2 : Field distribution of transmission-line model of patch antenna.	44
Figure 3 - 3: Normalized radiation pattern of patch antenna.	46

Figure 3 - 4 : Voltage, current and impedance distributed in the antenna patch.....	48
Figure 3 - 5 : Patch antenna with feed line along its radiating edge.....	48
Figure 3 - 6 : Quarter wavelength transformer placed away from the antenna.....	49
Figure 3 - 7 : Flow chart of antennas design methodology.....	53
Figure 3 - 8 : Finite element mesh for a sample of 3D printed antenna.	55
Figure 4 - 1 : a schematic diagram of the photolithography process.....	62
Figure 4 - 2 : a simplified diagram of a typical e-beam writing system.	65
Figure 4 - 3 : pattern transfer processes in a bi-layer e-beam resist system.....	67
Figure 4 - 4 : Schematic diagram of an electron-beam evaporator system.....	69
Figure 4 - 5 : metallisation and lift-off process	70
Figure 4 - 6 : a schematic diagram of electroplating system.....	72
Figure 4 - 7 : gold electroplating processes.....	73
Figure 4 - 8 : the fabrication process of two level antennas.....	76
Figure 4 - 9 : SEM photo for two level structure.	76
Figure 4 - 10 : the process flow used to fabricate three level antennas.	78
Figure 4 - 11 : SEM photo for three level structure.....	79
Figure 5 - 1: Configuration of the CPW feed mechanism with feeding post.	82
Figure 5 - 2 : Excitation of the parasitic slot-line in a coplanar waveguide.....	83
Figure 5 - 3 : Elevated feed lines configurations (EC-CPW and EMS).	84
Figure 5 - 4 : Comparison of measured losses for CPW and EC-CPW as a function of frequency.....	85
Figure 5 - 5 : Configuration of rectangular elevated patch antenna design.	87
Figure 5 - 6 : effect of the rectangular patch height on the antenna impedance. ..	88
Figure 5 - 7 : SEM photo of fabricated elevated rectangular patch antenna.	90
Figure 5 - 8 : Simulated and measured results of elevated patch antenna return loss.....	91
Figure 5 - 9 : XZ and YZ plane of patch antenna radiation pattern (gain).....	92
Figure 5 - 10 : 3-D radiation pattern of elevated rectangular patch antenna directivity.....	92
Figure 5 - 11 : Return loss of the patch antenna directly printed on the substrate.	94

Figure 5 - 12 : 3-D radiation pattern of the patch antenna directly printed on the substrate.....	94
Figure 5 - 13 : Configuration of elevated micromachined bow-tie antenna.....	96
Figure 5 - 14 : Simulated and measured return loss of elevated bow-tie antenna.....	98
Figure 5 - 15 : E and H plane of elevated bow-tie antenna radiation pattern (directivity).....	98
Figure 5 - 16 : Geometry of the proximity coupled elevated patch antenna.	101
Figure 5 - 17: SEM photo of proximity coupled elevated patch antenna.....	102
Figure 5 - 18 : Simulated and measured return loss of elevated proximity coupled patch antenna.	102
Figure 5 - 19: Radiation pattern at several frequencies across antenna bandwidth at xz-plane of elevated proximity coupled patch antenna.	103
Figure 5 - 20 : Simulated 3D gain radiation pattern of elevated proximity coupled patch antenna.	104
Figure 5 - 21 : EC-CPW fed elevated patch antenna structure.....	105
Figure 5 - 22 : SEM photo of fabricated EC-CPW fed elevated patch antenna. .	106
Figure 5 - 23 : Simulated and measured results of return loss for 5.5 μ m elevated antenna.....	107
Figure 5 - 24: 2-D radiation pattern in E and H plane at resonant frequency (gain).	108
Figure 5 - 25 : 3-D simulated radiation pattern for the antenna gain.	108
Figure 5 - 26 : <i>VSWR</i> plots of overlapped patch antenna has a narrow different between resonant frequencies.....	110
Figure 5 - 27 : Configuration of fabricated elevated overlapped patch antenna.	111
Figure 5 - 28 : Simulated and measured return losses and simulated 3-D radiation pattern.	112
Figure 5 - 29 : Radiation pattern of elevated overlapped patch antenna.	113
Figure 5 - 30 : EC-CPW fed elevated proximity patch antenna.....	115
Figure 5 - 31: SEM photo of the fabricated EC-CPW fed proximity coupled antenna.....	116
Figure 5 - 32 : Simulated and measured results of antenna return loss.....	117

Figure 5 - 33 : 3-D simulated radiation pattern at the centre frequency (Gain dB).	118
Figure 6 - 1 : MEMS switches types	123
Figure 6 - 2 : Basic operation of MEMS cantilever switch.....	128
Figure 6 - 3 : MEMS switch mechanical modelling.....	129
Figure 6 - 4 : Variation of normalized gap height (z/z_0) with applied voltage (V)...	132
Figure 6 - 5 : Equivalent circuit model for cantilever switch.....	132
Figure 6 - 6 : Cantilever beam structure of different spring constant.....	135
Figure 6 - 7: Illustration of dimensions of the meandered suspension.	136
Figure 6 - 8 : Stiction phenomenon in the cantilever MEMS switch	138
Figure 6 - 9 : Cantilever beam switches with different configuration.	140
Figure 6 - 10 : Structure of cantilever beam MEMS switch	141
Figure 6 - 11 : Dimensions of cantilever beam MEMS switch.	143
Figure 6 - 12 : I-V measurement of the fabricated cantilever MEMS switch.....	144
Figure 6 - 13 : A schematic diagram of the cantilever beam MEMS switch fabrication process.	145
Figure 6 - 14 : SEM photo of cantilever beam MEMS switch.....	146
Figure 6 - 15 : Examples of reconfigurable printed antennas by changing resonance length.	149
Figure 6 - 16 : Slotted patch antenna and its surface current path at different switch state	150
Figure 6 - 17 : Rectangular slot antenna loaded with MEMS cantilever type capacitors.....	151
Figure 6 - 18 : Reconfigurable patch antenna using shorting switches.....	151
Figure 6 - 19 : Tuning printed antennas by changing the substrate thickness.....	152
Figure 6 - 20 : Configuration of rectangular elevated patch antenna design.	154
Figure 6 - 21 : SIM photo of fabricated reconfigurable antenna.....	156
Figure 6 - 22 : Simulated results of return loss antenna at different switch states.....	157
Figure 6 - 23 : Measured results of return loss antenna at Off and On state of MEMS switch.	157

Figure 6 - 24: 3-D simulated radiation pattern (Gain dB) at Off and On state of MEMS switch.	158
Figure 6 - 25 : Geometry of the reconfigurable elevated proximity coupled patch antenna.	160
Figure 6 - 26 : Measured return loss of reconfigurable proximity coupled patch antenna at 0 and 42volt.	162
Figure 6 - 27 : 3-D simulated radiation pattern for the antenna directivity when there is no applied voltage.	162

List of Tables

Table 2 - 1 : Comparison of printed antenna types	26
Table 4 - 1 : Measured thickness of AZ4562 photoresist above the ground plane.....	75
Table 5 - 1 : Comparison of three-level and two-level antenna performances ..	117

List of Abbreviation

BELLE	Beam-writer exposure layout for lithographic engineers, a software tool.
BW	Bandwidth.
CAD	Computer aided design.
CPW	Coplanar waveguide.
FEM	Finite element method.
EBG	Electromagnetic band-gap.
EBPG	Electron Beam Pattern Generator.
EBL	Electron Beam Lithography.
EC-CPW	Elevated conductor coplanar waveguide.
EMS	Elevated Microstrip line.
GDS	Graphic data system, file format of CAD files.
HFSS	High frequency structure simulator, simulation software.
HPBW	Half power beam-width.
MMIC	Monolithic microwave integrated circuits.
IPA	Isopropyl alcohol.
MA	Mask aligner.
MEB	Electron beam evaporator.
MEMS	Micro-electromechanical Systems.
MIBK	Methyl isobutal ketone.
PML	Perfectly matched layers.
PMMA	Poly (methyl methacrylate), a positive tone electron beam resist.
RL	Return loss.
SEM	Scanning electron beam microscopy.
UHREWF	Ultra High Resolution Extremely Wide Field.
VSWR	Voltage standing wave ratio.
VRU	Variable resolution unit.
UV	Ultraviolet light
2-D	Two-dimensional.
3-D	Three-dimensional.

Author Declaration

I, Adel Saad Emhemmed, declare that the work contained within this thesis is solely mine, except where acknowledged.

1. Introduction

1.1 Motivation

Printed antennas at deep millimetre-wave (e.g G-band) have been experiencing a resurgence in popularity recently as many systems have been allocated, or are proposing to use, frequencies within this operating band. These higher frequencies and their propagation characteristics make them an excellent choice to satisfy actual requirements imposed by modern wireless communication systems, such as small profile, high data rates, low cost, short radio links and high sensing and imaging resolution [1-3]. Printed antennas are well known for their highly desirable physical characteristics such as planar configuration and light weight - making them ideal for applications that require low profile structures and convenient elements in the design of large antenna arrays. These antennas can also be integrated directly with MMICs in a single package owing to their small physical size and compatible fabrication procedure. Integration of the antenna is desirable since it often leads to miniaturization, lower costs, reduced power consumption, reduced parasitics, shrunken transceiver size and increased design flexibility compared with systems based on discrete antennas [4, 5].

Two significant trends are appearing in the new generation of modern wireless communication systems. One is to integrate antennas directly with RF, analogue and digital subsystems in a single package at millimetre-wave frequencies above $140GHz$ [2]. The other is to integrate multi-tasks in one system using a single reconfigurable antenna to eliminate the need for multiple antennas operating in various frequency

bands [6-8]. These trends are very challenging for printed antenna design due to various substrate property requirements as well as the difficulty of producing a single antenna design for different operation bands. These two considerations are summarised below.

1) substrate property requirements

Printed antennas at millimetre-waves are widely used as they are good candidates for on-wafer integration. However, they have different substrate requirements in terms of dielectric constant and thickness from the rest of the integrated circuits. Generally, printed antenna are realized thick substrates with a low dielectric constant to achieve a wider bandwidth, undisturbed radiation patterns and reduce any undesired coupling between the various elements in array configurations via the substrate [9]. This requirement can either lead to a hybrid integration solution or both antennas and other RF parts to be built on the same substrate with an intermediate dielectric constant, which therefore yields suboptimal component performance instead of the best performance for each part.

To integrate printed antenna directly with MMICs, the antenna has to be realized on a high dielectric substrate (i.e GaAs substrate $\epsilon_r=12.9$). The integration on the same substrate becomes an issue at deep millimetre-wave frequencies as the signal wavelength will become comparable to substrate thickness. This results in a strong moding effect and high loss due to surface wave excitation which in turn leads to lower efficiency, reduced bandwidth, degraded radiation patterns and undesired coupling between the various elements in array configurations [10-13]. This has limited printed antenna application in broadband modules and they are difficult to apply successfully at millimetre-wave frequencies. A reduction in surface waves is very important in millimetre-wave antenna design for it not only improves the efficiency of the antenna, but also weakens the side-lobe level which is produced by surface wave diffraction around the antenna substrate.

As micromachining technology is developed, it increasingly offers an alternative scheme to simultaneously satisfy the demands of the antenna and circuitry as it can

allow the use of the same substrate for both functions without performance degradation. Several techniques have been reported to synthesize a localized low dielectric constant environment and thus reduce the surface wave excitation. These include: (a) using two different dielectric constant substrates [5, 67]; (b) using bulk micromachining to etch a portion or complete section of the substrate material underneath and around the radiating element [14, 15]; (c) using an electromagnetic band-gap (EBG) structure [16-18]; (d) elevating the radiator element above the substrate using a membrane or using posts to lift the radiator into the air [19-23]. In addition, other techniques have been introduced in order to overcome the narrow bandwidth of the printed antennas. These techniques include using multiple-radiator resonators, modified radiator shape, stacking substrates and coupling through aperture and proximity coupled antennas [5, 24]. All of these referenced results achieved improved performance compared with conventional printed millimetre-wave antennas on relatively high dielectric constant substrates. On the other hand, a process such as etching the substrate and fabricating the membrane can be very difficult to establish when high yield is required. Also, most of these approaches are not fully compatible with MMIC processes or package processing and can consume large amounts of precious chip area.

The elevated and proximity coupled printed antenna approach can be considered as an alternative to conventional printed antenna approaches for the integration of an antenna with a MMIC and have concomitant advantages over conventional antenna designs such as broader bandwidth and reduced influence of substrate moding effects [11]. However, the feed network loss can be high for elevated antennas, since it is printed directly on the substrate and, also, proximity coupled antennas suffer from complex and cumbersome fabrication processes due to the use of two separate substrates - reasons preventing these antennas from being efficiently implemented in integrated form [25]. Therefore, the antennas which are realized in this work are based on elevated structures, using printed or elevated transmission feed lines. This will reduce the substrate effect for both the antenna and the feed line, since the antenna substrate is essentially air and most of the electric field of the elevated feed

line is confined in the air regions and not in the substrate. In addition, elevated antennas can achieve this and yet do not require separate substrates.

2) Different operation bands

A single antenna that can support multiple communication services would allow a wireless device with multiple wireless applications to utilise a single antenna element to transmit and receive signals at different frequency bands. By only requiring a single antenna element, the space required for antennas on the device is significantly reduced. To meet the need for multi-band wireless applications, a choice could be made from the following three types of antennas: (a) a single antenna showing multi-resonance characteristics for the required frequencies; (b) a very broadband antenna to cover all required frequencies; (c) a reconfigurable antenna to operate at required frequency points. Both a multi-resonance antenna and a very broadband antenna suffer interference from signals operating in unused covered bandwidths, whereas using a reconfigurable printed antenna design overcomes this problem and it can be controlled without changing the whole dimension and structure of the antenna [6].

Many techniques have been developed for the design of reconfigurable printed antennas to get multi-band operation without the use of additional radiators. These techniques tune the antenna bandwidth by controlling the antenna parameters - either by using solid state switches (diodes, transistors) or using MEMS (Micro-electromechanical Systems) switches [26, 27]. With these techniques, only the desired frequency bands or one band is in use at a time, this can decrease the level of the interfering signals and thus decrease the need for separate filtering. However, tuning the antenna operation band by using solid state switches at deep millimetre-wave frequencies limits the antenna efficiency, due to the high insertion losses [6, 28] of the switching devices. MEMS switches have been introduced as a prime candidate to replace the conventional solid state switches, since they offer high isolation, very low insertion loss, high linearity, and the MEMS actuator does not require any special epitaxial layers as in the case of diodes.

Even though MEMS switches have been shown to give very good performance, current implementations still suffer from a high actuation voltage - restricting their potential for integration with MMICs. In order to lower the actuation voltage of the MEMS switch, three different routes can be followed. These are: (a) increasing the area of actuation; (b) diminishing the gap between the cantilever and bottom electrode; (c) designing a structure with a low spring constant. In the first case, the area can only be increased by so much before compactness becomes a prevailing issue. In the second case, the isolation (parasitic parallel plate capacitance) associated with the RF signal restricts the value of the gap. The third route is the one with the most flexibility, since the design of the springs does not considerably impact the size, weight, and performance of the antenna [7, 19, 28]. A cantilever beam switch structure can be considered to provide very low values of spring constant in a compact area as well as providing high cross-axis sensitivity between vertical and lateral dimensions [29]. However, with low pull-down voltage switches, stiction (adhesion) problem in cantilever beam MEMS switch with metal-to-metal can be a serious problem [30-34]. Therefore, before the integration of MEMS switches with printed antennas, the adhesion problem associated with the contacts needs to be resolved. Therefore, in this work, we propose a simple integrated way to prevent the stiction problem without significant effect on pull-down voltage. This solution should be effective no matter what the actual cause of stiction is.

In summary, although there is much work to be found in the literature on printed antennas and frequency reconfigurable antennas at microwave frequencies, very little information can be found in the literature at G-band (*140GHz to 220GHz*). The design of printed antennas on high dielectric substrates, working at G-band and possessing high performance, full compatibility with MMICs and can be tuned for different bands using low actuation voltage MEMS switches still remains a challenging task. This research will provide characterization of such antennas - something which has not yet been done for this type of antennas.

1.3 Research Objectives

The aim of this thesis is develop MMICs compatible G-band printed micromachined antennas with fixed and reconfigurable bandwidth, and to tune for different operation bands using low pull-down voltage MEMS switches. The main objectives of this research are:

1. Study the substrate moding effect of planer transmission lines and printed antennas at millimetre-wave frequencies.
2. Develop G-band integrated micromachined antennas, this includes:
 - Develop fabrication technology.
 - Design different topology suitable for MMICs integration.
 - Examine new and more efficient techniques to feed antennas.
 - Antennas analysis.
 - Fabrication of antenna and characterisations.
3. Develop low actuation voltage MEMS technology (MMICs compatible bias voltages) with a simple integrated way to prevent the stiction problem.
4. Develop reconfigurable G-band printed antennas using the developed MEMS technology.

The technology developed in this work is a very crucial element in the future development of system integration and multifunctionality of chips. Further understanding of the parasitic effect is a crucial element in developing high performance systems.

1.4 Thesis Organization

Chapter 2 presents the basic theory of antennas and the fundamental parameters used for evaluating antenna performance, followed by a comparison of different printed antennas with a focus on the characteristics of patch antennas. This gives an understanding of the challenges to be resolved of the simulation software validation.

Chapter 3 discusses elevated patch antenna design equations, then presents several techniques used to match the antenna with its feed line. An insight into the process involved in the antenna design and layout is also provided. This is followed by an introduction to simulation software, which is used to design and predict antenna performance, and an outline of the tools which are used to measure antenna performance.

Chapter 4 developed fabrication techniques are introduced. This includes the realisation of planar antennas elevated antenna, MEMS switches, reconfigurable antennas and transmission media.

Chapter 5 introduces different and new feeding mechanisms for elevated micromachined antennas. Also, several new topologies of micromachined antennas operating at G band frequency region are discussed.

Chapter 6 covers a review of the theory of MEMS switches and their application in reconfigurable antennas. Several proposed designs of MEMS switches and reconfigurable antennas are demonstrated in this chapter.

Chapter 7 summarizes the conclusions reached and recommends future work.

2. Antenna Theory and Background of Printed Antennas

2.1 Introduction

To understand the challenges faced when designing antennas, it is necessary to provide some background information on some of the key parameters and performance metrics. There are many antenna types - each with differing geometry - but there are certain fundamental parameters which can be used to describe all of them.

This chapter presents the theory of antennas and the fundamental parameters used for evaluating antenna performance. The first part outlines what an antenna is and how it radiates. An insight is also given into the fundamentals of antenna modelling equations and their solution derivation from Maxwell's equations. The solution can be extrapolated to determine the radiation pattern of a given antenna, and determine the far and near field of radiation regions. To help evaluate antenna performance, the fundamental antenna analysis parameters, such as return loss, impedance bandwidth, directivity, antenna efficiency, gain and polarisation are discussed. The second part present a comparison of printed antennas types with a focus on the characteristics of patch antennas. An introduction to some of the feed mechanisms and bandwidth enhancement techniques of patch antenna are also presented in this chapter. This is followed by a discussion of the substrate effects on printed antennas performance at millimetre wave band, with focusing on the micromachined techniques that used to reduce these effects.

2.2 Basic Antenna Concept

Every wireless system must employ an antenna to radiate and receive electromagnetic energy. The antenna is the transducer between the system and free space and is sometimes referred to as the air interface [35]. In other words, antennas convert electromagnetic radiation into electric signal, or vice versa. A rather simpler definition of the antenna is that of a metallic device for radiating or receiving radio waves. In modern wireless systems, the antenna must also act as a directional device to optimise the transmitted or received energy in some directions while suppressing it in others. Antennas are reciprocal devices. That means the properties of an antenna are identical in both the transmitting and receiving mode. For example, if a transmitting antenna radiates to certain directions, it can also receive from those directions - the same radiation pattern applies for both cases [36]. There are numerous types of antennas developed for many different applications and they can be classified based on four distinct groups as wire, aperture, reflector, and printed antennas, and they can be used as single element or arrays [9, 37].

Regardless of the type of the antenna, they are all based on the principle that electromagnetic radiation occurs due to accelerated or decelerated electric charges within a conducting material. This can be explained with the help of Figure 2 - 1 which shows a voltage source connected to a two conductor transmission line [9]. When a sinusoidal voltage is connected to these two conductors, electric field E and magnetic field H are created. Due to the time varying electric and magnetic fields, electromagnetic waves are created and these travel between the conductors. As these waves approach open space, free space waves are formed by connecting the open ends of the electric lines. Since the sinusoidal source continuously creates the electric disturbance, electromagnetic waves are created continuously and these travel through the transmission line, through the antenna and are radiated into the free space. Inside the transmission line and the antenna, the electromagnetic waves are sustained, but as soon as they enter the free space, they form closed loops and are radiated. During propagation in space, some components of electric and magnetic field vectors decay

very quickly away from the antenna. Only orthogonal components of the electric and magnetic fields are maintained during propagation at far way distance [9].

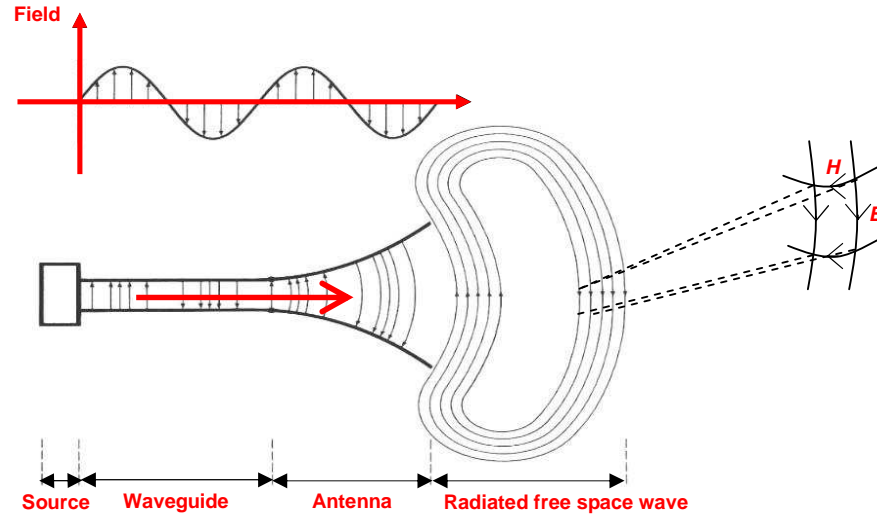


Figure 2 - 1 : Antenna and electromagnetic waves generation.

2.3 Antenna Modelling Equations

The basic equations which are used for antenna modelling are derived from Maxwell's equations. Maxwell's equations allow the calculation of the radiated fields from a known antenna current distribution. They also give a description of the behaviour of the fields around the antenna geometry. Maxwell's equations can then be used to understand the fundamental principles of antennas. The equations are presented below [38-40].

$$\nabla \times \vec{E} = -j\omega\vec{B} - \vec{M} \quad [\text{Faraday's law}] \quad (2.1)$$

$$\nabla \times \vec{H} = j\omega\vec{D} + \vec{J} \quad [\text{Ampere's law}] \quad (2.2)$$

$$\nabla \cdot \vec{D} = \rho_e \quad [\text{Gauss' laws for electric field}] \quad (2.3)$$

$$\nabla \cdot \vec{B} = \rho_m \quad [\text{Gauss' laws for magnetic field}] \quad (2.4)$$

where, \vec{E} is the electric field intensity (V/m), \vec{H} is the magnetic field intensity (A/m), \vec{D} is the electric flux density (C/m²), \vec{B} is the magnetic flux density (Wb/m²), \vec{J} is the electric current density (A/m²) and ρ_e is the electric charge density (C/m³). The quantities of magnetic current density \vec{M} and magnetic charge density ρ_m are non-physical and they are included in the symmetric forms of Maxwell's equation for mathematical convenience.

The qualitative mechanism by which Maxwell's equations give rise to propagating electromagnetic fields of time-varying sources (current and charge) is shown in the Figure 2 - 2. A time-varying current \vec{J} on a linear antenna generates a circulating and time-varying magnetic field \vec{H} , which through Faraday's law generates a circulating electric field \vec{E} , and \vec{E} through Ampere's law generates a magnetic field, and so on. The cross-linked electric and magnetic fields propagate away from the current source. Maxwell's equations are compact mathematical expressions of the electromagnetic interactions of physical nature [36, 40].

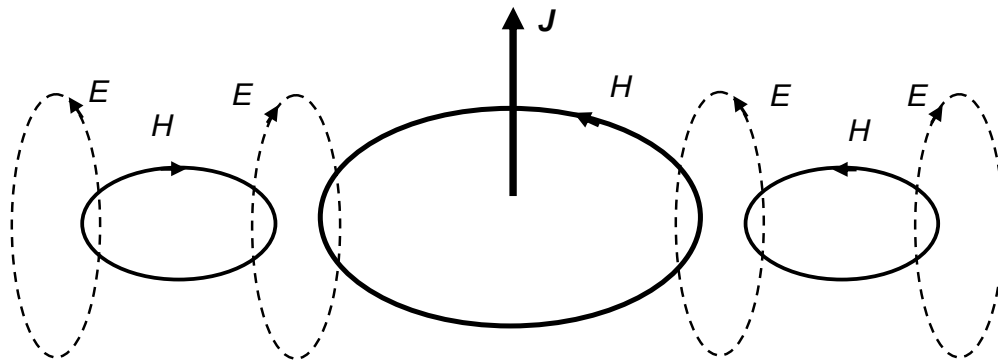


Figure 2 - 2 : Propagating mechanism of electromagnetic fields.

Calculation of the radiated field produced by an electric current source in free space can be regarded as a basic antenna problem. An antenna configuration is an electromagnetic boundary value problem. Therefore, the fields radiated must satisfy Maxwell's equations. Both electric \vec{J} and magnetic \vec{M} current densities, and also

electric ρ_e and magnetic ρ_m charge densities are allowed to represent the antenna (sources of excitation). The respective current and charge densities are related by the continuity equations [40].

$$\nabla \cdot \vec{J} = -j\omega\rho_e \quad (2.5)$$

$$\nabla \cdot \vec{M} = -j\omega\rho_m \quad (2.6)$$

Although magnetic sources are not physical, they are often introduced as electrical equivalents to facilitate solutions of physical boundary value problems. In fact, for some configurations, both electric and magnetic equivalent current densities are used to represent actual antenna systems. For a metallic wire antenna, such as a dipole, an electric current density is used to represent the antenna. However, an aperture antenna, such as a waveguide or horn, can be represented by either an electric current density or an equivalent magnetic current density.

Since Equations 2.1 and 2.2 are first-order coupled differential equations (each contains both electric and magnetic fields), it is often more desirable to couple the equations. When this is done, two non-homogeneous vector wave equations can be obtained; one for \vec{E} and one for \vec{H} [38].

$$\nabla^2 \vec{E} + \beta^2 \vec{E} = \frac{1}{\epsilon} \nabla \rho_e + \nabla \times \vec{M} + j\omega\mu \vec{J} \quad (2.7)$$

$$\nabla^2 \vec{H} + \beta^2 \vec{H} = \frac{1}{\mu} \nabla \rho_m + \nabla \times \vec{J} + j\omega\epsilon \vec{M} \quad (2.8)$$

where $\beta^2 = \omega^2 \mu \epsilon$. For a radiation problem, the first step is to represent the antenna excitation by its source, represented in Equations 2.7 and 2.8 by the current density \vec{J} or \vec{M} or both, having taken into account the boundary conditions, and solving these equation for \vec{E} and \vec{H} . This is a difficult step and it usually involves an integral

with a complicated integrand and this procedure is represented in Figure 2 - 3 as Path 1 [38].

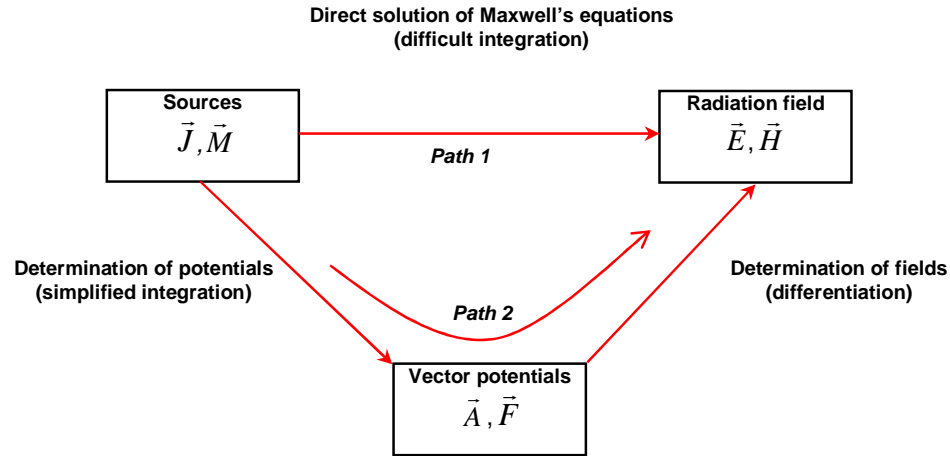


Figure 2 - 3 : Procedures for solving antenna radiation problems.

To reduce the complexity of the problem, it is a common practice to break the procedure into two steps. This is represented in Figure 2 - 3 by Path 2. The first step involves an integration while the second involves a differentiation. To accomplish this, auxiliary vector potentials are introduced. The most commonly used potentials are \vec{A} (magnetic vector potential) and \vec{F} (electric vector potential). Although the electric and magnetic field intensities (\vec{E} and \vec{H}) represent physically measurable quantities, for most engineers the vector potentials are strictly mathematical tools. In the first step of the Path 2 solution, the vector potentials \vec{A} and \vec{F} should be found, once the sources \vec{J} and \vec{M} are specified. This step involves an integration but one which is not as difficult as the integration of Path 1. The vector potentials \vec{A} and \vec{F} can be written related to \vec{J} and \vec{M} respectively as

$$\nabla^2 \vec{A} + \beta^2 \vec{A} = -\mu \vec{J} \quad (2.9)$$

$$\nabla^2 \vec{F} + \beta^2 \vec{F} = -\epsilon \vec{M} \quad (2.10)$$

If the current densities are distributed over a surface S , such as that of a perfect conductor immersed in an infinite homogeneous medium, the solutions of Equations 2.9 and 2.10 can be found as

$$\vec{A} = \frac{\mu}{4\pi} \iint_S \vec{J} \frac{e^{-j\beta R}}{R} ds' \quad (2.11)$$

$$\vec{F} = \frac{\varepsilon}{4\pi} \iint_S \vec{M} \frac{e^{-j\beta R}}{R} ds' \quad (2.12)$$

where R is the distance from any point on the antenna to the observation point. This is the most difficult step in the solution of Path 2 is the evaluation of the integrals in, for example, Equations 2.11 and 2.12. For most practical antenna geometries, these integrals cannot be evaluated in closed form. Usually approximations are made and/or numerical techniques are employed.

The next step of the Path 2 solution is to find the fields \vec{E} and \vec{H} , from the vector potentials \vec{A} and \vec{F} . This step involves differentiation by employing the concept of superposition of fields using these equations

$$\vec{E} = \vec{E}_A + \vec{E}_F = \left[-j\omega\vec{A} - j\frac{1}{\omega\mu\varepsilon}\nabla(\nabla\cdot\vec{A}) \right] + \left[-\frac{1}{\varepsilon}\nabla\times\vec{F} \right] \quad (2.13)$$

$$\vec{H} = \vec{H}_A + \vec{H}_F = \left[\frac{1}{\mu}\nabla\times\vec{A} \right] + \left[-j\omega\vec{F} - j\frac{1}{\omega\mu\varepsilon}\nabla(\nabla\cdot\vec{F}) \right] \quad (2.14)$$

Recently, with better computer simulation software, antenna modelling and evaluation is a much simpler, more convenient, and a more efficient procedure than in the past.

2.4 Antenna Radiation Field

The field patterns associated with an antenna change with distance and are associated with two types of energy. These two types are the reactive field and the radiation field. The reactive field is the portion of the antenna field characterised by standing waves and represent stored energy. The radiation field is characterised by radiating (propagating) waves and represent transmitted energy.

2.4.1 Antenna Radiation Field Regions

The space surrounding an antenna can be divided into three regions according to the properties of the radiated field. While these are not firm boundaries, they represent convention usage and provide some insight to the actual radiated field as a function of distance from the antenna. Figure 2 - 4 shows antenna radiation regions [9, 35, 41].

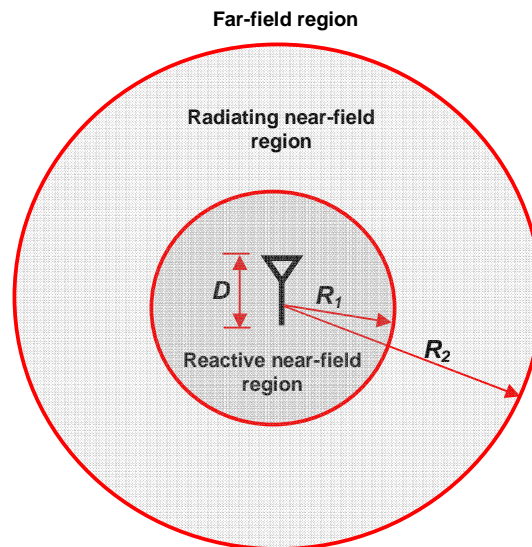


Figure 2 - 4 : Typical boundaries for antenna radiation regions.

- 1) **Reactive Near-field Region:** This region is immediately surrounding the antenna, where the reactive field (stored energy-standing waves) is dominant. In this region, energy only exists as stored energy and no energy is radiated, and E and H fields are not orthogonal. For the majority of antennas this

region exists at $R_1 < 0.62\sqrt{D^3/\lambda}$ from the antenna [9], where λ is the wavelength and D is the largest dimension of the antenna. In general, objects within this region will result in coupling with the antenna and distortion of the ultimate far-field antenna pattern [35].

- 2) ***Radiating Near-field (Fresnel) Region:*** This region lies between the reactive near-field region and the far field region, where the radiation fields are dominant and the angular field distribution is dependent on the distance from the antenna. The boundary for this region is $0.62\sqrt{D^3/\lambda} \leq R_2 \leq 2D^2/\lambda$ [9].
- 3) ***Radiating Far-field (Fraunhofer) Region:*** This region is the farthest away from the antenna, where the field distribution is essentially independent of the distance from the antenna (propagating waves), and apparent gain is a function only of the angle. The field components in this region are transverse to the radial direction from the antenna (plane wave) and all the power flow is directed outwards in a radial fashion [36, 42]. The inner boundary is taken to be at distance $R > 2D^2/\lambda$, and the outer boundary is ideally at infinity [9, 35].

2.4.2 Antenna Radiation Pattern

An antenna radiation pattern is spatial distribution of a quantity that characterizes the electromagnetic field generated by the antenna as function of position. The radiation pattern can be a mathematical function or a graphical representation (2-D or 3-D) in the far-field region of one of the antenna parameters such as gain, phase, polarization or directivity. The rectangular plots of two-dimensional patterns can be read more accurately, but the polar plots give a more pictorial representation and are thus easier to visualize. The principal plane patterns of a linearly polarized antenna are E-plane and H-plane patterns. The E-plane is the plane containing the electric field vector and the direction of maximum radiation, and the H-plane is the plane containing the magnetic field vector and the direction of maximum radiation [9, 43].

The antenna pattern parameters are shown in Figure 2 - 5. Two main parameters which can be calculated from the radiation pattern are half power beam-width (HPBW) and the front-to-back ratio. The half power beam-width can be defined as the angle between the two directions in which the radiation power is one-half the maximum value of the main lobe. The front-to-back ratio is the difference between the power level at the peak of the beam and the power level at specified rearward direction which is usually taken at worse cases or at a point 180° from the peak point [37].

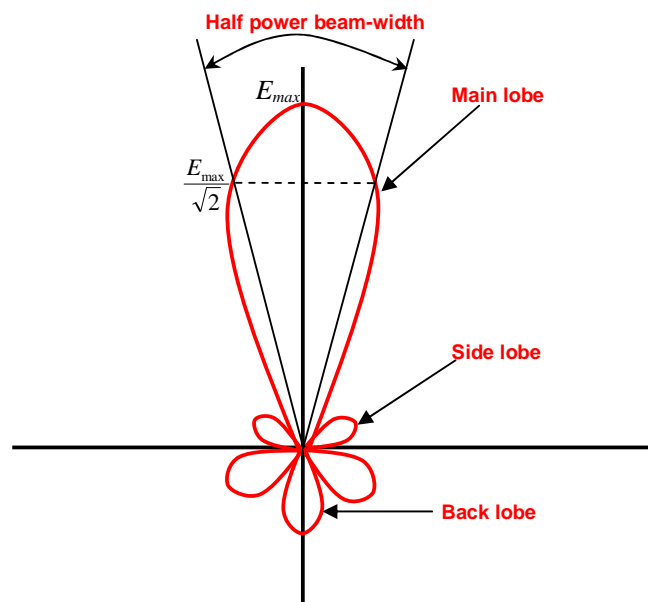


Figure 2 - 5 : 2-D antenna radiation pattern.

Radiation patterns of antennas can be classified based on the pattern shape into isotropic, omnidirectional or directional patterns [36, 41]. The isotropic antenna radiates equally in all directions and is a hypothetical (not physically realizable) concept, useful as a reference point to describe real antennas. The antenna radiates and receives equally in a given plane is called an omnidirectional antenna, and it is also called a non-directional antenna because it does not favour any particular direction in this plane. All physically realizable antennas are, to some extent, directional antennas. They focus the energy more in a particular direction than in others and can be subdivided into bidirectional, unidirectional and clover leaf types.

2.5 Antenna Parameters

To describe the performance of an antenna, definitions of various parameters are necessary. Some of the parameters are interrelated and not all of them need be specified for complete description of the antenna performance. The most fundamental antenna parameters are described below in sections 2.5.1 to 2.5.6.

2.5.1 Input Impedance and Return Loss

The antenna impedance is the impedance presented by an antenna at its terminals, is expressed as the ratio of the appropriate components of the electric to magnetic fields and is usually complex [43]. The imaginary part X_A represents the power stored in the near field of the antenna. The real part R_A consists of two components, the radiation resistance R_r and the loss resistance R_L . The power associated with the radiation resistance is the power actually radiated by the antenna or coupled to other modes, while the power dissipated in the loss resistance is lost as heat in the antenna structure due to dielectric and conductive losses [9].

When the impedance of an antenna fails to match the source impedance (transmitter/receiver), the system degrades due to reflected power. The input impedance is measured with respect to source characteristic impedance. When the two are not the same, a voltage wave is reflected, ΓV , where Γ is the voltage reflection coefficient [9, 39, 44]

$$\Gamma = \frac{Z_A - Z_0}{Z_A + Z_0} \quad (2.15)$$

Where Z_A is the antenna impedance and Z_0 is the source characteristic impedance. On a transmission line the two travelling waves, incident and reflected, produce a standing wave [44]:

$$V_{max} = (1 + |\Gamma|)V_i \quad \text{and} \quad V_{min} = (1 - |\Gamma|)V_i \quad (2.16)$$

$$VSWR = \frac{V_{\max}}{V_{\min}} = \frac{1+\Gamma}{1-\Gamma} \quad (2.17)$$

where $VSWR$ is the voltage standing wave ratio, which measure of how well the antenna is matched to source. The reflected power is given by $V_i^2 |\Gamma|^2 / Z_0$, and the incident power by V_i^2 / Z_0 . The ratio of the reflected power to the incident power is $|\Gamma|^2$, it is the returned power ratio or the return loss RL which is given by:

$$RL = 20 \log_{10} |\Gamma| \quad dB \quad (2.18)$$

For perfect matching, $\Gamma=0$, no power would be reflected back, whereas $\Gamma=1$ implies that all incident power is reflected. For practical applications, a $VSWR$ of 2 is acceptable and it corresponds to a RL of $10dB$.

2.5.2 Bandwidth (BW)

The bandwidth of an antenna is broadly defined as the range of frequencies within which the performance of the antenna, with respect to some characteristic, conforms to a specified standard. In general, bandwidth is specified as the ratio of the upper frequency to the lower frequency or as a percentage of the centre frequency. Since antenna characteristics are affected in different ways as the frequency changes, there is no unique definition of bandwidth. The two most commonly used definitions are pattern bandwidth and impedance bandwidth [9, 45].

The power entering the antenna depends on the input impedance locus of the antenna over the frequencies of interest. Therefore, the impedance bandwidth (BW) is the range of frequencies over which the input impedance conforms to a specified standard. This standard is commonly taken to be $VSWR \leq 2$ (or $\Gamma \leq 1/3$) which corresponds to a return loss of $10dB$, and translates to a reflection of about 11% of input power. Figure 2 - 6 shows how to measure BW from the RL [9]. Some applications may require a more stringent specification, such as a $VSWR$ of 1.5 or

less. Furthermore, the operating bandwidth of an antenna could be smaller than the impedance bandwidth, since other parameters (gain, efficiency, patterns, etc.) are also functions of frequencies and may deteriorate over the impedance bandwidth.

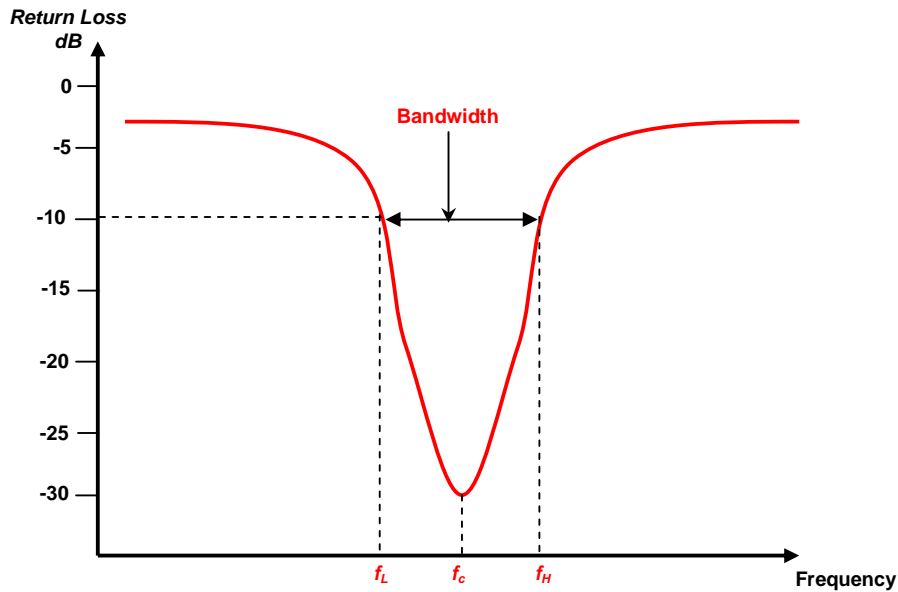


Figure 2 - 6 : Measuring BW from the antenna return loss.

2.5.3 Directivity

Directivity can be defined as the ability of an antenna to focus energy in a particular direction when transmitting or, equivalently, to receive energy better from a particular direction when receiving. It is a function of direction but it is often defined only with reference to the direction of the major lobe [9, 43, 44]. A comparison between an isotropic antenna and a practical antenna pattern fed with the same source is used to calculate the directivity - as shown in Figure 2 - 7. Directivity is a dimensionless quantity and it is generally expressed in *dB*. An antenna that has a narrow main lobe would have better directivity than one which has a broad main lobe.

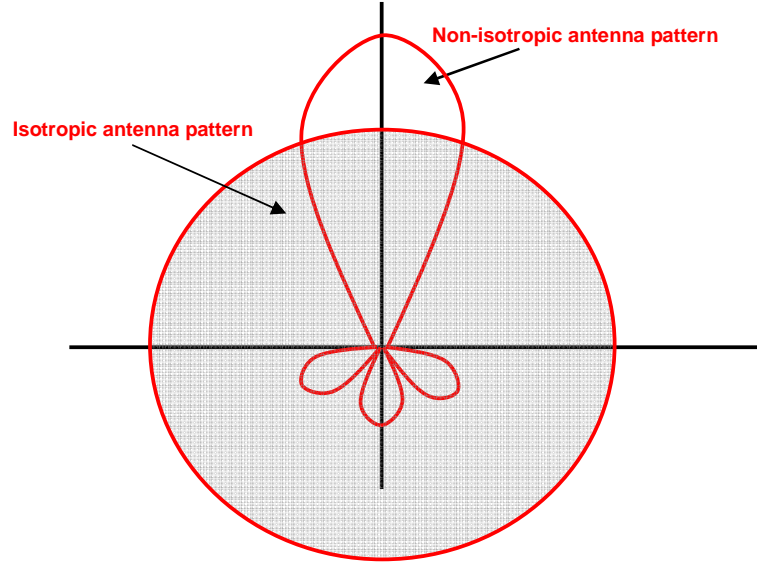


Figure 2 - 7 : Comparison of an isotropic antenna and practical antenna radiation pattern.

2.5.4 Antenna Efficiency

The antenna efficiency is a parameter which takes into account the amount of losses at the terminals of the antenna and within the structure of the antenna. It is expressed as the ratio of the total power radiated by an antenna to the net power accepted by an antenna from the connected transmitter [9, 43]. Usually, the total power delivered to the antenna terminals P_{in} is less than that available from the transmitter given the effects of mismatch at the antenna terminals. The total power delivered to the antenna terminals must be equal to the antenna ohmic losses P_{omic} (conduction loss + dielectric loss) plus total power radiated by the antenna P_{rad} . Antenna radiation efficiency, η_{cd} , is a measure of how efficient the antenna is at radiating the power delivered to its terminals and can be defined as

$$\eta_{cd} = \frac{P_{rad}}{P_{in}} = \frac{P_{rad}}{P_{omic} + P_{rad}} \quad (2.19)$$

Note that the antenna radiation efficiency does not include the mismatch (reflection) losses at the antenna connection, because it is not inherent to the

antenna alone. Total antenna efficiency, η_o , which includes the losses due to mismatch (reflection efficiency η_r) can be defined as

$$\eta_o = \eta_{cd}\eta_r \quad (2.20)$$

The reflection efficiency represents the ratio of power delivered to the antenna terminals to the total power incident on the antenna connection, and it can be easily found from transmission line theory in terms of the reflection coefficient Γ [9, 44].

$$\eta_r = 1 - |\Gamma|^2 \quad (2.21)$$

2.5.5 Antenna Gain

Antenna gain G , in simplest form, is the product of efficiency and directivity. The main difference between the definitions of directivity and gain is that the directivity is based on the radiated power while the gain is based on the input power. Not all of the input power is radiated (because of losses). Therefore, the gain can be expressed as

$$G = \eta_o \cdot D \quad (2.22)$$

Unless specified, it implies the direction of maximum radiation (maximum gain). A high gain implies both narrow beams and a better efficiency [9, 44].

2.5.6 Polarisation

The energy radiated by any antenna is contained in a transverse electromagnetic wave that is comprised of an electric and a magnetic field. These fields are always orthogonal to one another and orthogonal to the direction of propagation plane. Antenna polarization indicates the polarization of the radiated wave of the antenna in the far field region. The polarization of a radiated wave is the property

of an electromagnetic wave describing the time varying direction and relative magnitude of the electric field vector at a fixed location in space, and the sense in which it is traced, as observed along the direction of propagation. Typically, this is measured in the direction of maximum radiation [9, 43].

In general, the polarization of an antenna is classified as linear, circular or elliptical. Although linear and circular polarizations are special cases of elliptical, in practice they are usually treated separately. Circular and elliptical polarizations also are classified according to the rotation of the transmitted field vectors; this rotation can be either clockwise (right-hand) or counter clockwise (left-hand) as viewed in the direction of propagation [9, 37]. The antenna polarizations are illustrated in Figure 2 - 8.

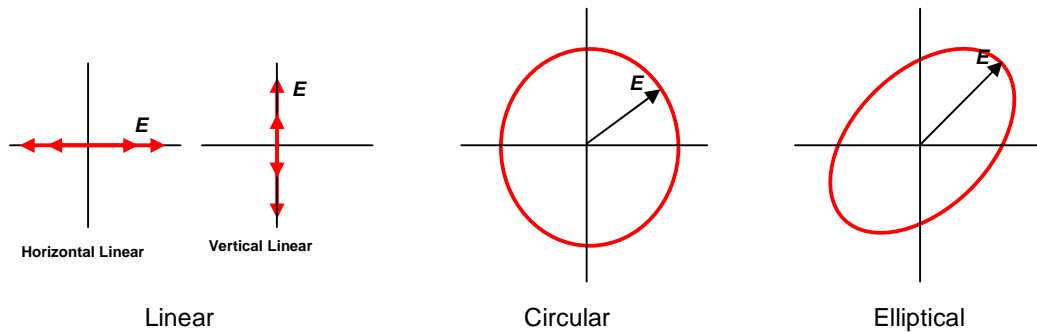


Figure 2 - 8 : Types of antenna polarizations.

The polarization of an antenna is important for several reasons. A horizontally polarized receiving antenna cannot receive vertically polarized radiation from a vertical transmitting antenna, and vice versa. Similarly, right-hand and left-hand circular antenna systems are not compatible. Sometimes this quality is used to good advantage. For example, the capacity of a microwave link can be doubled by transmitting two different information channels between two points on the same frequency using oppositely polarized antenna systems [46].

2.6 Printed Millimetre-Wave Antennas

The idea of a planar antenna as a rival to the conventional antenna was introduced in the 1950's and the first practical antenna in the form of a rectangular patch was developed in the early 1970's by Howell and Munson [24, 47, 48]. Since then, these antennas have been explored thoroughly and their highly desirable properties have been harnessed.

Printed antenna elements are radiators realised using planar transmission lines printed on dielectric substrates, and their performance is determined both by antenna geometry and by the thickness and permittivity of the dielectric substrate. In designing printed antennas, any number of substrates can be used but thick substrates with a dielectric constant in the lower range is the most desirable for good antenna performance because they provide better efficiency, larger bandwidth and loosely bound fields for better radiation into space [24]. However, the choice of the substrate is very much limited by the RF circuit coupled to the antenna, which is ideally built on the same board. In order to design a compact printed antenna, higher dielectric constants must be used which, for antennas, are less efficient and result in narrower bandwidths. Hence a compromise must be reached between antenna dimensions and antenna performance [9].

Printed antennas are a suitable choice of antenna technology at millimetre-wave frequencies due to their highly desirable physical characteristics such as low profile, light weight, low-cost mass production, capability of being fed using many different methods, ruggedness and are well suited to integration with integrated circuits and MMICs [49, 50]. There are several different configurations of printed antenna but the most common at millimetre wave region are the patch, dipole and slot antennas.

A dipole antenna is usually a half-wavelength or wavelength long metal wire or strip printed on a substrate [2]. The shape of the printed dipole is a narrow rectangular strip with width less than 0.05λ and total length is slightly smaller than $\lambda/2$, where λ is the wavelength in the dielectric medium at resonant

frequency as shown in Figure 2 - 9 - a. The feeding of a dipole can be done using, for example, microstrip line or CPW. There are various types of printed dipoles, which include centre-fed coplanar strips dipole, double sided printed dipole, folded printed dipole, bow-tie dipole and Yagi-Uda printed dipole antenna [51, 52].

The slot antennas have the simplest structure of a single metallic layer with a gap or aperture whose width is much smaller than the length. A slot dipole antenna is usually a half-wavelength at the desired resonance frequency. Slot antennas can be fed either by electromagnetic coupling with a microstrip line or with a coplanar waveguide (CPW) transmission line, but CPW is the most common since it enables direct connection to the integrated circuit and no via holes between different substrate layers are needed. Figure 2 - 9 - b shows a slot antenna with CPW feed. There are many configuration of slot antenna but the most common are slot dipole, loop slot, folded slot, bow-tie slot, arc-slot, T-slot and tapered slot antennas [53, 54].

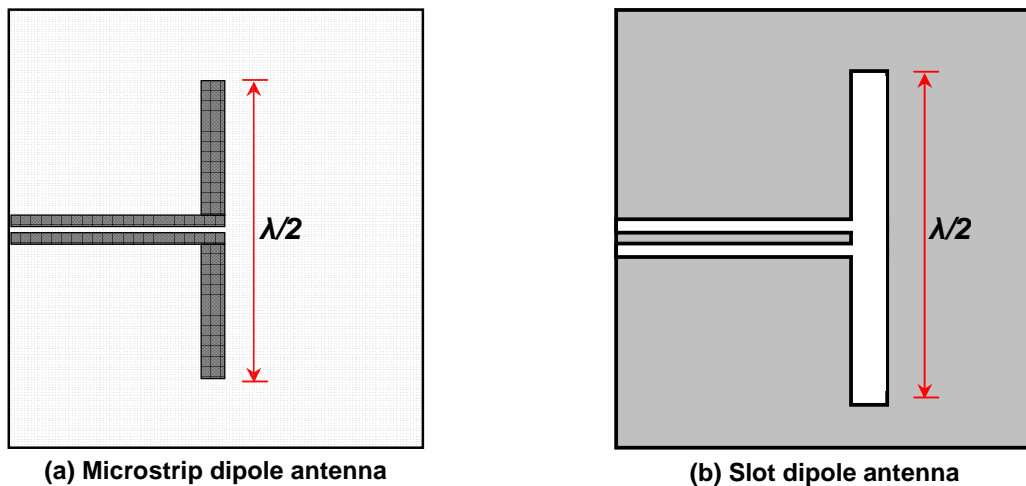


Figure 2 - 9 : Microstrip and slot dipole antennas.

Microstrip dipole and slot antennas have limitations in the design of high performance antennas such as limited antenna configurations, surface wave losses, bi-directional radiation, limited bandwidths, and feeding transmission line loss. The flexibility of the patch antenna configurations is the main reason why these structures

were chosen in this project. The next section provides more details on patch antennas [55]. Table 2 - 1 shows a comparison of printed antenna types.

Table 2 - 1: Comparison of printed antenna types

Characteristics	Patch antennas	Slot antennas	Dipole antennas
Profile	Thin	Thin	Thin
Fabrication	Very easy	Easy	Easy
Polarization	Linear / Circular	Linear / Circular	Linear
Dual frequency	Possible	Possible	Possible
Shape flexibility	Any shape	rectangular / circular	Rectangular/triangular
Spurious radiation	Exists	Exists	Exists

2.7 Printed Patch Antenna

Patch antennas consist of a very thin ($t \ll \lambda_0$, where λ_0 is the free space wavelength) metallic strip (patch) placed a small fraction of a wavelength ($h \ll \lambda_0$, usually $0.003\lambda_0 \leq h \leq 0.05\lambda_0$) above a ground plane. The patch and the ground plane are separated by a dielectric sheet (referred to as the substrate) [9]. Figure 2 - 10 shows a diagram of a printed patch antenna. The patch can take any arbitrary shape, but it is usually taken as a regular shape (square, rectangular, circular, triangular, elliptical, trapezoidal, H-shaped) for ease of analysis and understanding of the antenna characteristics. The shape and dimensions of the radiating patch usually determine the frequency of operation and thus these antennas are classified as resonant antennas. For example, a rectangular patch at TM_{10} mode has its length slightly smaller than $\lambda/2$ [24, 49].

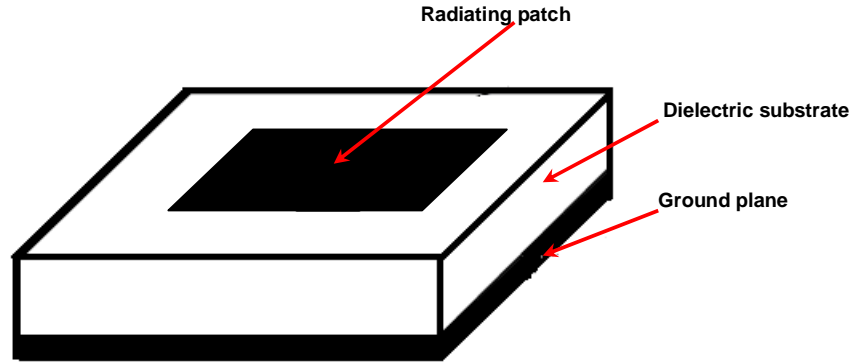


Figure 2 - 10 : Printed patch antenna structure.

Radiation from the patch antenna can occur from the fringing fields between the periphery of the patch and the ground plane. The source of fringing field is large amount of charge and repulsive forces which push the charges to the edge of the patch, creating a large density of charge at the edges. The length of the rectangular patch for the fundamental TM_{10} mode excitation is approximately a one-half wavelength when the air is the antenna substrate. However, if the antenna loaded on a dielectric substrate, the resonant length of the rectangular patch decreases as the dielectric constant of the substrate increases [49].

2.7.1 Patch Antenna Excitation

Excitation methods influence the input impedance and the polarization characteristics, but the feed line should be placed in the middle of the width of the patch to avoid the excitation of the orthogonal TM_{01} mode. Several feeding mechanisms can be used for the patch antenna and they offer the designer many parameters with which to optimize the antenna performance. Microstrip line and the coaxial probe feed are classified under the group of direct contact feeding methods while the proximity coupling, coplanar waveguide (CPW) and aperture coupling are grouped under the non-contact feeding methods. In the direct contact method, the RF power is fed directly to the radiating patch using a connecting element, while in the non-contact scheme electromagnetic field coupling is used to transfer RF power between the feed line and the radiating patch. However, the CPW feed is the most

common at millimetre wave regions due to its low loss and dispersion compared with other feeding mechanisms [9, 24].

- 1) *Microstrip line feed*: In this type of feed technique, a conducting strip, which is smaller in width compared to the patch, is connected directly to the edge of the patch as shown in Figure 2 - 11. The advantages of this feeding method are that it is easy to fabricate, simple to match by controlling the inset position and relatively simple to model. The most obvious setback while attempting to improve its operating bandwidth by increasing the substrate thickness is an increase in surface waves and spurious feed radiation.

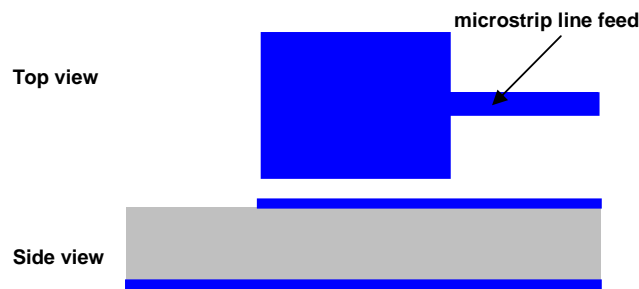


Figure 2 - 11 : Patch antenna with microstrip line feed.

- 2) *Coaxial probe feed*: The inner conductor of the coax is attached to the radiating patch while the outer conductor is connected to the ground plane as shown in Figure 2 - 12. This feed method is simple to match by controlling the position of the probe at any desired location inside the patch. However, it has significant probe radiation and matching problems for thicker substrates, since increasing probe length make the antenna input impedance more inductive.

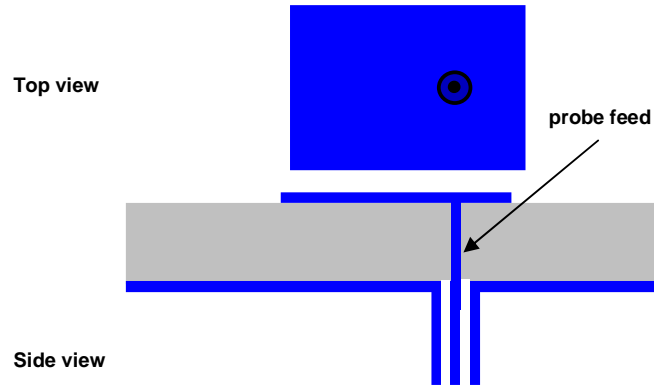


Figure 2 - 12 : Patch antenna with coaxial probe feed.

- 3) *Proximity coupled feed:* This non-contact feeding method works on the principle that the feed line need not necessarily touch the resonator because it can be excited by proximity coupling. The proximity coupled feed uses a two layer substrate with a microstrip line on the lower substrate, terminating in an open stub below the antenna element which is printed on the upper substrate as shown in Figure 2 - 13. The length of the feeding stub and the antenna element width to microstrip line width ratio can be varied to adjust the input impedance of the antenna. This method is considered difficult to fabricate because of two dielectric layers used instead of one, although it has the largest bandwidth, is easy to model and has low spurious radiation.

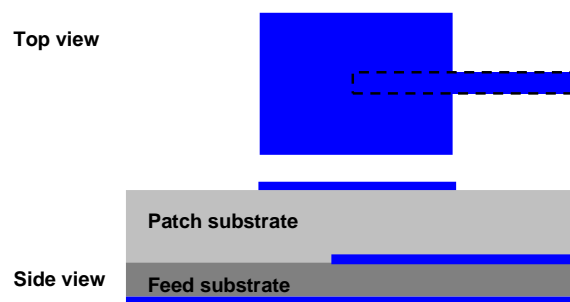


Figure 2 - 13 : Patch antenna with proximity-coupled feed

- 4) *Aperture coupling feed:* In this type of feed technique, the radiating patch and the microstrip feed line are separated by the ground plane as shown in Figure 2 - 14. Coupling between the patch and the feed line is made through a slot or an aperture in the ground plane. The coupling aperture is usually centred under the

patch, leading to lower cross polarization due to the symmetry of the configuration. The amount of coupling from the feed line to the patch is determined by the shape, size and location of the aperture. Since the ground plane separates the patch and the feed line, spurious radiation is minimized. This method is the most difficult among all feed types in fabrication because multi-layer fabrication is required and it possesses a narrow bandwidth as a limitation. However certain advantages have overridden this limitation. These advantages are that the patch and the feed layer are completely shielded from each other; spurious radiation from the feed will not degrade side lobes levels or contribute to cross polarizations. Furthermore, the use of two substrates allows the independent optimisation of the feed mechanism and the antenna.

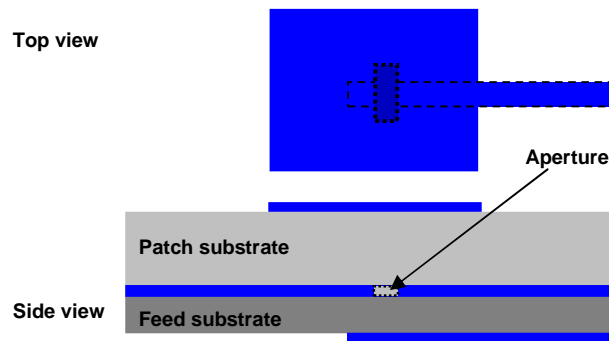


Figure 2 - 14 : Patch antenna aperture coupled feed.

- 5) *Coplanar waveguide feed (CPW)*: In this method, the coplanar waveguide is etched on the ground plane of the patch antenna and patch separated from ground plane by other dielectric substrate. The patch is excited by electromagnetic coupling using a slot formed in the ground plane and connected to the CPW feed line. The slot can be adjusted to an appropriate location below the patch to enhance the electromagnetic coupling and to obtain a suitable input impedance. Therefore, an antenna can be directly matched to the CPW feed [56] - as shown in Figure 2 - 15. The CPW offers several advantages over conventional microstrip line such as it is lower radiation loss, reduced surface wave excitation and is easier to integrate with other circuits [57]. Also, the CPW line has a uniplanar construction which implies that all of the signal lines and ground planes are on the same

surface of the substrate. This attribute simplifies manufacturing by eliminating the need for backside via holes. However, it can cause the excitation of the parasitic slot-line mode and surface waves millimetre-wave frequencies [58].

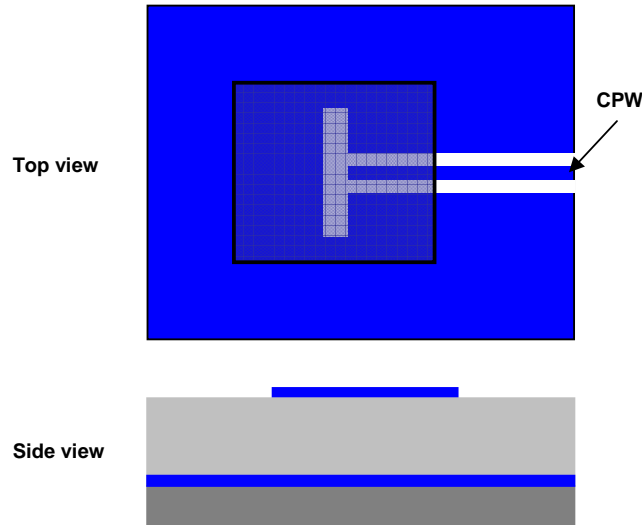


Figure 2 - 15 : Patch antenna fed with coplanar waveguide.

2.7.2 Impedance Bandwidth Enhancement Techniques

One of the major disadvantages of printed antennas is their inherent narrow bandwidth. Much work has been done to create either entirely new designs or variations to the existing antennas that give either wider bandwidths or multiple-frequency operation in a single element. However, most of these innovations bear disadvantages related to the size, weight or overall volume of the single element and the improvement in bandwidth usually comes with a degradation of the other characteristics. This section introduces the general techniques to improve the narrow bandwidth characteristic of patch antennas.

There are three ways of increasing the bandwidth. The first technique is simply increasing the thickness of the substrate. However, this technique introduces various problems. A thicker substrate will support surface waves, which will deteriorate the radiation patterns as well as reduce the radiation efficiency. Additionally, depending

upon the z-direction, higher order modes may arise - introducing further distortions in the pattern and impedance characteristics. The second technique to increase bandwidth is decreasing the relative permittivity of the substrate, which has an obvious limitation based on size. The third method is by means of a wideband matching network. However, this concept was not feasible until an impedance-matching technique was proposed. This first impedance-matching approach was analytical. The real frequency matching technique and the simplified real frequency technique are improved versions that followed. Yet, the inherent complexity of these techniques is apparent. The main techniques which have been found to increase the antenna bandwidth are presented briefly in the following [1, 24, 59-61]:

- 1) Proximity coupled feed: a proximity coupled feed requires the use of two substrates that increases overall antenna thickness and is not easy to fabricate. The proximity coupling feed shown in Figure 2 - 13.
- 2) Modification of the patch shape: the regular configurations of the patch can be modified to create multiple resonances as shown in Figure 2 - 16 - a. It is one of the most effective ways to increase antenna bandwidth without increase in antenna profile.
- 3) Slotted patch: Slots in the radiating element can be used to meander the current and create multiple resonances. Figure 2 - 16 - b shows a slotted patch.
- 4) Multiresonator configurations: Two or more patches of different lengths can be placed in proximity with each other such that they are excited with a single feed on planar or multilayer configurations as shown in Figure 2 - 16 - c and d. Although these configurations yield broad bandwidth, they have large size, which makes them unsuitable as an array element.

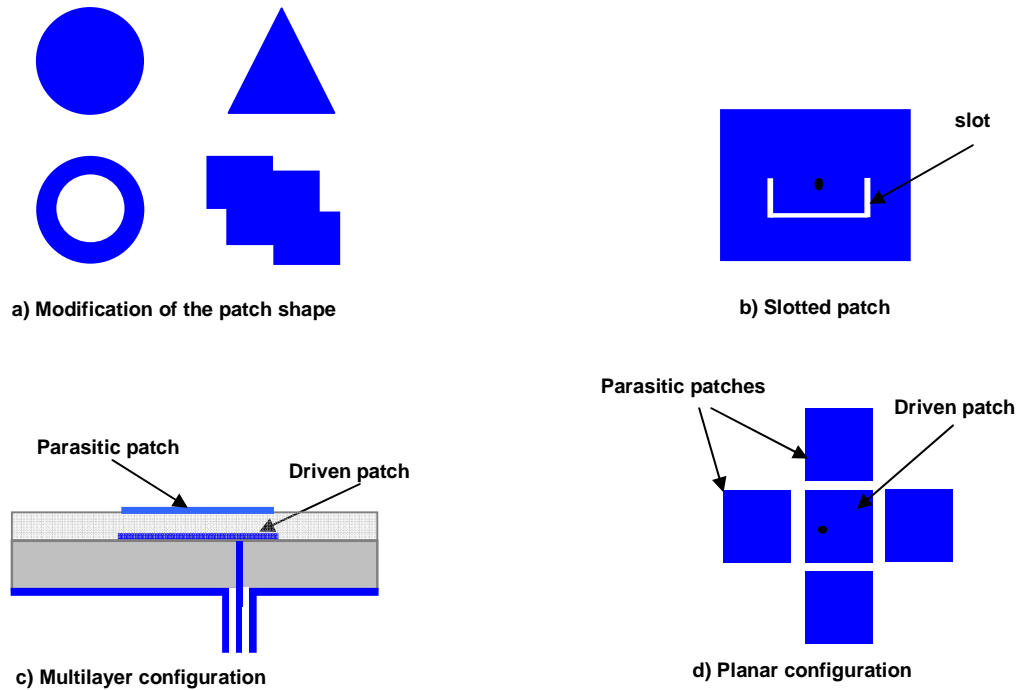


Figure 2 - 16 : Techniques used to increase patch antenna bandwidth.

2.7 Substrate Radiation of Printed Antennas

The purpose of an antenna is of course to radiate space waves. However, there are also other types of waves such as surface waves and leaky waves which can be excited in the antenna substrate depending on its thickness, dielectric constant and angles of reflection at the substrate metallic boundaries [24]. The excitation of surface wave modes is often considered to be a disadvantage in all printed antenna applications. The reason for this is that most surface waves are generally difficult to control and are not radiated in the main beam direction, but in the direction parallel to the air dielectric interface, distorting the main beam radiation pattern and increasing the level of the side lobes as well as the back lobes. Hence, the surface wave power is treated as a loss mechanism when calculating the radiation efficiency [10, 44].

The surface waves are excited from a total internal reflection mechanism with most of the field contained near or in the dielectric layer. The field becomes tightly bound

to the dielectric at higher frequencies [24]. These waves propagate slightly downwards from the radiator into the substrate, having an elevation angle θ satisfies

$$\frac{\pi}{2} \leq \theta \leq \pi - \sin^{-1}\left(\frac{1}{\sqrt{\epsilon_r}}\right) \quad (2.23)$$

Figure 2 - 17 shows this elevation angle θ in the antenna substrate. When surface waves reach the edges of the substrate, they are reflected, scattered, and diffracted causing a reduction in gain, an increase in cross-polar levels, and increase the cross coupling between array elements [10, 39, 55].

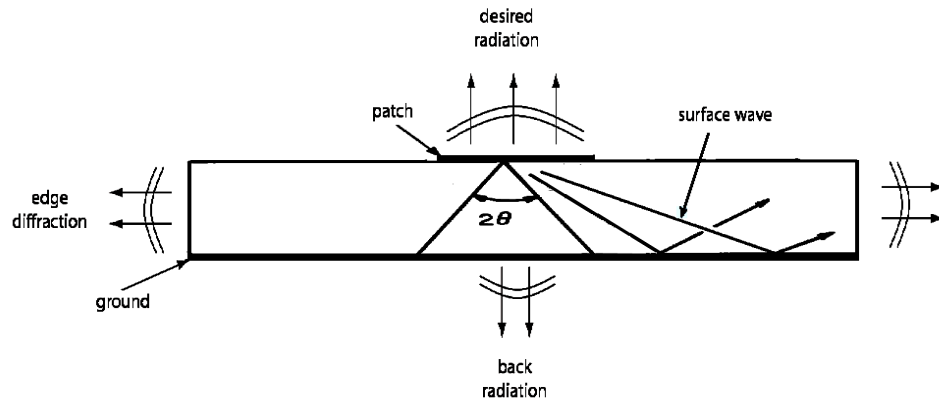


Figure 2 - 17 : Surface wave in the antenna substrate.

Surface waves in the substrate can be existed in the form of Transversal Electric TE and Transversal Magnetic TM modes. The phase velocity of these modes is a function of dielectric constant ϵ_r and substrate thickness h . If a *quasi-TEM* wave is present under the antenna radiator with a phase velocity close to the phase velocity of a surface wave mode, strong mode coupling can occur. For higher order TE and TM modes, the cut-off frequency is given by

$$f_c = \frac{nc}{4h\sqrt{\epsilon_r - 1}} \quad (2.24)$$

where c is the free space velocity of light, $n = 1, 3, 5\dots$ for TE_n modes and $n = 2, 4, 6\dots$ for TM_n modes. We can note from the Equation 2.23 that the excitation of surface wave modes increase and become a significant part of the total radiation as the substrate thickness increases or the dielectric constant increases, and also the TM_0 mode has zero cut-off frequency so that it can be generated for any substrate thickness h . Therefore electrically thick and high permittivity substrates should not be used. The loss due to surface waves can be neglected when h satisfies the following criterion

$$\frac{h}{\lambda_o} \leq \frac{0.3}{2\pi\sqrt{\epsilon_r}} \quad (2.25)$$

Surface waves can in turn lead to leaky wave radiation. Such leaky waves leak from substrate to air; leaky waves will increase the side lobes and cross polarization levels, as well as the end fire radiation. Surface wave effects are usually undesirable for antennas, so their excitation should be suppressed.

Reducing surface-wave excitation from printed antennas can be beneficial for various reasons. First, the reduction of surface-wave excitation will increase the radiation efficiency of the antenna. Second, the reduction of surface-wave excitation will result in less diffraction from the edges of the substrate or ground plane supporting the antenna - resulting in less back radiation and interference with the main pattern in the forward region. Also, reduced surface-wave excitation usually results in reduced coupling between antenna elements in an array. Generally speaking, the substrate thickness must be chosen to avoid coupling to the first higher surface wave mode. Surface wave effects are usually undesirable for antennas, so their excitation should be suppressed, and their effects must be considered in the antenna design [24, 62].

2.8 Micromachining Techniques to Reduce Substrate Effects

The substrate of printed antennas plays a very important role in achieving desirable electrical and physical characteristics. For good antenna performance, a thick substrate with low dielectric constant is desirable since this provides better efficiency. However, to integrate the antenna with other MMICs at millimetre-wave regions, a high dielectric substrate will be used, which causes high surface wave loss due to the thickness of substrates becoming electrically large [9]. This would impact negatively on the efficiency and bandwidth of the antenna. Although reducing the thickness of the dielectric reduces the amount of power launched into surface waves, it does not entirely eliminate them because the fundamental TM_0 mode has no cut-off and the radiation efficiency of antenna can therefore be greatly reduced.

As micromachining technology is developed, it offers an alternative scheme that satisfies the conflicting demands of the antenna and circuitry by using the same substrate without performance degradation of antenna or circuitry. It allows high performance antennas to be realised on high dielectric constant substrates such as silicon and GaAs. Several techniques have been reported using micromachining technology on high dielectric substrates to synthesise a localized low dielectric constant environment and thus reduce the surface wave excitation. The main techniques are presented briefly in the following:

- 1) *Etching the antenna substrate*: The first approach of etching the substrate is achieved by using bulk micromachining to etch a portion or all of the substrate material underneath and around radiating element. A low dielectric filling material inside the cavity can also be used. Figure 2 - 18 - a shows this structure. This results in two separate regions of air and the substrate material, producing a mixed substrate region with low effective dielectric constant. The walls of the hollowed cavity are in general slanted due to the anisotropic nature of the chemical etching [14]. The second approach is based on using bulk micromachining to etch or drill a series of very closely spaced holes underneath and around the antenna and to

control the effective dielectric constant with the choice of the diameter and spacing of the holes. The period of the holes must be small compared to a wavelength [63]. Figure 2 - 18 - b shows this structure.



Figure 2 - 18 : Techniques used to synthesize a low dielectric constant by etching the substrate.

- 2) *Electromagnetic bandgap (EBG)*: Another possibility is to use an electromagnetic bandgap (EBG) structure as shown in Figure 2 - 19. The PBG structure is basically a periodic metallic pattern printed on dielectric substrate and this provides a stop band to surface waves propagating through it. The frequency range of the stop band depends on the pattern geometry and its dimensions. If the antenna operating frequency falls within this stop band, it is attenuated while propagating through the substrate. Thus the generation and propagation of surface wave is stopped [16, 64].



Figure 2 - 19 : Printed antenna with EBG substrate

- 3) *Elevating the antenna radiator*: It is achieved by elevating the radiator element above the substrate using a membrane or by using posts to lift the radiator into the air as shown in Figure 2 - 20 - a and b. In the case of a membrane supported patch antenna, because the substrate under the patch is etched out, the effective dielectric constant under the patch is almost the same as the air. This will help reduce the substrate losses and improve the radiation efficiency. However, the delicate substrate etching has to be performed because the antenna performance at mm-wave frequencies is

very sensitive to the fabrication tolerances. Moreover, because the input impedance of the patch is very high, the impedance transformer (such as the $\lambda/4$ impedance transformer) is required to match the impedance. When fabricated as a patch array antenna, the feed line and the impedance transformer become very complex and, furthermore, unwanted radiation from the feed network readily occurs. Thus, the radiation efficiency of a patch antenna is degraded. Therefore, using posts to elevate the radiator can be considered as an alternative to previous techniques, with concomitant advantages of broad bandwidth and reduced dependence on substrate effects, since the antenna substrate is essentially air - the lowest possible dielectric constant [21, 65, 66].

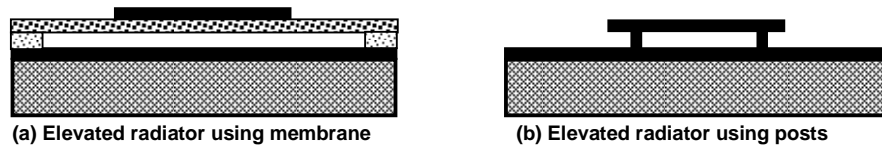


Figure 2 - 20 : Synthesize a low dielectric constant by elevating the radiators.

- 4) *Using different substrates:* In this technique, the radiator is formed on a substrate with low dielectric constant and the feed line on a substrate with high dielectric constant as shown in Figure 2 - 21. By using different substrates, the feed line network and the radiator can be optimised at the same time and the high dielectric substrate effect on the antenna can be reduced. However, use of two substrates involves exact alignment to achieve good performance. It is very difficult to align the substrates exactly and a small misalignment results in large performance degradation at millimetre-wave frequencies [5, 67].



Figure 2 - 21 : Different substrates used to synthesise a low effective dielectric constant.

2.9 Conclusion

Basic antenna concepts and radiation mechanisms along with basic equations used for modelling antenna radiation have been outlined. This provides an understanding of the challenges faced when designing antennas and helps in the investigation and selection of the proper antenna configuration and in evaluating antenna performance. A comparison has also been given of different printed antennas with a focus on the characteristics of patch antennas, which is used in this project as it is the most suitable for operation at G-band frequencies.

3. Elevated Patch Antennas Analysis and Design Process

3.1 Introduction

There is no ideal process to design and analyse printed antennas and closed form equations to calculate the parameters which give the best performance do not exist. Therefore, the dimensions of the antenna are roughly evaluated and then altered iteratively until the desired performance, or the closest possible approximation, is achieved.

This chapter presents the analysis and design processes used for elevated patch antennas. The first part of this chapter discusses the motivation for use of the elevated patch antenna and the reasons why it is considered the most attractive type of antenna i.e. its versatile characteristics. Elevated patch antenna design equations based on the transmission line model are introduced for the first time with several matching techniques that are used to match an antenna with its feed. The second part provides clear guidelines on design approaches and considerations that should be taken into account for the designs of elevated patch antennas. This chapter also presents the High Frequency Structure Simulator (HFSS) simulation software as an effective tool for modelling and predicting antenna performance with an overview of the modelling process in HFSS. The end of the chapter introduces measurement tools which are used to evaluate antenna performance at G-band frequencies.

3.2 Integration of Elevated Patch Antennas

Integrating printed antennas directly with RF circuits in a single package at G-band frequencies offers potential advantages of low cost, reduced parasitic, shrunken transceiver size and increased design flexibility compared with systems based on discrete antennas, since the shorter wavelength of G-band frequencies results in smaller antenna size and more bandwidth can be realized [14, 68, 69]. However, the signal in RF circuits is often carried through a high dielectric constant substrate. The design of conventional printed antennas on such substrates is generally avoided, as they suffer from a narrow bandwidth and excessive loss due to surface wave excitation. This has limited their applications in broadband modules and they are difficult to successfully apply at millimetre-wave frequencies [10, 13, 70, 71].

For example, GaAs substrate with $630\mu\text{m}$ thickness and dielectric constant of 12.9 is used in this work. If the antenna is printed directly on this substrate, the surface waves will propagate slightly downwards from the antenna patch into the substrate, having an elevation angle θ between $90^\circ \leq \theta \leq 163.83^\circ$ based on Equation 2.23. These waves hit the ground plane of the antenna, then are reflected, then are directed to the dielectric-to-air boundary and are again reflected, and so on (see section 2.7). Both TM and TE surface wave modes will be excited on a dielectric substrate and cut-off frequency f_c of these modes is given by Equation 2.23. The excitation of surface waves becomes significant when the substrate is electrically thick and has a large permittivity. For G-band frequencies, the first surface wave mode TM_0 has zero cut-off frequency and there are possibilities of exciting six other modes which are TE_1 , TM_2 , TE_3 , TM_4 , TE_5 , and TM_6 , since their cut-off frequencies are 34.51GHz , 69.02GHz , 103.53GHz , 138.04GHz , 172.55GHz , and 207.06GHz respectively based on Equation 2.24. To neglect the effect of surface waves, the criterion which is given by Equation 2.25 must be satisfied. For example, the thickness of GaAs substrate at 200GHz needs to be less than $8.37\mu\text{m}$; it is very difficult to satisfy this condition due to the mechanical and fabrication limitations.

It can therefore be seen that low permittivity substrates are desirable for antenna designs in many different ways since it provides better efficiency. In order to overcome the substrate effect and improve printed antenna performance, the elevated patch antenna can be considered as an alternative to a conventional printed antenna approach. Figure 3 - 1 shows the electric field at the resonant frequency of an elevated rectangular patch antenna.

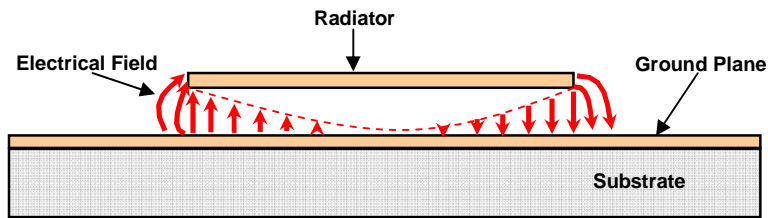


Figure 3 - 1 : Electrical field at the resonant frequency of an elevated rectangular patch antenna.

By elevating the antenna radiator above the ground plane, the antenna topology effectively will create a low dielectric substrate since the antenna substrate is essentially air (the lowest possible dielectric constant) and the electric field is confined in the air region between the patch and the ground plane, not in the high dielectric substrate. This will help increase the radiation efficiency, gain, and the radiation bandwidth [21, 65]. In addition, for traditional printed antennas integrated with other components, once the substrate specifications are chosen for the whole module, the thickness is a universal constant for each component on this substrate and it cannot be tailored freely and thus optimized for antenna design. In contrast, for the elevated printed antennas, the height of the radiator can be varied regardless of substrate used. This can be used to further enhance the patch bandwidth when we cannot change the substrate thickness for the sake of the rest of the module circuits. Thus, the elevated printed antennas can meet different application requirements and can be utilized as a substrate-independent solution. Finally, the antenna ground plane on top of the wafer will completely shield the antenna from the underlying elements and vice versa [20]. The performance exhibited by these antennas make them attractive candidates for many G-band applications.

3.2.1 Analysis Model of Elevated Patch Antenna

There is no universal mathematical synthesis method to determine the geometry of a patch antenna based on specific requirements. Usually, the design of the antennas is done through analysis of antenna geometry. Although many methods are used to analyse patch antennas, the most popular among all are those based on a transmission line model, cavity model and the full wave method [24]. Among the three methods of analysis, the transmission line model is the simplest and easiest of all but it is the most inaccurate. The cavity method is much more accurate than the transmission line method, but it is also much more complex although it gives useful physical insights. The most accurate method is the full wave model but it is also the most complex and difficult to properly apply. This model is very versatile and can treat single elements, finite and infinite arrays, stacked elements, arbitrary shaped elements and coupling [9, 24]. Recently, much commercial software has been made available for full-wave numerical analysis. In this work the transmission line model is used to calculate the initial dimensions of the antenna and then HFSS simulation software is used to carry out the full wave analysis of the designed structure.

The transmission line model is based on an equivalent magnetic current distribution around the patch edges. The antenna radiator element is viewed as a transmission line resonator with no transverse field variations (the field only varies along the length), and the radiation occurs mainly from the fringing fields at the open circuited ends. The fringing fields in this method can be modelled as two radiating slots (magnetic current elements) formed at the two ends of the patch, separated by $\lambda/2$, and each slot can be modelled as a magnetic dipole [24, 59]. The elevated patch antenna supports pure *TEM* mode of transmission since all of the electric field lines reside in the air and the phase velocities are constant.

The fundamental TM_{10} mode implies that the field varies as one $\lambda/2$ cycle along the length, and that there is no variation along the width of the patch. The vertical components of the electric field (E-field) at the two edges along the width are in opposite directions and hence cancel one another in the broadside direction, whereas the horizontal components are in same direction and hence combine in the broadside

direction. Therefore, the edges along the width are termed as radiating edges. The fields due to the sinusoidal distribution along the length cancel in the broadside direction, and hence the edges along the length are known as non-radiating edges [24, 37].

The fringing fields along the width of elevated patch can be modelled as radiating slots and electrically the patch of the antenna looks greater than its physical dimensions as shown in Figure 3 - 2.

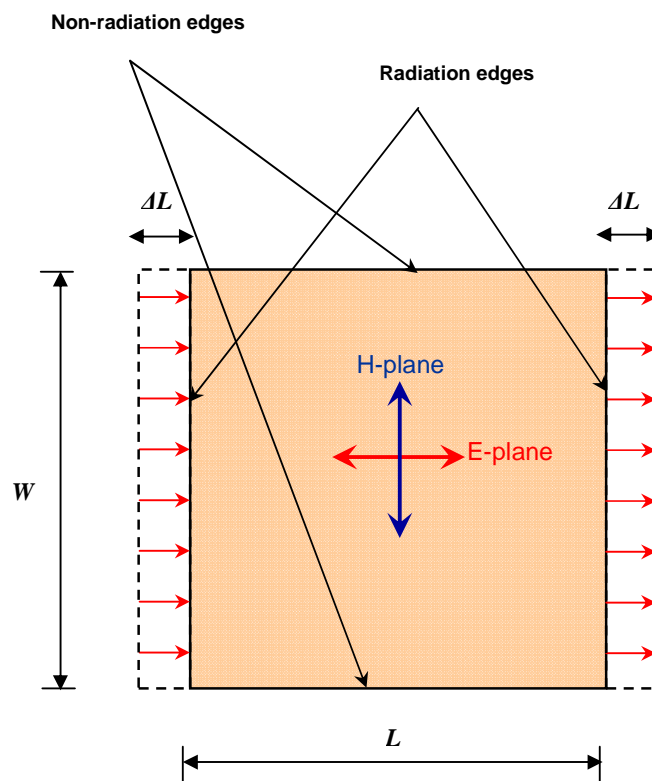


Figure 3 - 2 : Field distribution of transmission-line model of patch antenna.

The dimensions of the patch along its length have now been extended on each end by a distance ΔL . The patch is elevated above the ground plane by h_p and has width of W , Its length can be calculate using [9, 24]

$$L = L_{eff} - 2\Delta L \quad (3.1)$$

where extended on each end of the patch is

$$\Delta L = h_p \frac{(0.722W + 0.19h_p)}{(W + 0.8h_p)} \quad (3.2)$$

Also, the effective length for a given resonance frequency f_o is

$$L_{eff} = \frac{c}{2f_o} \quad (3.3)$$

Generally, the resonance frequency of rectangular patch antenna for any TM_{mn} mode can be written as

$$f_o = \frac{c}{2} \sqrt{\left(\frac{m}{L_{eff}}\right)^2 + \left(\frac{n}{W_{eff}}\right)^2} \quad (3.4)$$

where m and n are modes along length and width of the patch respectively.

The width W of the patch can be taken smaller or larger than the patch length. If W is taken larger, then the bandwidth and gain of the antenna will increase due to enhanced fringing fields from the radiation edges and antenna aperture area. However, increasing the patch width W too much leads to excited higher order modes. For example, the TM_{02} mode will be excited when W is equal to λ_o . In this case, the resonance frequency corresponding to the TM_{02} mode will be close to that of the TM_{10} mode, thereby causing interference leading to radiation pattern impurity. On the other hand, square patches may result in the generation of high cross polarization levels, and thus should be avoided unless dual or circular polarization is required. For efficient radiation and prevention of higher order modes, the patch width is taken in the range $\lambda_o/2 < W < \lambda_o$ [24, 72].

The radiation patterns of the elevated patch antenna for the fundamental TM_{01} mode can be also calculated by combining the radiation pattern of the two slots of length W and width ΔL on the infinite ground plane, which are spaced at a distance $L + \Delta L$. The normalized radiation patterns in the E-plane (E_θ in $\phi = 0^\circ$ plane) and the H-plane (E_ϕ in $\phi = 90^\circ$ plane) are given by[24].

$$E_\theta = \frac{\sin\left(\frac{k_0 \Delta L \sin \theta}{2}\right)}{\frac{k_0 \Delta L \sin \theta}{2}} \cos\left(\frac{k_0 (L + \Delta L) \sin \theta}{2}\right) \quad (3.5)$$

$$E_\phi = \frac{\sin\left(\frac{k_0 W \sin \theta}{2}\right)}{\frac{k_0 W \sin \theta}{2}} \cos \theta \quad (3.6)$$

where θ is the angle measured from the broadside of the patch and $k_0 = 2\pi/\lambda$. The fields are plotted using matlab for patch antenna with $W = L = 0.5\lambda$ in Figure 3 - 3. The antenna has a maximum field in the direction perpendicular to the patch at $\theta=0^\circ$ (broadside), and the field decreases when moving away from broadside towards lower elevations.

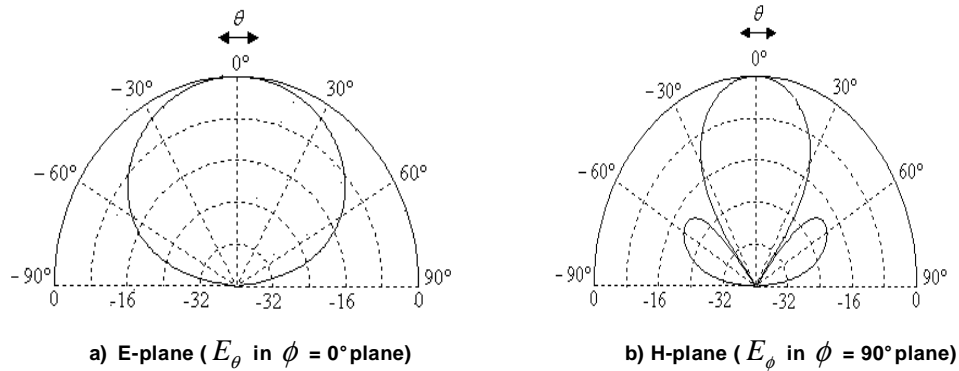


Figure 3 - 3: Normalized radiation pattern of patch antenna.

3.2.2 Matching of Antenna Input Impedance

The operation of a patch antenna over a frequency range is not completely dependent upon the frequency response of the antenna element itself but also on the frequency characteristics of the feed line - antenna element combination. In practice, the characteristic impedance of the feed line is usually real (50Ω) whereas that of the antenna element is complex. Also the variation of each as a function of frequency is not the same.

The complex input impedance of the patch antenna also varies as a function of frequency, and the resonance occurs at a frequency where the real part of input impedance (resistance) reaches its maximum at about 50Ω and complex (input reactance) is equal to the average sum of its maximum and minimum values at around 0Ω . By tuning the elevated patch antenna to the desired frequency, the feed line must be located at that point on the patch where the input impedance is equal to 50Ω and the reactive part is zero at the resonant frequency [73, 74].

Generally, the feed line of patch antenna is placed in the middle of the width of the patch to avoid the excitation of the orthogonal TM_{01} mode. For the fundamental TM_{10} mode, the impedance of the patch varies from a zero value at its centre to the maximum value at the radiating edges, since the current is maximum at the centre and minimum near the left and right edges while the voltage is zero in the centre and maximum near the left and minimum near the right edges. Figure 3 - 4 shows these quantities at resonance. The antenna input resistance at resonant frequency can be approximately calculated at a distance y by [24, 75, 76]:

$$|R_{in}| = |R_{max}| \cos^2 \left[y \frac{\pi}{L} \right] \quad \text{for } 0 \leq y \leq L/2 \quad (3.9)$$

where R_{max} is the resistance at patch border $y=0$.

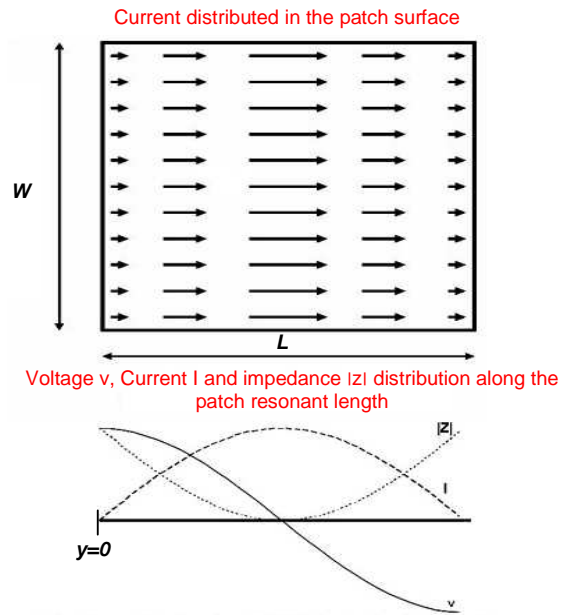


Figure 3 - 4 : Voltage, current and impedance distributed in the antenna patch.

For some feed methods, an antenna matching impedance of 50Ω can be directly obtained by controlling the feed position. However, the most patch antenna configurations have the feed line placed along the patch radiating edge. This usually leads to the characteristics impedance of the feed line not being equal to antenna input impedance. Matching an elevated patch antenna to its feed line can be accomplished using either an inset feed or quarter-wavelength transformers as shown in Figure 3 - 5 [39, 76].

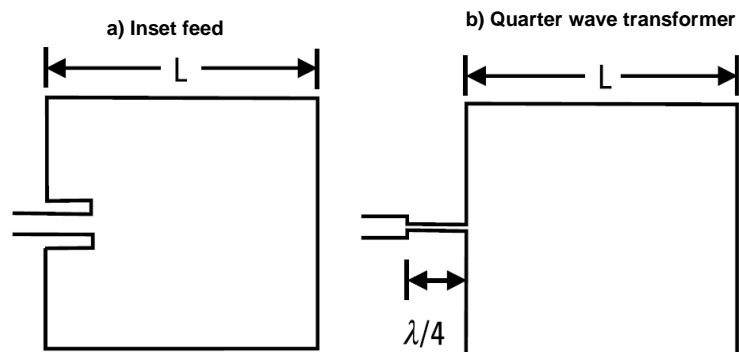


Figure 3 - 5 : Patch antenna with feed line along its radiating edge.

Inset feed technique is to artificially move the feed point to a lower impedance region inside the patch. The input impedance of the inset fed patch antenna mainly depends on the inset distance and to some extent on the inset width (spacing between feeding line and patch conductor). Variations in the inset length do not produce any change in resonant frequency, but a variation in the inset width will result in a change in resonant frequency [77].

The quarter wavelength transformer ($\lambda/4$ transformer) is a section of transmission line, one quarter of a wavelength long, that is used to transform the input resistance of the antenna to a new value that will match the characteristic impedance of a given transmission line. The quarter-wave transformer is attached directly to the antenna when the impedance of the antenna is real. However if the antenna impedance is complex, the transformer is placed a distance d away from the antenna, as shown in Figure 3 - 6. The distance d is chosen so that the input impedance toward the load at d is real and designated as R_{in} .

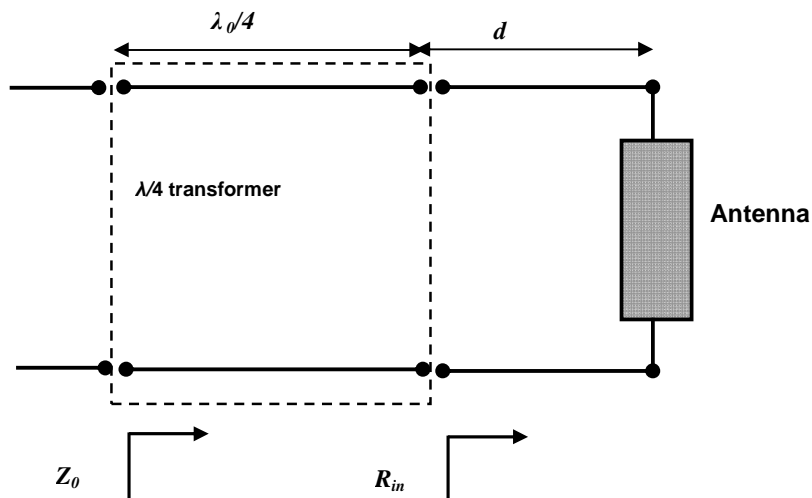


Figure 3 - 6 : Quarter wavelength transformer placed away from the antenna

To provide a match, the transformer characteristic impedance $Z_{\lambda/4}$ should be

$$Z_{\lambda/4} = \sqrt{R_{in} Z_0} \quad (3.10)$$

where Z_0 is the source characteristic impedance. The quarter wavelength transformer is usually another transmission line with the desired characteristic impedance. Because the characteristic impedances of most transmission lines are limited in range and values, and the typical values of the edge input resistance R_{max} of the patch antenna are in the range of $150 \Omega - 300\Omega$. The quarter-wavelength transformer technique is most suitable to match when microstrip transmission lines are used. In microstrips, the characteristic impedance can be changed by simply varying the width of the centre conductor [9, 37, 39].

3.3 Design Methodology

Before starting to design an antenna, specifications or requirements that the antenna has to fulfil have to be taken into account. The design of printed antennas require an understanding of the electrical and physical properties of the antennas, and also an awareness of fabrication and simulation software related issues in order to obtain proper results. Also, a designer should be able to explore the various methods available to further improve the antennas performance. Usually, the design of an improved antenna usually assumes three possibilities: a variation of an existing design, a combination of features of two or more antenna types, and an entirely new idea. The design of printed antennas in this work was based on the second and third criteria. This section provides clear guidelines on the design approach and considerations that should be taken in account for the design of the elevated printed antennas detailed in this project.

3.3.1 Antennas Design Considerations

Many factors have been studied as a part of a trade-off between the antenna performance and the physical realization considerations of the elevated printed antenna. Considerations which should be taken into account when we design elevated printed antennas are:

- 1) The resonant frequency of the antenna (frequency of operation) in the G-band (140 GHz to 220 GHz); hence the antenna configuration must be able to operate in this frequency range.
- 2) GaAs is the dielectric substrate material of the printed antenna. GaAs has been selected because of its ability to perform at high frequencies (G-band). It also allows for integration with MMICs.
- 3) CPW probe pads are required in the antenna configuration in order to obtain compatibility with measurement systems.
- 4) Gold metal has been selected to build antenna structures, because of its excellent corrosion resistance and is the most chemically stable material, since it does not form oxides offering greater longevity. Also, its relatively high electrical conductivity implies less skin depth. Further, Au is easily deposited using usual deposition methods such as sputtering, evaporation, and electroplating and has a high melting point.
- 5) The antennas should satisfy the requirements of minimum return loss of 15 dB , bandwidth more than 5 GHz , and input impedance matching at 50Ω with gain greater than 1 dB .
- 6) The height of the antenna patch radiator should be chosen to comply with the limitations of the fabrication process, where the post height is determined by thickness of the photoresist layer.
- 7) The number of the posts and their cross-section area used to elevate the radiator above the substrate should offer a mechanically strong and rigid solution.

All these points are taken into consideration for the antenna designs presented in this thesis.

3.3.2 Antennas Design Approach

Figure 3 - 7 illustrates the flow chart of design procedures. The design procedure starts with determining antenna electrical and physical specifications. The electrical specifications include the frequency of operation, the return loss, gain, bandwidth, beam width, and the polarisation. However, the physical specifications include the type of dielectric substrate and its thickness and size. Once the specification and limitations of the fabrication process are properly defined, the designer can select the antenna configuration which will meet the antenna specifications whilst taking into account the design considerations.

The proposed antenna configuration usually comprises radiator, the feed configuration and the substrate material. These parameters of the antenna configuration are the input data for the modelling method to calculate antenna dimensions. The antenna model is then translated to the computer simulation software. Outputs of the simulation software are the design parameters of the antenna and predicted results in terms of return loss, resonant frequency, input impedance, bandwidth, radiation patterns, gain and polarization. When all these parameters meet the required specifications, the antenna layout is sent for fabrication and then measured. There may be a difference between simulated and measured results. One of the error sources is the fabrication tolerance of antenna structures. Thus, to remove doubt, one must measure the actual dimensions after the fabrication process and re-simulate the structure with these new dimensions.

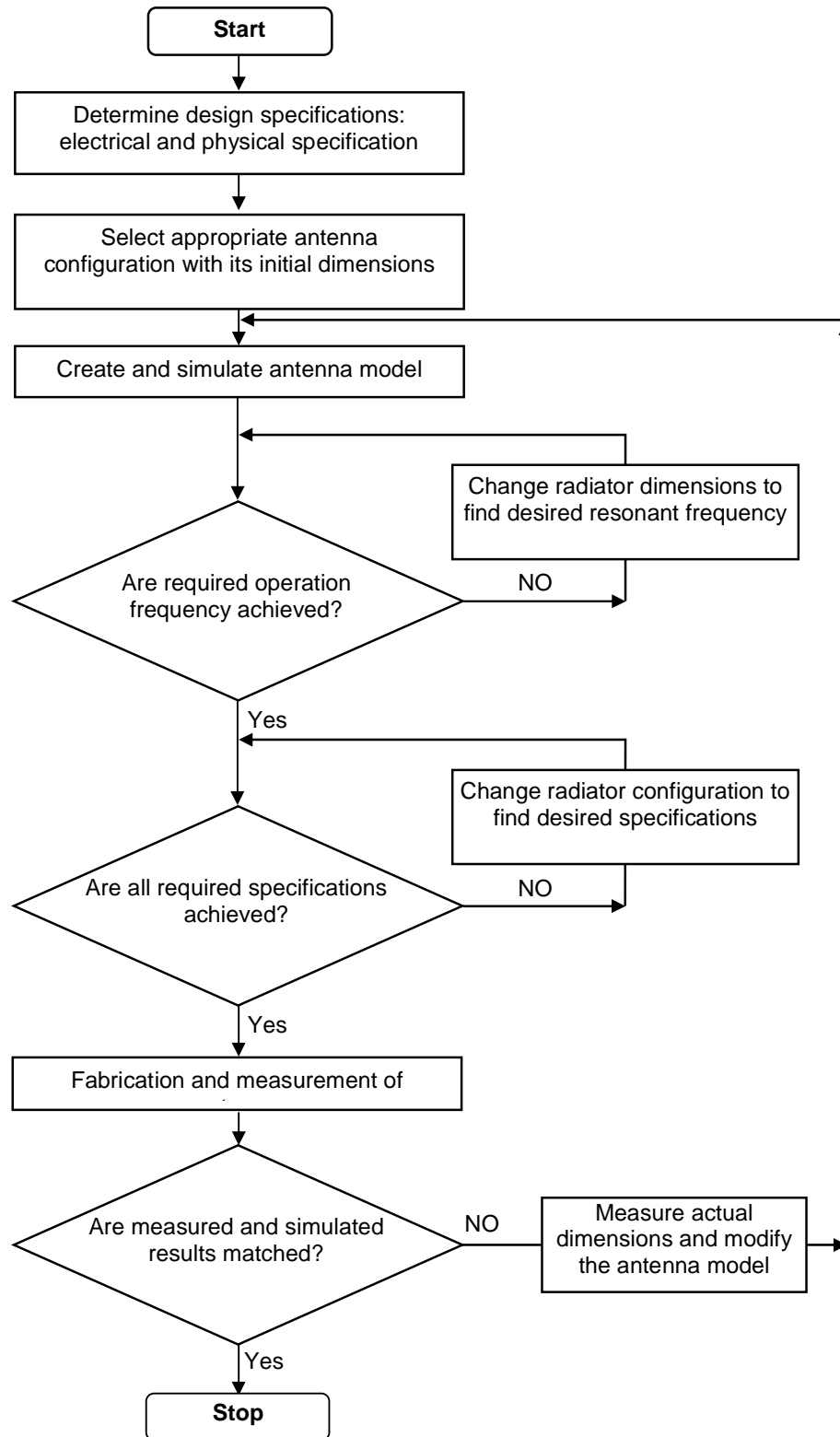


Figure 3 - 7 : Flow chart of antennas design methodology.

3.4 Simulation Software

The simulation is an important stage in modern antenna design and saves time and money before fabrication. It is an intermediate stage between design and fabrication. The simulation tool should be able to accurately characterize antenna performance and should also be able to simulate all the antenna parameters such as return loss and radiation pattern in all the planes with a high degree of accuracy. Hence, the selection of the proper simulation tool is a crucial task in the process of realizing a printed antenna.

There are many electromagnetic (EM) simulation software packages available for use in antenna design, which use different numerical techniques in the time or frequency domain, and it is often difficult to determine which program will work best for a given antenna geometry [78]. In order to streamline the antenna design process and generate accurate results before prototype construction, it is important to select an EM simulation program that will provide an optimal balance between a minimal simulation run time and a maximized correlation between the simulation results and the experimental data. High Frequency Structure Simulator (HFSS) by Ansoft is used to design and predict the performance of the printed antenna, since it provides 3-D full-wave electromagnetic field simulation. HFSS is based on Finite Element Method (FEM), it divides the geometric model into a large number of tetrahedral elements. This allows the meshing of any arbitrary 3D geometry, such as complex curves and shapes. Each tetrahedron is composed of four equilateral triangles and a collection of tetrahedra forms known as the finite element mesh. Each vertex of the tetrahedron, components of the field tangential to the three edges meeting at that vertex are stored. Figure 3 - 8 shows the finite element mesh for an elevated patch antenna. The other stored component is the vector field at the midpoint of selected edges, which is also tangential to a face and normal to the edge. Using these stored values, a vector field quantity such as the H-field or the E-field inside each tetrahedron is estimated. A first order tangential element basis function is used to perform the interpolation. Maxwell's equations are then

formulated from the field quantities and are later transformed into matrix equations that can be solved using traditional numerical techniques [79, 80].

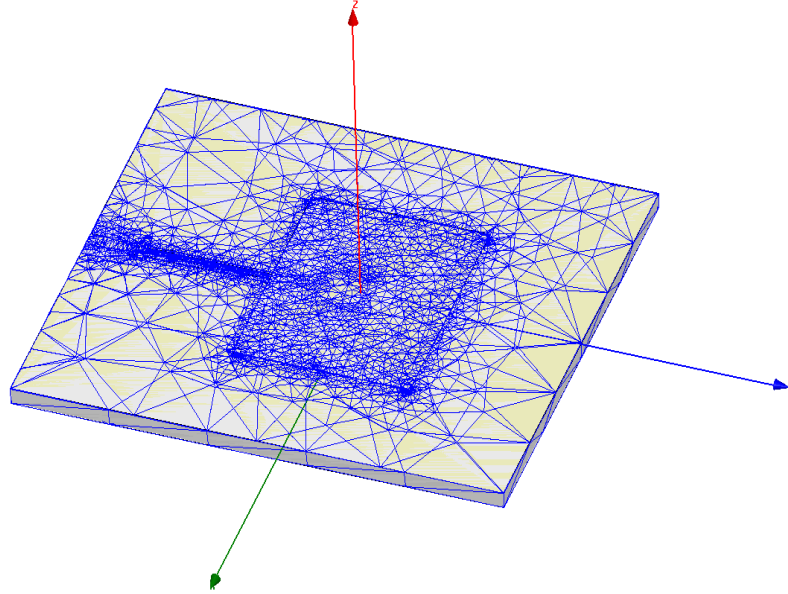


Figure 3 - 8 : Finite element mesh for a sample of 3D printed antenna.

3.4.1 Theoretical Basis of HFSS

Once a mesh is created, basis functions are defined for each tetrahedra. The basis functions, W_n , define the conditions between the nodal locations in the overall mesh of tetrahedral based on the problem inputs. The basis functions are then multiplied by the field equation, which is derived from Maxwell's equations, and can be written as.

$$\nabla \times \left(\frac{1}{\mu_r} \times \vec{E} \right) - k_0^2 \epsilon_r \vec{E} = 0 \quad (3.11)$$

The result is then integrated over the volume of the tetrahedron is

$$\int_V \left[W_n \cdot \nabla \times \left(\frac{1}{\mu_r} \times \vec{E} \right) - k_0^2 \epsilon_r \vec{E} \right] dV = 0 \quad (3.12)$$

This is then processed using the Green and divergence theorems and is then set equal to the excitation/boundary terms.

$$\int_V \left[(\nabla \times W_n) \cdot \left(\frac{1}{\mu_r} \times \vec{E} \right) - k_0^2 \epsilon_r \vec{E} \right] dV = \int_S (\text{boundary term}) dS \quad (3.13)$$

The electric-field vector is then given as a summation of unknowns, X_m , multiplied by the same basis functions used in generating the initial series of equations.

$$\vec{E} = \sum_{m=1}^N X_m W_m \quad (3.14)$$

The resulting equations allow the solution of the unknowns, X_m , to find the electric-fields. The general form of the expression is given by

$$\sum_{m=1}^N X_m \cdot \left(\int_V \left[(\nabla \times W_n) \cdot \left(\frac{1}{\mu_r} \times W_m \right) - k_0^2 \epsilon_r W_n W_m \right] dV \right) = \int_S (\text{boundary terms}) dS \quad (3.15)$$

Once the values have been calculated using the solver, a second adaptive pass occurs and HFSS compares the calculated S-parameters to the previous mesh-based solution. This process is repeated and the difference between the two solutions calculated. This process is continued until the solution has converged to an acceptable difference, usually 2% or less, this being defined by the user.

3.4.2 Simulation Process Overview in HFSS

Models in HFSS are created relatively easily, by the user or imported in a DXF, GDS etc. file format. The various aspects involved in the process of setting up and running a simulation in HFSS is provided in the following:

- 1) ***Drawing:*** The key to successful use of HFSS for solving any electromagnetic problem lies in the creation of the three-dimensional geometric model of the structure. The structure has to be visualized as a collection of two-dimensional (2D) and three dimensional (3D) objects, each of which can later be assigned a specific material or a specific boundary as the need arises. Also, it is critical to ensure that the geometry is as simple as possible, because a more complex geometry would make the finite element mesh more complex, which in turn would require higher memory and greater CPU time.

- 2) ***Assigning materials:*** HFSS creates a finite element mesh for each object based on the material that is assigned to the corresponding object. Thus, accurate assignment of materials is essential. HFSS has an extensive library of materials but it is also possible to create new materials not contained within the library. Creating your own material can be useful for investigating the effects of changing certain material parameters, such as permittivity, conductivity, dielectric loss tangent and magnetic loss tangent.

- 3) ***Assigning boundaries:*** Among the various phases involved in setting up a simulation in HFSS, assigning boundaries is the most critical. Generally, boundary conditions can be split into excitations and surface approximations. Most boundary conditions are used to define electromagnetic characteristics, but a port is the only boundary condition that allows energy to flow into and out of a structure. There are many types of excitations possible in HFSS, but the main one used for the models throughout the thesis is the wave port, since it can be placed internally or externally and support multiple modes of transmission. Radiation boundaries and perfectly matched layers (PML) are the main options to select the surface approximation for the radiation boundary.

- 4) ***Setting up the solution:*** HFSS is based on the finite element method for performing calculations. This method is implemented by creating a mesh that breaks down a structure into small cells. Choosing the mesh parameters and

selecting the frequencies at which the structure will be solved are the two most important parameters of setting up the solution. Generally, either the discrete or fast sweep with meshing smaller than $\lambda/4$ is used throughout this thesis to obtain higher simulation resolution.

A major benefit of HFSS is that it is versatile and can model all kinds of passive structures and it can calculate the full three-dimensional electromagnetic field of the antenna and the corresponding S-parameters with high accuracy [80]. Overall, the software is useful because the real operating environment of the structure can be taken into account. The simulation was carried out using Dual Intel Xeon 3.20GHz Quad Core and 64 GB DDR2 800 MHz Quad Channel FBD Memory PC platforms.

3.5 Measurement System

Testing the antenna characteristics forms one of the most important activities in the whole process. Accurate measurement of a printed antenna is a considerable challenge at high millimetre-wave frequencies. Moreover, of all the measurements that is made of any kind of RF circuit, the most difficult and least understood are those of antennas. This is because the surrounding environment plays a major role in determining the accuracy of the tests being conducted. Therefore, antennas should be tested only in a place far removed from any objects that may cause spurious reflections.

Usually, the typical tests of any antenna measurement setup are s-parameter (return loss) and radiation pattern parameters; however in this project we were not able to measure the radiation pattern because University of Glasgow do not have an on-wafer G-band anechoic chamber. In fact, these kinds of chamber do not currently exist in commercial form. We tried to build this chamber but we could not get all the components, hence we depend on matching between the simulation and measurement s-parameters to validate antenna designs and simulation predictions. On-wafer one port S-parameter measurements were

carried out in the G-band frequency range using an Agilent PNA Vector Network Analyzer with 140GHz to 220GHz Heads and Cascade Microtech ground-signal-ground high frequency coplanar probes with $100\mu\text{m}$ pitch size WR-05 waveguide probes and an impedance standard substrate to place the measurement reference plane at the probe tips and correct for any errors in the measurement system. The system is connected to a control computer running Cascade Microtech Nucleus software. This computer also runs the Cascade Microtech WinCal software which allows the configuration and management of measurements. In order to make accurate on-wafer S-parameter measurements in the region 140GHz to 220GHz , it is necessary to have on-wafer calibration standards that are well defined at all the frequencies of interest. Various strategies exist for calibration, such as the SOLT (short, open, load, thru), LRM (line, reflect, match) or LRRM (line, reflect, reflect, match), but our system was calibrated using the LRRM method with alumina ISS standards placed on an absorbing material, which is recommended by Cascade Microtech. The reference planes for the measurements were placed at the probe tips. Measurements were made with the substrate separated from the wafer chuck by a 1mm quartz spacer. This eliminates the effect of the microstrip line mode [81].

3.6 Conclusion

Printed antenna design is typically done through using transmission line model analysis to calculate the initial dimensions of the antenna and then simulation software is used to predict antenna performance, taking into account its desired specifications. As highlighted previously, design tools can greatly assist a design engineer to create antennas with the desired response. Combining this with accurate test equipment, it is possible to fully characterize and develop antennas for specific applications. The 3-D electromagnetic simulation software, HFSS, was used for every antenna designed in this thesis. This software was combined with a powerful PC to increase the design accuracy through finer meshing. A Vector Network Analyzer was used to measure the fundamental parameters used to characterize antennas.

4. Antenna Fabrication Processes

4.1 Introduction

There are several different technologies available for the designer to choose from and it is often not obvious which one is best suited for the intended application and product. A new approach for fabricating printed micromachined antennas based on developing elevated structure is introduced in this work to fulfil the fabrication process requirements.

This chapter aims to cover each of the fabrication techniques relevant to the work in this thesis. First, lithography processes and pattern transfer are summarised. Next, metallisation and lift-off processes are introduced. Gold electroplating is then described and its process is presented. Finally, fabrication development processes required for micromachined printed antennas are described in detail. Antenna fabrication involves combinations of several basic techniques, but a key enabling techniques for the successful development of the fabrication process is combining the photolithography with e-beam lithography processes to create 3-D structures.

4.2 Lithography

Lithographic processes involve the transfer of a design onto a substrate that has been covered with a thin film of radiation sensitive material, known as resist. By exposing selective regions of this resist layer to a source of radiation and then developing it in an appropriate solution, a relief image will be formed in the resist (the developer solution etches away either the exposed (positive tone) or unexposed (negative tone) areas of the thin film resist) [83, 84]. The achievable resolution of a lithographic system is therefore defined by several factors including the source and type of incident radiation and the chemistry of the resist exposure process. The radiation used must thus match the resist film sensitivity, and defines both the equipment and techniques used during exposure. Several types of lithography (such as x-ray, optical and electron-beam) have been investigated by the semiconductor industry [84, 85].

In this research two types of lithography were used. These are photolithography and electron beam lithography.

4.2.1 Photolithography

Photolithography is the process of transferring geometric shapes on a mask to the surface of a substrate. It uses light to transfer a geometric pattern from a mask to a light-sensitive chemical photoresist. The photoresist is a liquid film that can be spread out on a substrate, exposed with a desired pattern using ultraviolet UV light, and developed into a selectively placed layer for subsequent processing [86].

1. Photolithography system

Basic photolithography uses a mask held in contact with the sample to be processed using a vacuum, with UV light focused through a lens to ensure coherence and uniformity of exposure. This system, known as contact photolithography, ensures optimal pattern transfer from the mask, but as a result of the physical contact, carries a great risk of mask damage and sample

contamination. As a result, the mask is generally elevated above the substrate, which, though it removes any potential for damage or contamination, degrades the achievable resolution as a result of diffraction around mask features [86, 87]. The procedure was carried out on a MA6 mask aligner housed in the in the James Watt Nanofabrication Centre (JWNC) at the University of Glasgow.

2. Masks Fabrication

The masks required for patterning the resist were made using the e-beam tool. Technical staff were responsible for the processing of masks beyond the CAD design and e-beam job submission. The process consisted of patterning a quartz mask with chrome on one surface and e-beam resist on top of the chrome. The chrome was then etched away using a chemical wet etching and then the remaining resist removed in a barrel asher leaving the original pattern transferred into the chrome. Multiple copies of the chrome master could then be made using a photolithography technique and ferric oxide (iron oxide, Fe_2O_3) coated quartz plates (ferric oxide being opaque to UV light) [88].

3. Photolithography Resist

Two type of positive tone photoresist have been used in this work, which are S1818 and AZ4562 and they are spun at different speed depending on the required thickness. A schematic diagram of the photolithography process and details of the steps are shown in Figure 4 - 1.

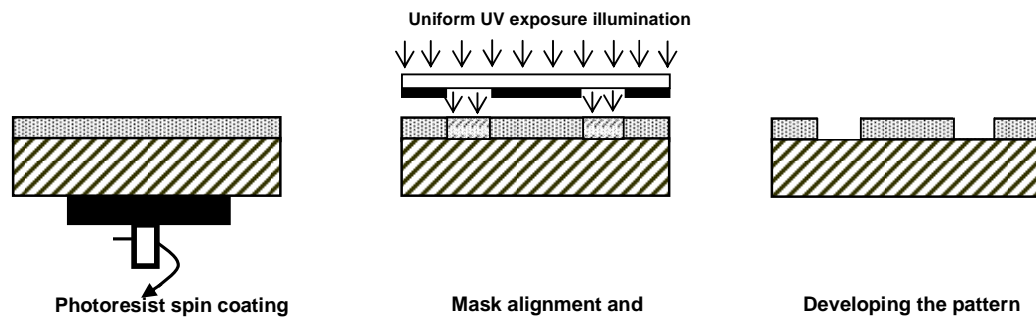


Figure 4 - 1 : A schematic diagram of the photolithography process.

- 1) ***Photoresist Spin Coating:*** The sample was held on a spinner chuck by vacuum and photoresist is poured on the sample, which is then set to high speed rotation, spreading the resist in a thin layer with a highly uniform thickness. Typically, the sample spun for 30-60 seconds at a rotational speed of 1000-6000rpm. The thickness of the resist after spin coating is inversely proportional to the speed of the spin coater and time of the spinning.
- 2) ***Baking of the Photoresist:*** The common procedure for drying out almost all of the solvent from the photoresist is to bake the sample in an oven at 90°C for 20 minutes. Baking decreases the thickness of the photoresist and makes it sensitive to ultraviolet light.
- 3) ***Mask Alignment and Exposure:*** One of the most important steps in the photolithography process is mask alignment. The mask is aligned with the substrate, so that the pattern can be transferred onto the wafer surface. Once the mask is accurately aligned with the pattern on the substrate surface, the photoresist is exposed through the pattern on the mask with a high intensity ultraviolet light. Usually, the exposing time depends on the type and thickness of the photoresist. Exposing the sample to ultraviolet light will create both exposed and unexposed portions of photoresist. The areas that are exposed to the ultraviolet light will undergo a chemical reaction.
- 4) ***Development:*** Photoresist development entails washing away the exposed resist so that the pattern will be fully developed, and it is immediately followed by the removal of the solution by spray wash. Exposed areas of S1818 photoresist were then developed in a mixture of Microposit and H₂O and a mixture of AZ400K and H₂O was used to develop the exposed area of AZ4562 photoresist.

4.2.2 Electron Beam Lithography

Electron Beam Lithography (EBL) refers to a lithographic process that uses a focused beam of electrons to form the patterns needed. Unlike photolithography, no mask is required; instead the pattern data is held only in software on computer which is used to control a finely focused beam of electrons and writes the desired pattern on a substrate coated with resist [88, 89].

1. Electron Beam Writing System

The principal components of a typical EBL machine are outlined in Figure 4 - 2. The electron gun generates the beam of electrons that is used to write the pattern on the substrate. The electrons are usually emitted by heating a tungsten filament to provide sufficient energy for electrons to overcome their work function barrier. In addition, the electron gun will normally incorporate two or more electrodes to control the emission properties of the electron source. The diameter, profile and direction of the electron beam are precisely controlled by electron optics within the column, whilst accurate sample alignment is achieved by fine control of the stage positioning mechanism within the chamber. During operation, the vacuum system maintains a constant pressure throughout the column and at the gun assembly and also controls the pressure changes required for loading and unloading samples. The supporting electronic systems supply power and transmit the signals that regulate various components throughout the e-beam machine and the entire system is managed by a master computer [87, 88].

In this work, a Leica Electron Beam Pattern Generator 5 (EBPG5) was used to fabricate the masks. Also a newer Leica VB6 Ultra High Resolution Extremely Wide Field (UHR EWF) was employed for all other steps.

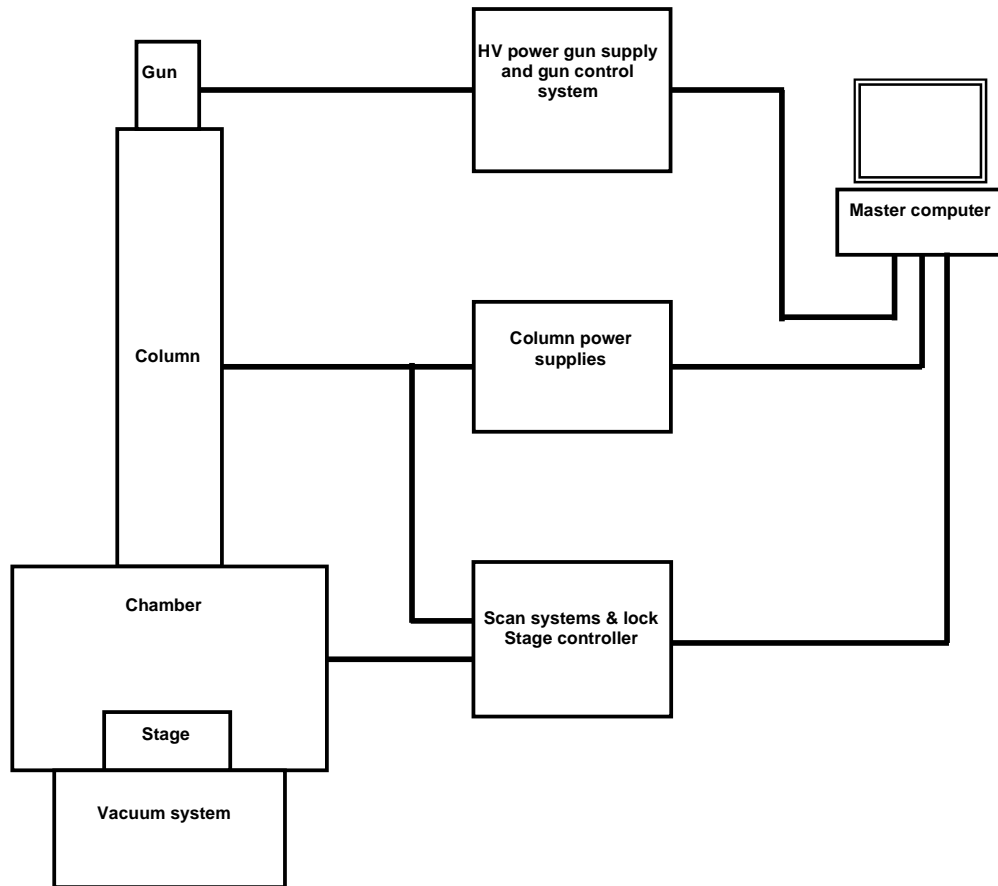


Figure 4 - 2 : A simplified diagram of a typical e-beam writing system.

2. Pattern Definition

The e-beam lithography tool can write large patterns from conjoined small fields. However, the large area structures must be split into shapes realisable by the pattern generator. To achieve this, the fracturing process breaks large shapes into trapezoidal subshapes which can be realised within a subfield and potentially into larger fields for stitching. After creating a pattern file in the CAD software proprietary format, it is usually exported in the universal GDSII (Graphical Design System II) format. Commercial fracturing tools such as the CATS package are used to fracture the pattern into fractured files, as the format required by the e-beam tool. The layout of these fractured files can then be specified using a command file which instructs the control computer to expose the fractured patterns with a given sample size, dose, beam size and resolution. These files are

created using the BELLE (Beam-writer Exposure Layout for Lithographic Engineers) software tool developed at the University of Glasgow [90]. Further layers can be aligned relative to the first metallization layer to produce multi-level devices. This is generally done by scanning for the edges of a marker of a specified size relative to an easily found large feature at a known substrate location. The Belle file contains information about the relative position of the new pattern to the original metal layer allowing accurate registration [88, 91].

3. Electron Beam Lithography Resist

Electron beam resists are normally coated on the sample to record the image of the pattern to be transferred. It is usually high molecular-weight polymers with long chains. The long polymer chains are broken by the electron beam, this reduces the average molecular weight and hence the chains become soluble in a developer which selectively removes shorter chain length molecules. A solvent developer selectively washes away the weakened or lower molecular-weight resist, thus a pattern is formed in the resist layer. The development time and temperature strongly influence pattern transfer, and have an interaction with the exposure dose. In general, raising the developer temperature increases resist solubility, resulting in faster pattern development. There is a time delay associated with the chemical processes of development and development is not immediately complete on introduction into the solution. As a result, developing for too short a time will leave a portion of the exposed resist on the substrate, whilst developing for too long will further erode the resist exposed by backscattering, resulting in enlargement of the pattern. There is therefore an optimal development time for a given exposure dose [92].

For this project, the e-beam resist of choice was poly-methyl methacrylate (PMMA) which has excellent resolution and is easy to process. PMMA is available in a variety of molecular weights and has a wide processing range [89, 93]. A bi-layer e-beam resist system was used to produce an undercut profile to enhance the lift-off process. To facilitate consistent and effective metal lift-off with PMMA, two layers are spun and baked consecutively. The lower layer is a

higher concentration and lower molecular weight resist solution. This makes it thicker and more sensitive to e-beam dose. The upper layer is thinner and less sensitive. The result is that for a given dose the lateral dimensions of the exposed region of the lower layer will be larger than those of the upper region and the lower region will be thicker than the upper. This gives the familiar lip and undercut of the resist lift-off profile. The resist profile is dependent on a combination of concentration and spin speed (i.e. resist thickness), molecular weight (sensitivity to dose), e-beam dose, developer dilution and development time. PMMA resists are generally developed in methyl isobutyl ketone (MIBK), diluted in isopropyl alcohol (IPA) [84, 93, 94]. Figure 4 - 3 shows the pattern transfer process in a bi-layer resist system.

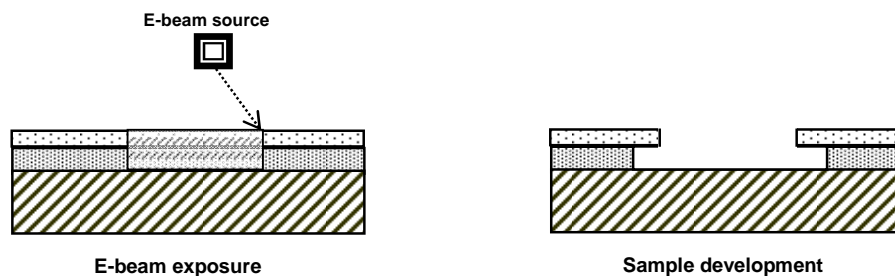


Figure 4 - 3 : Pattern transfer processes in a bi-layer e-beam resist system.

4.3 Metallisation and Lift-off

In the fabrication of antennas, the metallisation process is employed to form the antenna ground plane. Generally, metallisation is achieved by providing a patterned layer of resist material and depositing a blanket layer of desired metal. Unwanted metal is then removed by dissolving the resist and lifting off the metal. Depositing metal onto samples can be carried out in several different ways including thermal or electron beam evaporation and sputtering [87]. Electron beam evaporation was the main method employed in this work.

4.3.1 Electron Beam Evaporation System

Evaporation techniques rely on the heating of a metallic source to a temperature at which it vaporises. All evaporation processes can therefore be considered thermal. Electron beam evaporators locally heat the metal using electronic beam.

The electron beam is produced using a high accelerating voltage applied between a thermionic emission filament and the crucible, which acts as the cathode. The beam can be focussed on the metal surface and as a consequence of the interactions of the accelerated electrons with the metal; it is heated locally at the focussed spot. In thermal evaporators, there is the possibility of metallic contamination by evaporating the crucible if its melting point is similar to the target metal. In e-beam evaporators, as a consequence of the local heating, there is no possibility of such contamination, yielding a high-purity deposited film. Only the locally-heated region of the metal is evaporated, whilst the rest of the water-cooled source remains solid. There are, in addition, usually two shutters between the source and target. The purpose of these is to protect the sample from rate fluctuations during initial heating. When the evaporation rate is sufficiently stable, the source shutter can be opened, and the rate controlled using monitoring of the oscillation frequency of a quartz crystal and closed loop feedback. When the desired rate is reached, the upper substrate shutter can be opened, exposing the sample to the evaporated flux [91]. Figure 4 - 4 schematic diagram of an electron-beam evaporator system.

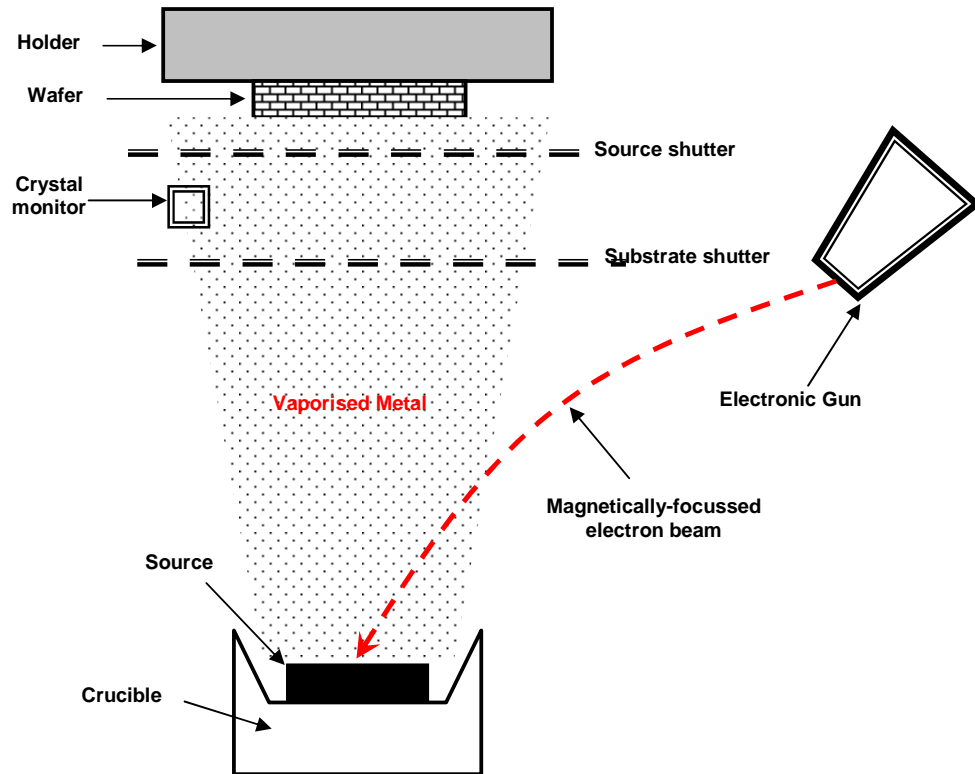


Figure 4 - 4 : Schematic diagram of an electron-beam evaporator system.

All evaporation processes must take place under high vacuum in the range of 10^{-6} to 10^{-7} Torr, since at these pressures, the evaporating metal flux has a mean free path greater than the distance to the target. As a result, there are few collisions of the metal whilst in flux, resulting in a highly directional metal coating on the sample, holder and chamber. Consequently, evaporated films are highly non-conformal to sample topography, since the incident metal flux is usually nominally normal to the surface.

Electron-beam evaporation processes were used in this work, using Plassys MEB 450 Electron Beam Evaporator (*Plassys I*) and a Plassys MEB 550S (*Plassys II*).

4.3.2 Metallisation and Lift-off Process

When the bi-layer resist sensitivities, exposures and development processes are correctly chosen, the resultant resist profile should be undercut, with the bottom layer more developed than the upper. As a result, using a directional evaporation process, the deposited metal film will be discontinuous at the edges of the exposed resist areas. In the exposed regions, the metal is deposited on the substrate; in the masked areas, the metal is deposited on the resist. By then soaking the sample in solvent, the resist can be dissolved, removing the metal deposited on top of the unexposed regions [95]. Figure 4 - 5 shows this process.

For high reliability, the deposited metal thickness must be less than the thickness of the bottom layer of resist. Prior to the metallisation, a sample was deoxidised by dipping shortly in a dilute solution of hydrochloric acid (HCl) in RO water.

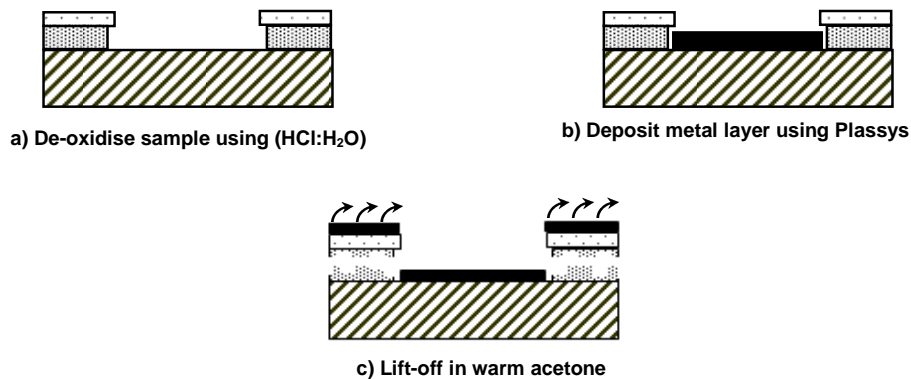


Figure 4 - 5 : Metallisation and lift-off process

4.4 Gold Electroplating

Electroplating or electrodeposition is a plating process that uses electrical current to deposit a desired material from a solution and coat a conductive surface with a thin layer of the material. Adherent metal film is deposited electrochemically by reducing a dissociated metal salt onto a negatively biased electrode. Standard electroplating solutions exist for a range of metals, including all noble metals. Electroplating is usually used when very thick layer of metal is needed to deposit. A dc electrical current in this technique is used to reduce the positive ionic of a desired metal from a plating solution and coat a conductive object with a thin layer of the metal. The anode and cathode in the electroplating cell are both connected to an external supply of direct current [96].

In many 3-D structures fabrication the use of gold electroplating is preferred because of its excellent corrosion resistance, solderability and bondability and its high electrical and thermal conductivity [97, 98]. In this research gold electroplating is used to form the elevated radiators of the antennas, air-bridges and elevated transmission line feeds. It is also used to fabricate beam cantilever of the MEMS switches.

4.4.1 Electroplating System

Figure 4 - 6 shows a schematic diagram of electroplating system which is used in this work. The anode is connected to the positive terminal, and the cathode (sample to be plated which is mounted onto the copper plate using wax and connected electrically to copper plate using silver paint) is connected to the negative terminal of a dc power supply. The plating dc current I_p can be set by using this equation [95].

$$\text{Plating Current (mA)} = (\text{sample holder area} - \text{sample area}) \text{ mm}^2 \times 0.013 \quad (4.1)$$

The cell is then filled with a gold plating solution to a level that would cover the cathode. Thermostatically controlled water bath are usually operated near 50°C ,

and the plating solution is agitated by a stirrer paddle. When the external power supply is applied, the metal at the anode is oxidized from the zero valence state to form cations with a positive charge. These cations associate with the anions in the solution. The cations are reduced at the cathode to deposit in the metallic, zero valence state.

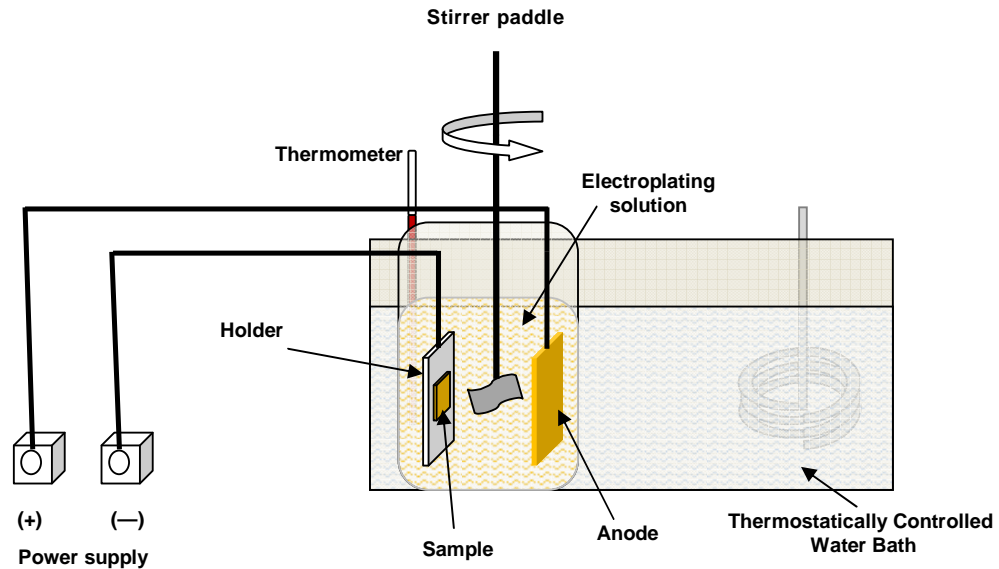


Figure 4 - 6 : A schematic diagram of electroplating system.

4.4.2 Electroplating Process

The gold electroplating process is shown schematically in Figure 4 - 7. In this process, the substrate is typically covered with a seed layer of conductive metal, which acts as the plating base and an underlying adhesion; also it prevents contamination of the plating solution (barrier layer). Typically these metal seed layers are deposited using sputtering or evaporation. The seed layer for gold electroplating usually is a two level metallization such as Ti/Au or NiCr/Au for good adhesion. The substrate is then patterned with a photoresist, and gold is selectively electroplated into the resist-free areas. Following plating of the structures to the desired thickness, the photoresist mask is stripped and the metal plating base is removed by wet etching [97].

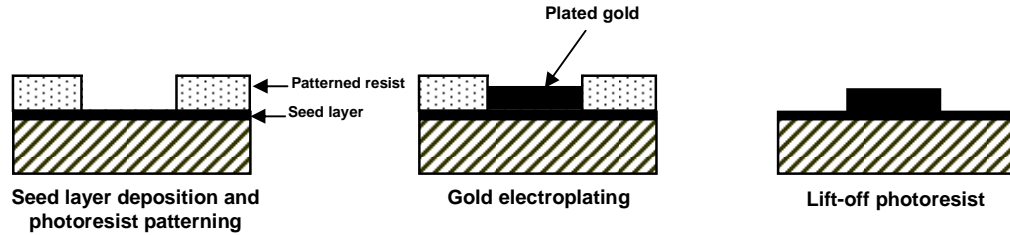


Figure 4 - 7 : Gold electroplating processes.

4.5 Sample Preparation

The antennas are built on a SI-GaAs wafer with a substrate thickness of $630\mu\text{m}$ and a dielectric constant of 12.9 . The wafer was scribed using a diamond-tipped scribing tool (rather than a pen) to keep the size and shape regular, and each single 50mm diameter SI-GaAs wafer scribed a different size based on the designed pattern. All scribed substrates are cleaned before subsequent processing to make sure that it is free from dust. An ultrasonic cleaning bath was used to clean the samples through the mechanism of cavitations. An acetone is the ideal solvent to clean organic contaminants from a sample. It is an organic solvent and hence will not react with any of the materials used in printed antenna fabrication. Further ultrasonic bathing in isopropyl alcohol IPA and then a reverse osmosis (RO) water rinse to remove any polar contaminants complete the procedure. Finally, the sample is dehydration baked in a 120°C oven to ensure that any water on the sample will be evaporated out.

4.6 Fabrication Process of 3-D Printed Antennas

Printed antenna fabrication makes use of many of the techniques covered in this chapter; specifically lithography, metallisation and electroplating. The antennas went through several fabrication steps and experience was accumulated through repeated fabrication and testing. In this project, the pattern definition of antenna ground plane is generally carried out using electron beam lithography, for its flexibility in addition to its superior pattern definition characteristics. Elevated structures realisation combines numerous individual process steps. Also, for good

antenna performance, the fabrication process of the antenna should be considered in the antenna design. This section will aim to describe the main purpose of each step to fabricate antennas.

4.6.1 Fabrication Process for Two Level Elevated Antennas

The fabrication of two level antennas is based on the development of a airbridge process [95, 99]. Figure 4 - 8 shows the fabrication process.

The first stage of fabrication is to define the antenna ground plane by e-beam exposure and development of a $1.5\mu\text{m}$ thickness of PMMA bi-layer, followed by electron beam evaporation and lift-off of a $50\text{nm}/1.2\mu\text{m}$ thickness nichrome/gold layer. This is the stage where accurate pattern transfer is most important as the photolithography and e-beam markers must be accurately reproduced to ensure that the alignment of subsequent layers is correct. Care is also taken at this stage to mitigate any stitching errors arising from tilt in the sample during pattern writing, by cleaning any traces of resist residing on the back surface after spinning. These could lead to the alignment markers being misplaced with respect to the centre of the pattern. Following this, the elevated structures (elevated radiators, elevated feeds and air-bridge tracks) are realized using a number of gold posts which offer a strong and rigid mechanical performance. These posts are defined in AZ4562 photoresist followed by backing and exposure. The thickness of photoresist will determine the height of the elevated structures. The thickness can be varied as required for optimum antenna performance by using different spinning speed. Table 4.1 shows the measured thickness of spun AZ4562 photoresist above the antenna ground plane at different spinning speed for *30 second*.

Table 4.1 : Measured thickness of AZ4562 photoresist above the ground plane

Spinning speed for 30second	Thickness of AZ4562 resist
<i>6000rpm</i>	<i>3.7μm</i>
<i>4000rpm</i>	<i>5.5μm</i>
<i>3000rpm</i>	<i>6.2μm</i>
<i>2000rpm</i>	<i>8.1μm</i>
<i>1500rpm</i>	<i>10.5μm</i>

The sample is now ready for developing in the ratio 1:4 (AZ400K:H₂O) and ashing in a dry etching machine. A 50nm Ti (titanium) layer and 10nm Au plating seed layer was then deposited using the Plassys MEB Electron Beam Evaporator. The Ti layer provides adhesion for the patch contact, and the 10nm Au layer prevents the Ti layer from oxidising. A 40nm layer of gold was then sputtered to provide electrical contact for the subsequent electroplating. Next, elevated structures were formed in 2 μ m thickness of S1818 photoresist followed by exposure and development and ashing in dry etching machine. Following the structures were electroplated with gold, which are the almost filled by the thickness of 2 μ m onto the seed layer. For large cross section area of the posts, 2 μ m of plated gold is not enough to fill all the hole areas of the posts. This fact affects the antenna performance and fabrication yield. Extra steps are required to full the posts with gold, which are: spinning a thin layer of S1818 potoresist followed by exposure using the posts mask and development. The whole areas of the posts are electroplated with desired thickness. The top layer of photoresist was removed by a flood exposure and development. The seed layer was then etched away in gold etching for 5 seconds to remove the Au followed by Ti etch in 4:1 buffered HF for 30second. Finally the bottom layer of AZ4562 is removed by a flood exposure and development. Figure 4 - 9 shows SEM photo for two level structure.

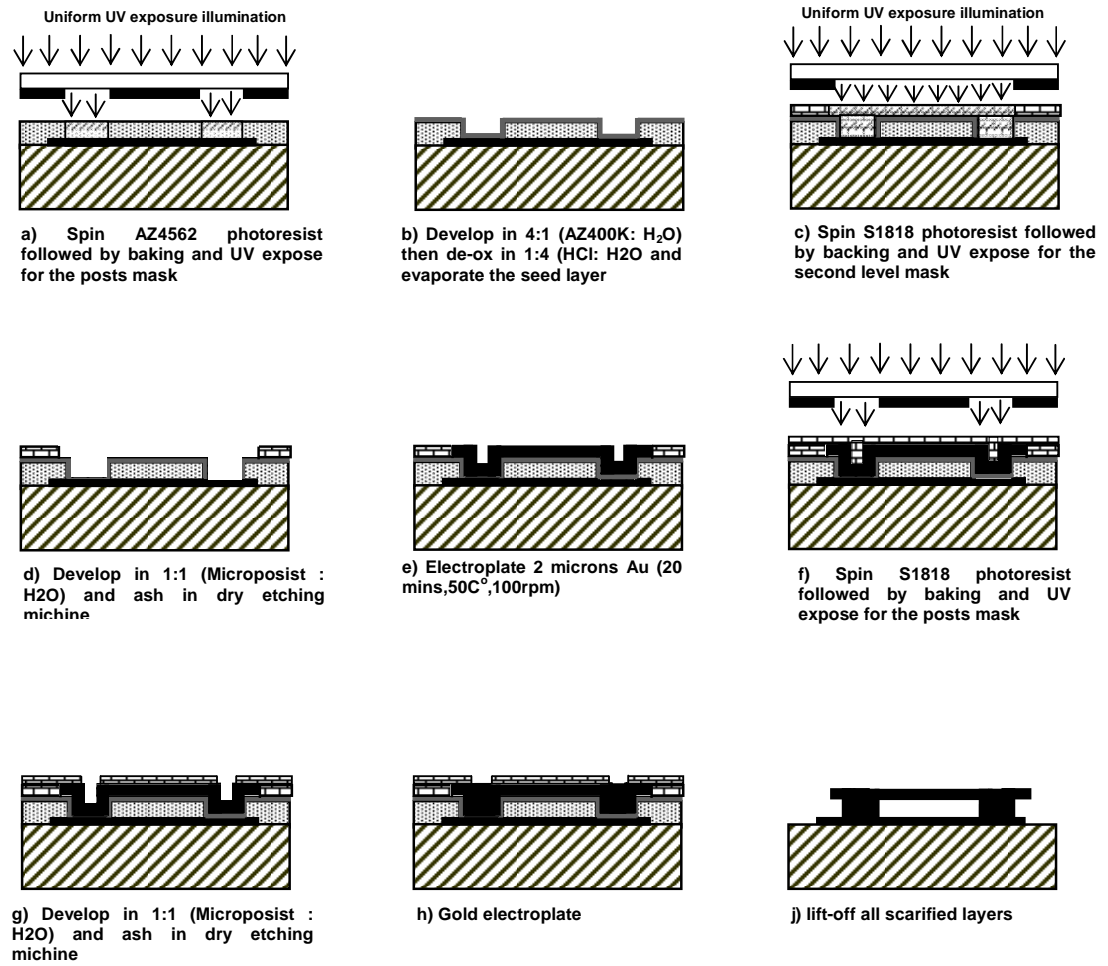


Figure 4 - 8 : Fabrication process of two level antennas.

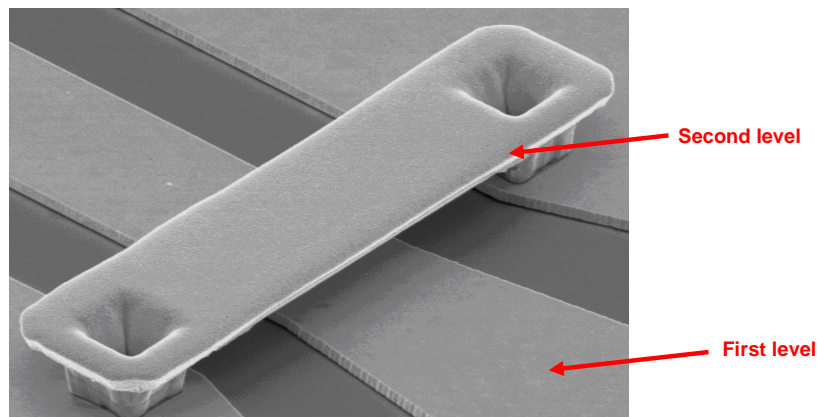


Figure 4 - 9 : SEM photo for two level structure.

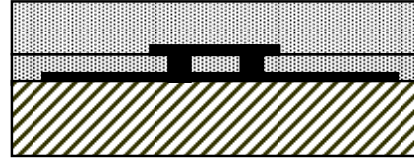
4.6.2 Fabrication Process for three Level Elevated Antennas

This section explains how to fabricate three level antenna structures using the photoresist as a sacrificial layer and four masks based on development a standard air-bridge process. Figure 4 - 10 shows the process flow used to fabricate the antennas. The desired structure has three levels of height; the first level consists of the antenna ground plane, then the elevated feed network and finally the radiator patch and air-bridge track.

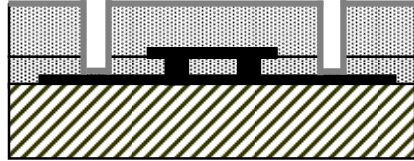
The first two levels (ground plane, feed network) are built with the same process, which have been discussed in the previous section, where the feed height above the ground plane can be varied as required for optimum antenna performance by changing the thickness of the first AZ4562 photoresist layer. Since there are several steps of lithography required, markers are required in each layer to align following exposures to the first. These markers are usually several microns in size, used in an edge location search to establish reference points across the plane of the substrate. Before fabrication of the third level starts, the top layer of S1818 photoresist and the seed layer have to be removed. The first layer of AZ4562 and the feed network structure are covered by AZ4562 photoresist layer, which is exposed and developed to form the radiator post patterns. The height of the radiator is determined by the total thickness of the first and second layers of AZ4562 photoresist and it can be varied as required for optimum antenna performance by changing the thickness of the second resist layer. The other steps of the third level which are employed include photolithography and electroplating techniques, which are used to form the two level structures. Figure 4 - 11 shows SEM photo for three level structure.



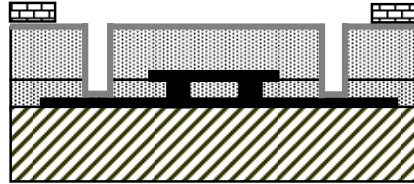
a) Flood expose and develop followed by etch Au and Ti



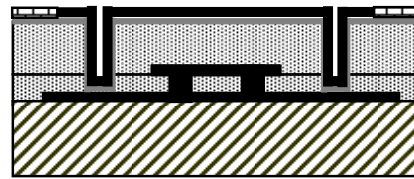
b) Spin AZ4562 photoresist followed by UV expose for the posts mask



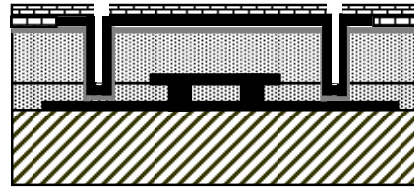
c) Pattern development then de-ox and evaporate the seed layer



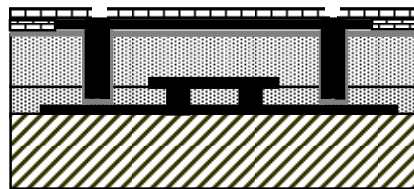
d) Spin S1818 photoresist followed by exposure and development for the radiators mask



e) Electroplate 2µm of gold



f) Spin S1818 photoresist followed by exposure and development for the posts mask



g) Gold electroplate



i) Lift-off the photoresists and etch the Ti/Au seed layer

Figure 4 - 10 : Process flow used to fabricate three level antennas.

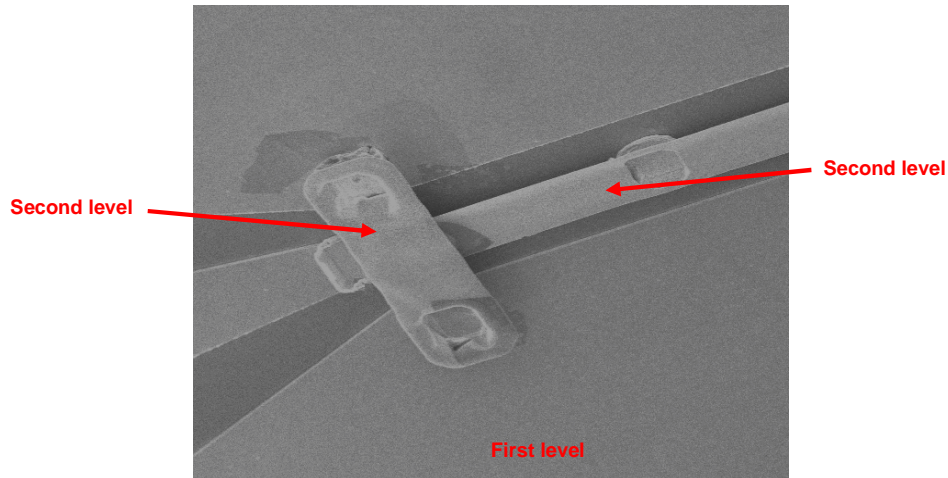


Figure 4 - 11 : SEM photo for three level structure.

4.7 Conclusions

The development fabrication process provides a new method for 3-D multilevel structures without etching the substrate. Also, the height of the elevated antennas can be specified in the process and can vary by several microns, regardless of the substrate used. This can be used to further enhance the antenna bandwidth when we cannot change the substrate thickness for the sake of the rest of the module circuits. Thus, the elevated antenna can meet different application requirements and be utilized as a substrate independent solution. Gold was used as a metal since it is widely used owing to its performance and low resistivity characteristics. For the substrate, GaAs material is used, although the process is compatible with the integration of other RF components onto different substrate materials, facilitating the application of this antenna in fully integrated MMICs. This novel process technique may play an important role in the fabrication of the state-of-the-art, reliable micromachined devices.

5. Micromachined Elevated Antenna Designs

5.1 Introduction

To increase the performance of millimetre-wave systems, an antenna with high gain, broad bandwidth and fully integrated with MMIC circuitry is required. Micromachined elevated antennas, which will present in this chapter, are highly valued for their ability to provide such characteristics for these systems.

Antennas are designed as a single element at G-band (140GHz to 220GHz) on a high dielectric substrate, taking into account manufacturing tolerances and measurement facilities used in testing the functionality of the antennas. The first part of this chapter discusses several new feeding mechanisms for elevated micromachined printed antennas. CPW and elevated feed lines were used as they offer a greater degree of freedom for the elevated antenna design. Different, new, configurations of elevated printed antennas with different feeding techniques have been also designed during this work. Other antennas are under investigation and their configurations are shown in the Appendix A. The investigated antenna configurations include: elevated rectangular patch antenna, CPW fed elevated bow-tie antenna, proximity coupled elevated patch antenna, EC-CPW fed elevated patch antenna, and EMS fed elevated overlapped patch antenna. The end of the chapter concentrates on new designs for three level patch antenna structures. Simulation and measurement results for basic antenna parameters such as return loss, bandwidth, and radiation pattern are presented and demonstrate the feasibility of G-band micromachined antennas on high dielectric substrates.

5.2 Feeding Mechanisms of Elevated Printed Antennas

The increased interest in the monolithic integration of antennas with RF circuits has led to many new configurations with different feeding techniques. For good antenna performance, a low loss feed is desirable since this will provide better radiation efficiency. New feeding mechanism techniques for elevated micromachined antennas are proposed in this research for the first time. These techniques will be discussed in this chapter.

5.2.1 Coplanar Waveguide CPW

A coplanar waveguide CPW is the first feeding mechanism we studied in order to feed elevated micromachined antennas. This is because a CPW structure has many interesting advantages over conventional transmission lines at millimetre-wave frequencies [3, 57, 100], as we discussed in section 2.7.1 chapter 2. Two methods have been introduced in this work to feed an antenna using a CPW line. Firstly, an elevated antenna radiator is excited by feeding a metal post directly connected with the radiator, and it also vertically mounted at the end of the centre conductor of the coplanar waveguide (CPW) line underneath the radiator. A second method is to indirectly excite the radiator. Here, the antenna radiator is excited by electromagnetic coupling using a slot formed in the ground plane and connected with the end of the CPW feed line.

In both methods, the centre conductor width W and the gap S between the centre conductor and the ground planes of the CPW were designed to have a characteristic impedance of 50Ω to couple the antenna effectively with the measurement system. The CPW dimensions are calculated using LineCalc in Agilent ADS and optimized with Ansoft HFSS simulation software as follows: $W/S=20\mu\text{m}/15\mu\text{m}$. Also, in order to obtain compatibility with the measurement system, a 50Ω CPW taper probe pad ($W/S=60\mu\text{m}/40\mu\text{m}$) is required in the antenna design to provide a smooth transition between the two different line geometries. Figure 5 - 1 shows the configuration of the CPW feed mechanism connected with feeding post.

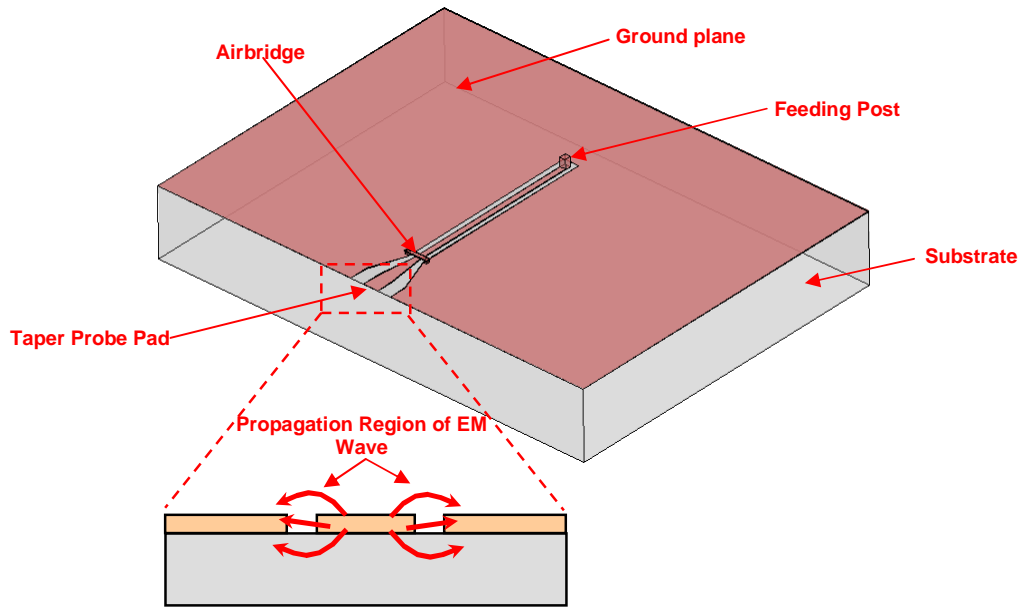


Figure 5 - 1: Configuration of the CPW feed mechanism with feeding post.

The main advantage of this mechanism is that the feeding post or the feeding slot can be adjusted to an appropriate location to obtain a suitable input impedance of the antenna. Therefore, the antenna can be directly matched to various input impedances, and the $\lambda/4$ impedance transformer which is used in the edge feeding method is not required. Furthermore, a CPW feed line can be optimized separately like aperture coupled antenna and hence the need for a compromise between radiation and propagation requirements can be avoided.

However, for CPW at frequencies $< 60GHz$, $\lambda/4 \gg$ substrate thickness (normally $100-650\mu m$) and the dimensions (ground-signal-ground) \ll substrate thickness, the substrate moding effect is found to be negligible. Hence, dielectric and metal losses are the only dominant factors to be considered when characterised. At millimetre-wave frequencies above $140GHz$ the above mentioned conditions do not hold, substrate thickness comparable to $\lambda/4$ and CPW dimensions (ground-signal-ground) comparable to substrate thickness. This results in a strong moding effect and high dielectric loss which must be taken into account for deep millimetre-wave antenna and packaging [13, 58]. Also, the CPW line suffers from limited usable impedance ranges. This is due to the fact that the line losses of the

CPW line tend to increase rapidly at low-impedance and at high-impedance extremes. Furthermore, CPW suffers from the excitation of the parasitic slot-line mode at asymmetric discontinuities like bends and T-junctions. This mode propagates at a different velocity from the dominant even CPW mode and causes more radiation to free space - as shown on Figure 5 - 2 - a. The conventional method for eliminating the unwanted mode is the use of air-bridges to equalize the ground planes along the feed line as shown in Figure 5 - 2 - b [58, 101, 102].

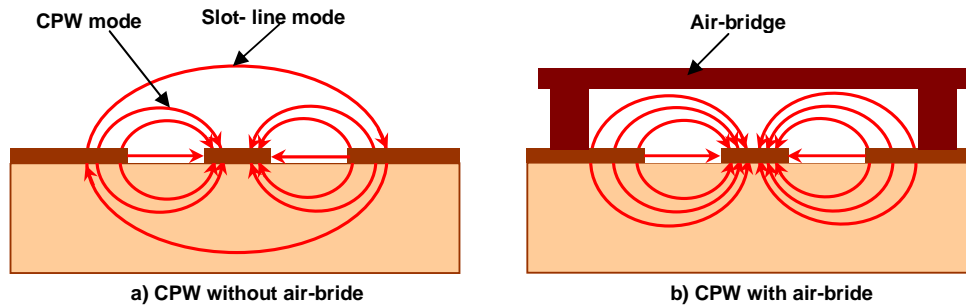


Figure 5 - 2 : Excitation of the parasitic slot-line in a coplanar waveguide.

5.2.2 Elevated Transmission Lines

Low loss transmission lines are one of the most important components for extending the frequency limits of the planar antennas. Conventional CPW on high dielectric substrates at G-band frequencies suffers from many drawbacks as we explained in previous section. To improve the poor performance of conventional CPW, there have been attempts to reduce the loss of the transmission lines at millimetre-wave frequencies by using elevated transmission feed lines [3, 66, 81, 103, 104].

The elevated feed lines structure offer several advantages such as [12, 66, 105]: First, they enable the realization of high-impedance lines without reducing their widths, thus, minimizing the dependency of the structure on the manufacturing tolerance and reducing the conductor loss. Second, the area above the ground lines can be utilized to form metal insulator metal capacitors, to load the elevated lines without increasing the chip-area. Third, these feed topologies effectively

eliminate undesired substrate moding effects (surface wave) at millimetre-wave frequencies, since most of the electric field is confined in the air between the elevated line and the ground plane, rather than, in the substrate. Finally, using elevated transmission lines can reduce the associated capacitive dielectric losses and associated energy lost through Joule's heating, because of propagation region is air which is gives the lowest capacitance.

Two kinds of elevated feed line structures were initially proposed in this work to overcome the problem of high losses that are found in conventional CPW implementations. This is a new feeding mechanism for elevated micromachined antenna and presents, for the first time, more degrees of freedom for antenna design. These two kinds of elevated feed lines are Elevated Conductor Coplanar Waveguide EC-CPW and Elevated Microstrip EMS line. The configuration of these feed lines is shown in Figure 5 - 3.

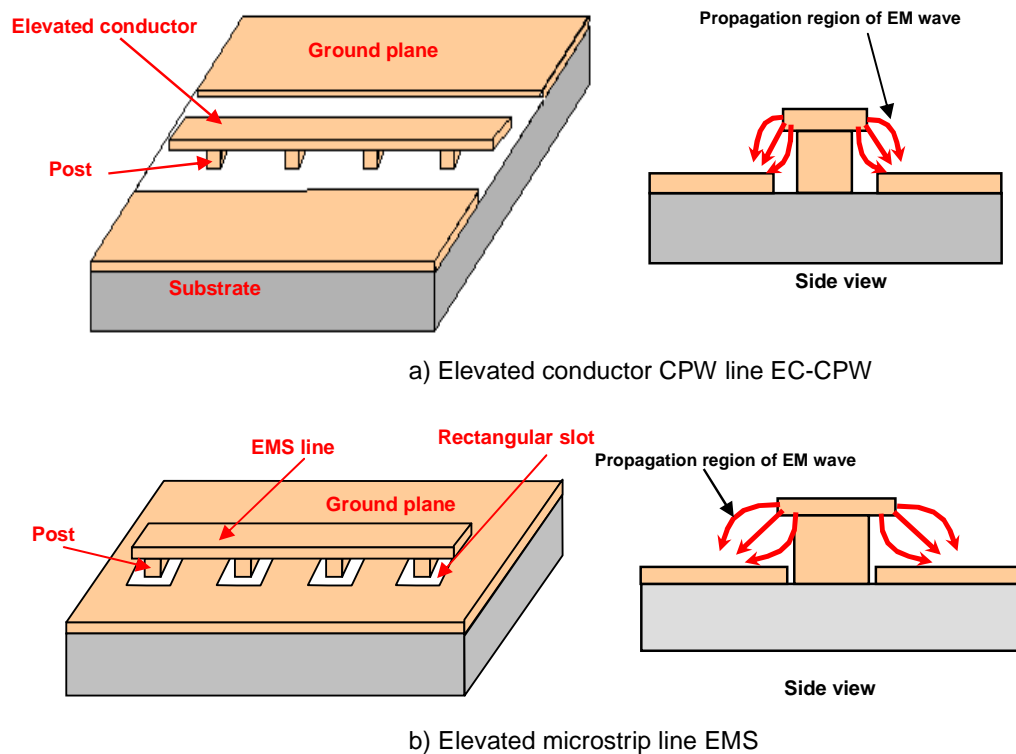


Figure 5 - 3 : Elevated feed lines configurations (EC-CPW and EMS).

The centre conductor of the CPW was elevated above the substrate by using gold posts of $20 \times 20 \mu\text{m}^2$ cross-section and a height of $5.5 \mu\text{m}$. Similarly, the elevated microstrip was elevated in the same way with the posts positioned within rectangular slots of $25 \times 25 \mu\text{m}^2$ in the ground plane. The input impedance of these feed lines can be set by adjusting the height, width of the signal line trace and the gap between the signal line and the ground planes.

The measured insertion losses S_{12} of the conventional and elevated CPW lines are shown in Figure 5 - 4. The EC-CPW dimensions are calculated using LineCalc in Agilent ADS and optimized with Ansoft HFSS simulation software as follows: $W/S=26\mu\text{m}/11\mu\text{m}$. Both transmission lines, elevated and conventional, have the same length of 1.5mm and characteristic impedance of 50Ω and with the same ground size, so that a valid comparison can be made. As shown in Figure 5 - 4, ECPW line shows an improvement in loss across G-band frequencies region. For example, the conventional CPW loss at 220GHz is about 8.4dB , while EC-CPW has an only 6.8dB . The reduction in loss is attributed to the screening of substrate loss for EC-CPW structures, since most of the electric field is confined in the air between the elevated line and the ground plane, rather than, in the substrate. This shows that the elevated feed structures are more efficient than conventional CPW for antenna feeding at G-band, and they can offer valuable advantages of a variety of feed lines configurations and layout flexibility.

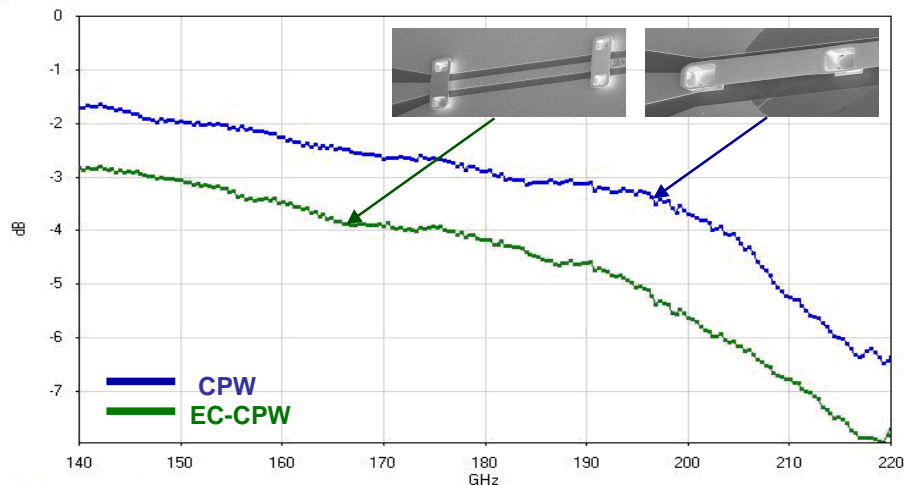


Figure 5 - 4 : Comparison of measured losses for CPW and EC-CPW as a function of frequency

5.3 Elevated Rectangular Patch Antenna

A class of micromachined printed antennas that are particularly well suited for operation at G-band frequencies are elevated patch antennas. An elevated patch antenna in its simplest form consists of a radiating patch elevated over a ground plane using posts on one side of a dielectric substrate. The radiating patch could be of any arbitrary shape, but a rectangular patch was chosen in this design to provide linear polarization, broadside radiation and ease of analysis and understanding of the elevated antenna characteristics. The antenna is fed using CPW connected with a feeding post [12-14].

5.3.1 Antenna Design

The configuration of antenna design is shown in Figure 5 - 5. To reduce the dielectric substrate loss, the rectangular patch is elevated above a CPW ground plane by gold posts. By elevating the patch, the antenna topology effectively will create a low dielectric substrate since the antenna substrate is essentially air, which is the lowest possible dielectric constant. This will help increase the radiation efficiency, gain, and the bandwidth. The patch height is chosen after considering the following factors: first, the greater the elevation, the greater the bandwidth. Secondly, the more elevation, the more difficult the fabrication is and the more fragile the micromachined structure will be. A height of $5.5\mu\text{m}$ is a good choice taking all of these concerns into account. Also, the number of gold posts and their volumes were determined considering the trade-off between electrical performance and mechanical robustness. A large number of posts would offer a stronger and more rigid mechanical performance at the expense of an increase in back lobe radiation and difficult to match. In this design, the smallest possible number of posts, while maintaining mechanical robustness, is decided as eight; one gold supporting post is used for each patch vertex and one for each middle point of the patch length edge. In order to decide appropriate dimensions for the antenna and an optimum design, investigation was performed using the simulation software HFSS. The effects of different aspects of the antenna structure on the response will be determined in the following section.

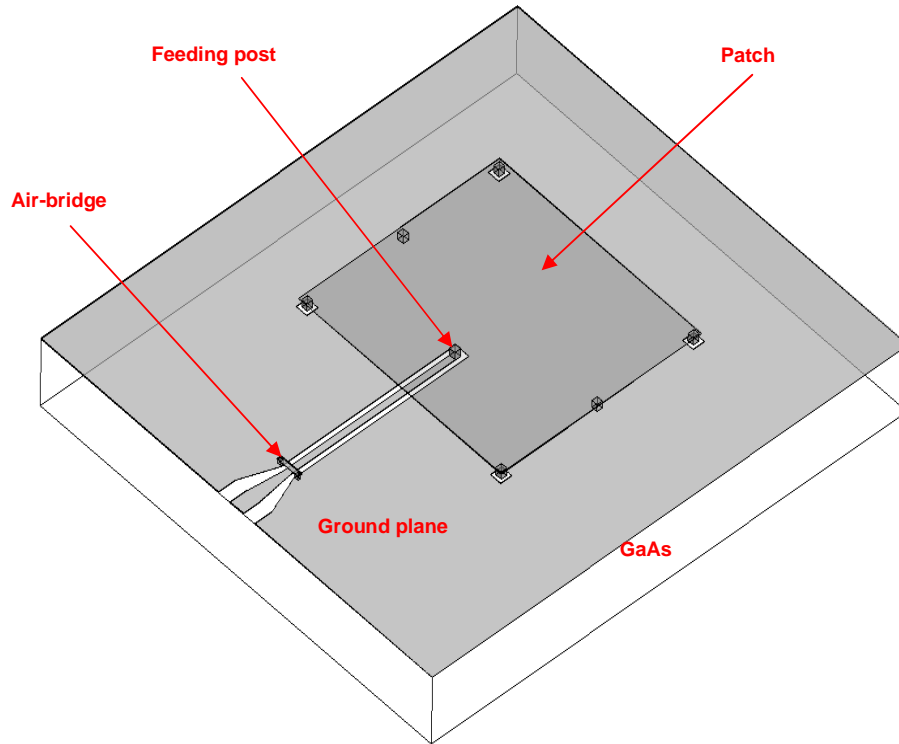


Figure 5 - 5 : Configuration of rectangular elevated patch antenna design.

Radiating Patch Element

The physical specifications and operation frequency of the elevated patch antenna have been determined based on design considerations which have been discussed in chapter three. The initial dimensions of the elevated patch were $L \times W = 0.749\mu\text{m} \times 0.857\mu\text{m}$, which were calculated based on transmission line mode equations (see section 3.2.1) at the desired frequency. The antenna configuration then optimized using HFSS simulation software. The antenna operating frequency is determined mainly by the patch length L , which generally is in the range of $0.3333\lambda_0 < L < 0.5\lambda_0$, where λ_0 is the free space wavelength at resonant frequency. The elevated patch is designed and optimized to resonate at G-band. The final size of a prototype patch was $L \times W = 746\mu\text{m} \times 806\mu\text{m}$ with $5.5\mu\text{m}$ height and $2\mu\text{m}$ thickness.

The height of the patch has an impact on the resonant frequency and antenna radiation performance. For example, increasing the patch height will enhance the fringing fields from the patch radiating edges; this will reduce the antenna resonant frequency and increase the antenna gain. The decreasing in the resonant frequency comes from increasing the effective length of the patch. Also, the input impedance locus shifts in the right direction on the Smith chart implying that the impedance is increasing. The increasing in the imaginary part of the antenna input impedance comes from the antenna itself as the capacitance underneath the patch becomes less with increasing the patch height, whereas the increasing in the real part (resistance) comes from increasing of fringing field between the patch and ground plane. Further, increasing the patch height will allow more space between the ground and the patch. The more space for storing energy makes the antenna wider bandwidth. Figure 5 - 6 shows the effect of the patch height on the input antenna impedance. However, too large a patch height will increase the cross polarization level because of the increase in the posts length, which act as a monopole antenna underneath the patch whose radiation increases with the increase in its length.

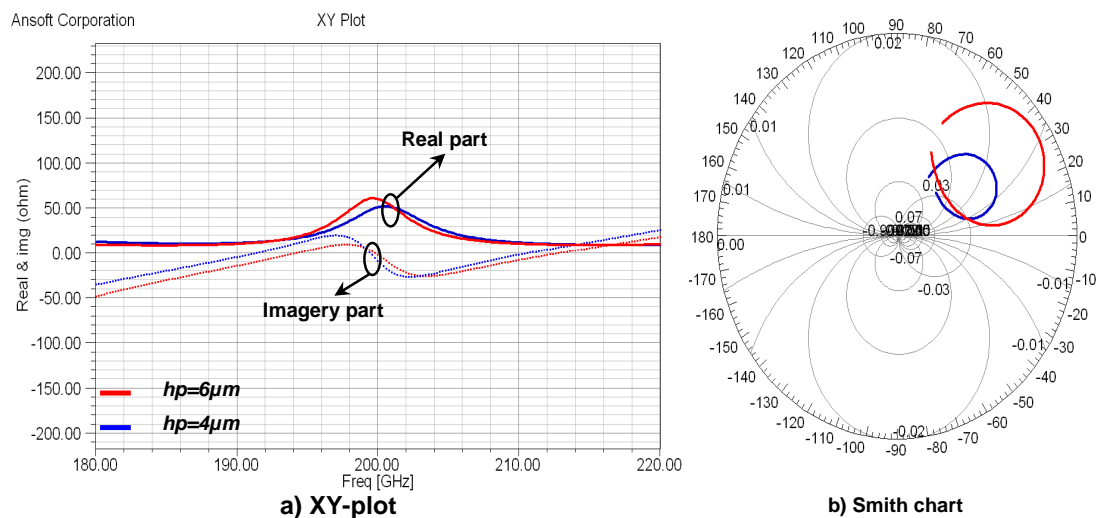


Figure 5 - 6 : effect of the rectangular patch height on the antenna impedance.

The patch width has also an important effect on antenna performance, which can be increased to enhance the fringing fields from the patch radiating edges. As a result, the antenna gain and bandwidth will be increased, and also HPBW (half power beam-width) at the H-plane will increase whereas it remains almost the same in the E-plane. However, increasing the patch width too much leads to excited higher order modes and a square patch results in the generation of high cross polarization level as explained in section 3.2.1.

Feeding Mechanism

The patch is fed by a gold feeding post connected to a CPW feed line on gallium arsenide (GaAs) substrate. The feeding post is placed in the middle of the width of the patch to avoid the excitation of the orthogonal TM_{01} mode. For the fundamental TM_{10} mode, the impedance of the patch varies from a zero value at its centre to the maximum value at the radiating edges. By tuning the elevated patch antenna to the desired frequency, the feeding post must be located at that point on the patch where the input impedance is equal to 50Ω at the resonant frequency. Hence, a trial and error method is used in this design to locate the feed point using HFSS simulation software. For different locations of the feed point, the return loss (R.L) is compared and that feed point is selected where the R.L is the highest. A perfect match with a 50Ω feed line is obtained at $193\mu\text{m}$ off the patch radiating edge.

Ground plane

The ground plane has to be large enough to reduce diffraction of the edges for reducing ripples in the main pattern and backward radiation, and to shield the antenna from the underlying elements and vice versa. The transmission line model is applicable to infinite ground planes only. However, for practical considerations, it is essential to have a finite ground plane. It has been shown by [9, 24] that similar results for finite and infinite ground plane can be obtained if the size of the ground plane is greater than the patch dimensions by approximately six times its height all around the periphery. Hence, for this

design, the ground plane dimensions were chosen as $W_s \times L_s = 1.5\text{mm} \times 1.65\text{mm}$ with $1.2\mu\text{m}$ thickness of gold to reduce the antenna ohmic losses.

The antenna was built on a GaAs substrate with a substrate thickness of $630\mu\text{m}$ and a dielectric constant of 12.9. The two level antenna process, which is based on air-bridge process, was used to fabricate the antenna. Figure 5 - 7 shows a SEM photo of fabricated antenna which has been measured to evaluate its performance.

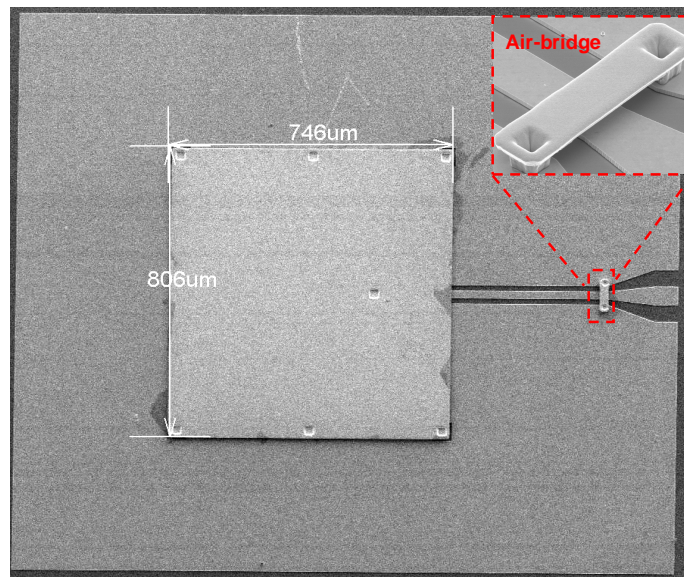


Figure 5 - 7 : SEM photo of fabricated elevated rectangular patch antenna.

5.3.2 Analysis of Results

The measured return loss of the elevated patch antenna is plotted along with the simulation results in Figure 5 - 8. The measurement result shows good agreement with simulation in the return loss between 140GHz and 220GHz for the proposed antenna. The slight shift in resonant frequency can be attributed to the small geometrical disparity between the fabricated prototype and the simulated one. However, this can be easily overcome in an industry manufacturing process where all of the fabrication conditions are optimized for a specific process. The

measured $10dB$ bandwidth is about $7GHz$ from $170GHz$ to $177GHz$ at $172.5GHz$ resonant frequency.

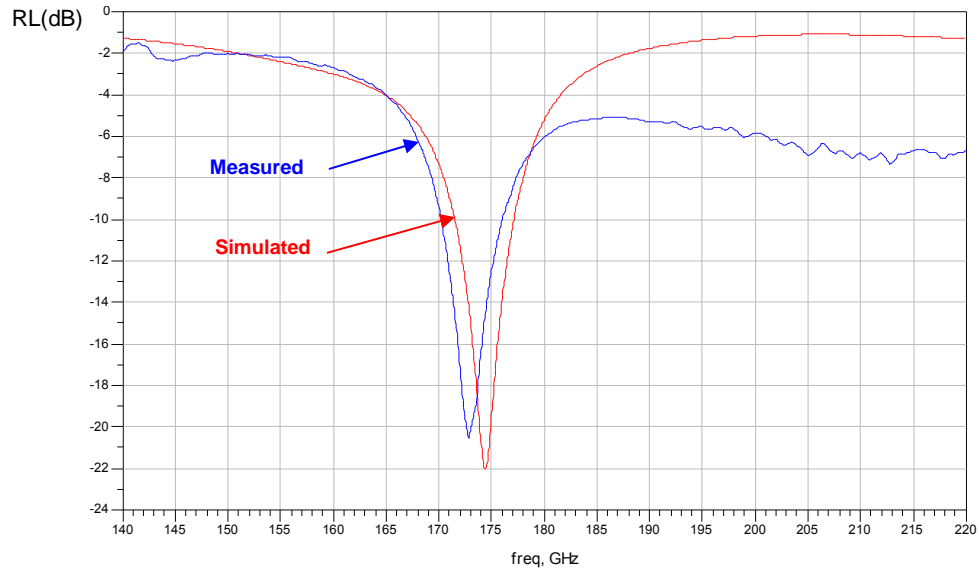


Figure 5 - 8 : Simulated and measured results of elevated patch antenna return loss.

The proposed antenna demonstrates a nearly symmetrical and broadside radiation pattern with low side lobes over its bandwidth. Since the elevated patch antenna radiates normal to its patch surface, the elevation pattern for $\theta = 0^\circ$ (XZ-plane) and $\theta = 90^\circ$ (YZ-plane) would be important, therefore Figure 5 - 9 shows these planes at the resonant frequency. The maximum antenna gain is $2.6dB$ with $3dB$ beam width of 64° in the XZ-plane and 59° in the YZ-plane. The gain diminishes slowly towards the edges of the antenna bandwidth, and falls sharply for frequencies out-of-band. It is postulated that this is due to significant surface-wave generation outside the impedance bandwidth of the antenna as the energy is no longer strongly coupled to the parasitic patch element. Another effect of this surface-wave generation is the high out-of-band return loss of 4–5 dB.

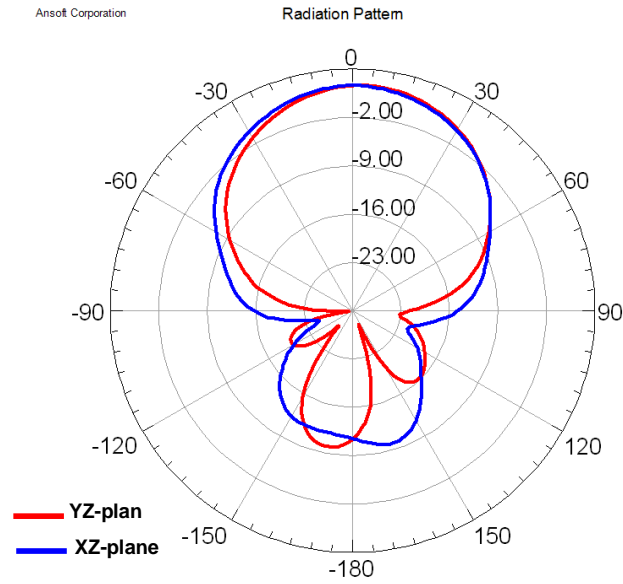


Figure 5 - 9 : XZ and YZ plane of patch antenna radiation pattern (gain).

Also, the pattern is found to be stable across the whole bandwidth of the antenna with a front-to-back ratio of 8 dB (worst case) and efficiency of 30.23%. Figure 5 - 10 shows the simulated 3-D radiation pattern of the antenna directivity at the resonance frequency.

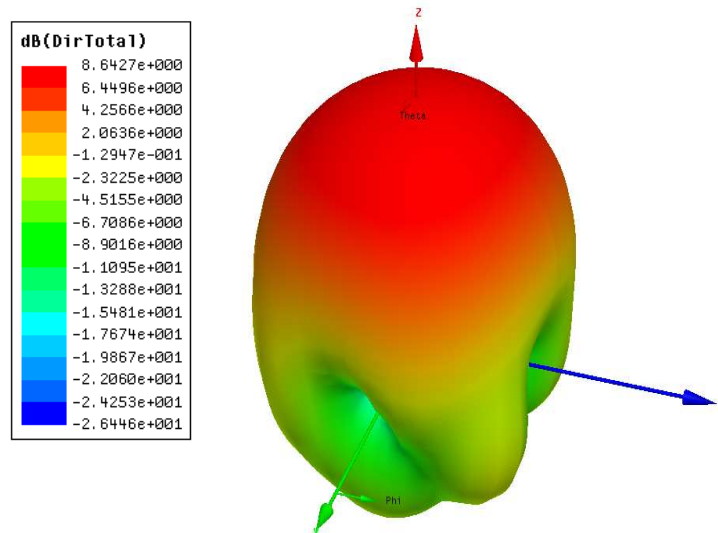


Figure 5 - 10 : 3-D radiation pattern of elevated rectangular patch antenna directivity.

The antenna scheme offers an easy method to integrate antenna with other MMICs, eliminate the most undesired substrate effects and maximize antenna performance on high dielectric substrates. Also, because there is no need for an additional transition, a single chip wireless millimetre-wave system including the antenna can be achieved with a very compact size, low cost, and high performance. Further, because the CPW feed line is formed on the substrate and the radiating patch is lifted in the air, the radiating patch and the feed line can be optimized separately like aperture coupled antenna.

5.3.3 Comparison with Conventional Patch Antenna

A conventional edge-fed microstrip patch antenna directly printed on top of GaAs substrate with the same elevated patch dimensions was simulated using HFSS simulation software to compare its performance with the elevated patch antenna. Figure 5 - 11 shows the return loss of the patch antenna directly printed on the substrate. It can be clearly observed that the antenna loss is very high and increases with frequency and there is no clear resonant frequency. This because as we explained in section 3.2 at G-band frequencies there is possibility to excited seven surface wave modes in the GaAs substrate, the first mode TM_0 has zero cut-off frequency and last mode TM_6 has cut-off frequency of $207.06GHz$.

Also, the elevated patch antenna has demonstrated a significantly improved radiation performance than the conventional patch antenna directly printed on top of the same type of substrate. The maximum predicted directivity for the elevated patch is $8.6dB$ with the front-to-back ratio of $8dB$ and lower side lobe regardless of suspension height, showing high radiation efficiency of the antenna structure. A non-elevated patch on the same substrate gives a maximum predicted directivity of $4.8dB$ with a bad front-to-back ratio of $0.203dB$, but no longer at the broadside direction as a consequence of surface wave triggered in this electrically thick dielectric substrate, as shown in Figure 5 - 12. It can be clearly observed that there is a deep drop in the antenna radiation performance without elevation due to the diffraction of surface

waves at the edge of the substrate. In contrast, the elevated patch has a clear main beam in the z-direction.

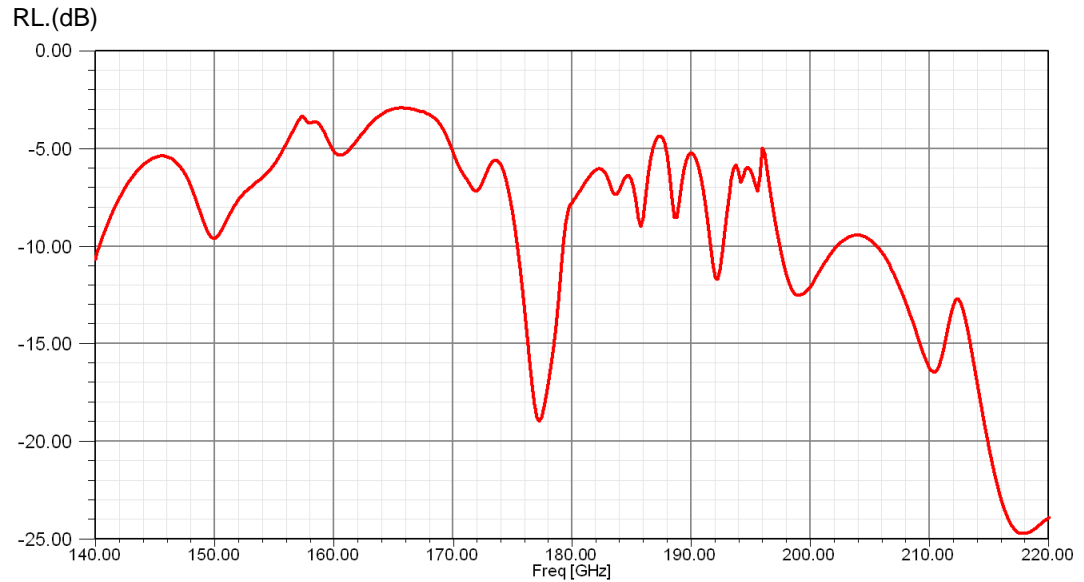


Figure 5 - 11 : Return loss of the patch antenna directly printed on the substrate.

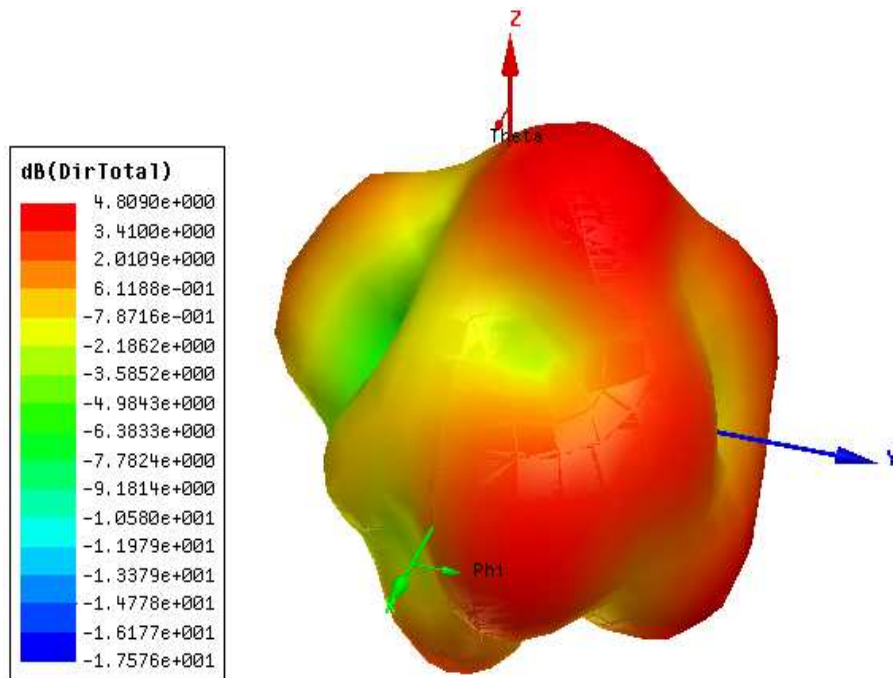


Figure 5 - 12 : 3-D radiation pattern of the patch antenna directly printed on the substrate.

5.4 CPW Fed Elevated Bow-tie Antenna

Bow-tie antennas have become attractive candidates in many present day communication systems due to their compact nature compared with rectangular patch antennas. This section provides a new design of an elevated bow-tie antenna fed by the same technique which has been used in last design. The main goal of this new design is to reduce the substrate effect coupled with small size and MMIC compatibility.

5.4.1 Antenna Design

Figure 5 - 13 shows the configuration of the elevated micromachined bow-tie antenna. The elevated bow-tie antenna actually is the combination of the imaginary image of two triangular patches which are elevated above a single substrate; hence the design of bow-tie antenna is based on the design of a triangular antenna. Also, formulas that are used in the design of triangular printed antenna to calculate the side length are also applicable in the design of elevated bow-tie antenna. Because the antenna substrate is essentially air $\epsilon_r = 1$, the antenna resonant frequency for TM_{mn} mode can be written as [24, 61]:

$$f_{mn} = \frac{2c}{3a_e} \sqrt{m^2 + mn + n^2} \quad (5.1)$$

Where: f_{mn} is the resonance frequency, m and n are the order of various resonant modes, c is the velocity of light in free space, and a_e is the effective side length of the triangle radiator which can be quickly estimated using the following approximate formula

$$a_e = a + 4h_p \quad (5.2)$$

For the fundamental TM_{10} mode, the vector representation of the field variation along the periphery of radiator is shown in Figure 5 - 13. A larger arrow size is used to show that the magnitude is larger.

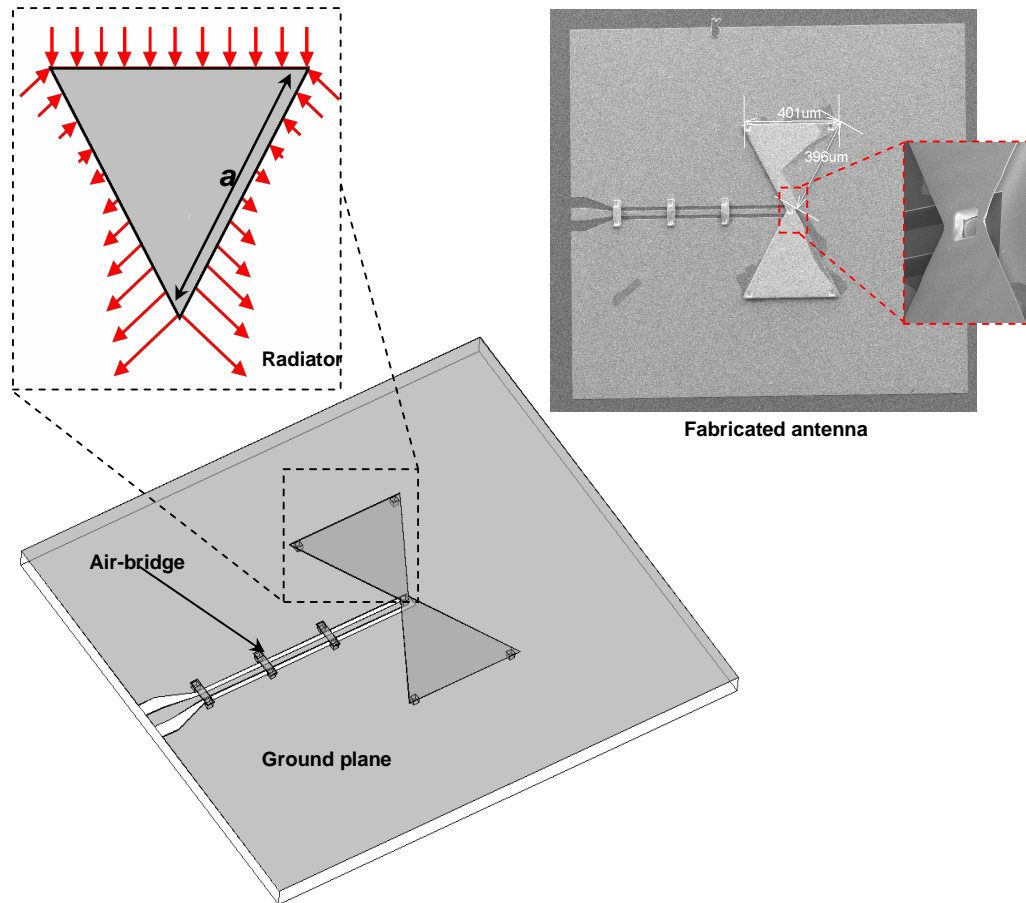


Figure 5 - 13 : Configuration of elevated micromachined bow-tie antenna.

The antenna fabrication is based on elevated micromachined structures technology on GaAs substrate with a substrate thickness of $630\mu\text{m}$ and a dielectric constant of 12.9 . The two identical triangle radiators of bowtie antenna are joined together at the apex and elevated by gold posts of height $5.5\mu\text{m}$. The side length of triangle radiators was calculated and then optimized using HFSS simulation software at desired frequency and it is $396\mu\text{m}$, while the other lengths are depends on the flare angle (flare angle is not less than 0° and not bigger than 180°). The antenna topology creates a low dielectric substrate and undesired substrate effects will be eliminated, since the antenna substrate is essentially air. Therefore, the type and thickness of the dielectric substrate can be varied without significant change of antenna performance. This will allow the use of high dielectric substrates with different thicknesses.

The antenna was fed with the same method which has been used in rectangular patch antenna using CPW feed line via micromachined gold post. The CPW was designed to have an input impedance of 50Ω using HFSS software ($W/S=20\mu m/15\mu m$) to couple the antenna effectively with the measurement system. Parameters such as flare angle and side length of the bow are optimized using HFSS software to match to a 50Ω input impedance. The ground planes of CPW are composed of the air-bridges, which are used to eliminate the unwanted mode of the CPW feed line (slot line mode). The CPW ground plane will act as a reflector and it will totally shield the antenna from the underlying elements. The size of the ground plane on top of the GaAs substrate is $W_s \times L_s = 1.5mm \times 1.65mm$, which is large enough to reduce diffraction of the edges for reducing ripples in the main pattern and backward radiation.

5.4.2 Analysis of Result

The acceptable return loss for a printed antenna is $10dB$ or higher. It is preferable if the antenna having the return loss of higher than $20dB$. By comparing the simulation results and the measurement results, the measurement return loss shows good agreement with simulation. The slight shift in resonant frequency can be attributed to the fabrication tolerance between the fabricated prototype and the designed one. The measured $10dB$ bandwidth is about $8.6GHz$ at $209GHz$ resonant frequency from $204GHz$ to $212.6GHz$. Figure 5 - 14 shows the measured and the simulated results of the $5.5\mu m$ height elevated bowtie antenna. Also, proposed antenna demonstrates bidirectional radiation pattern with maximum directivity of $5dB$. Figure 5 - 15 shows the simulated 2-D E and H plane radiation pattern.

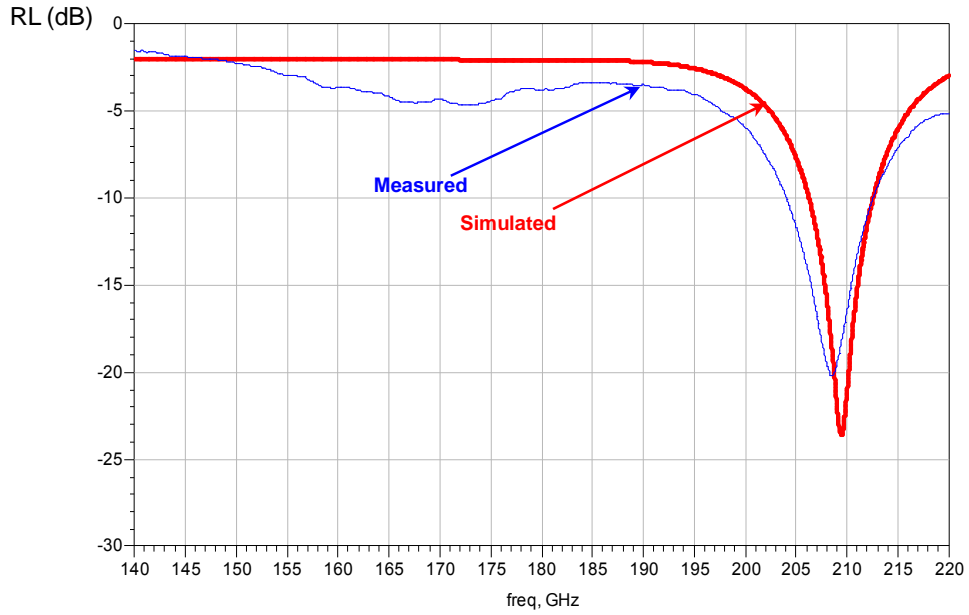


Figure 5 - 14 : Simulated and measured return loss of elevated bow-tie antenna.

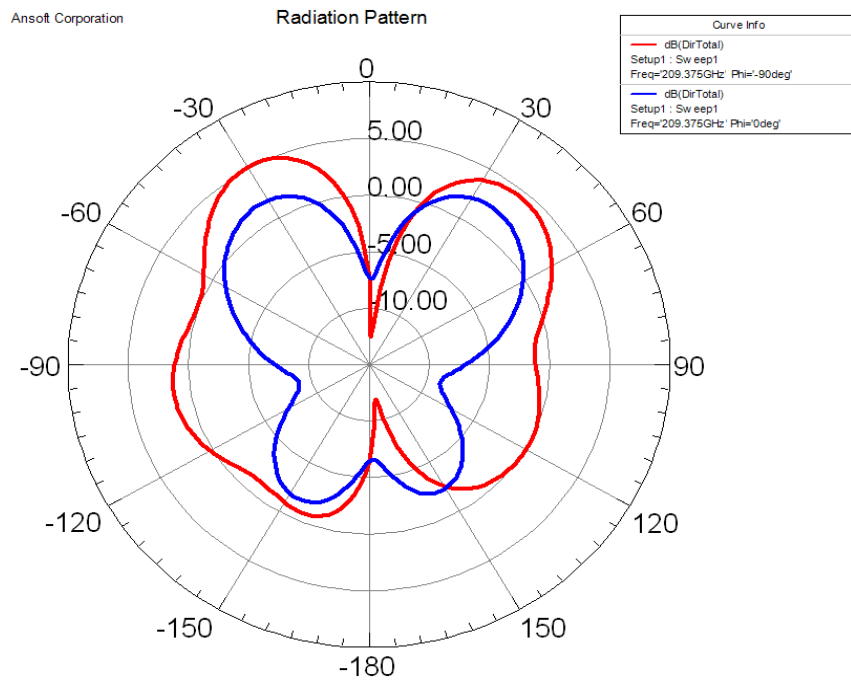


Figure 5 - 15 : E and H plane of elevated bow-tie antenna radiation pattern (directivity).

5.5 Proximity Coupled Elevated Patch Antenna

Many techniques have been introduced in order to overcome the narrow bandwidth of the patch antenna as we have discussed in chapter two. The CPW fed proximity coupled patch antenna approach can be considered as an alternative to increase antenna bandwidth [57, 106]. In particular, a loop slot proximity coupled patch antenna gives symmetrical coupling between the feed and the radiating patch, and it can be used for reconfigurable antennas by using a short or open loop slot [107]. However, all loop slot proximity coupling antenna designs have been achieved by using separate substrates, which have to be aligned exactly to achieve good performance. It is very difficult to align the substrates exactly and small misalignment results in large performance degradation especially at millimetre-wave frequency. Furthermore, using separate substrates leads to a more complex construction and difficulty in MMIC implementation. Therefore, using loop slot proximity coupling to feed an elevated patch will overcome these drawbacks and have the advantage of broad bandwidth, less substrate effects and no alignment needed [14, 15].

A new concept for feeding an elevated patch antenna is presented here for first time. The new antenna design uses a loop slot instead of a probe at the end of CPW to feed the elevated patch. The main goal of this design is to enhance the antenna bandwidth and reduce the substrate effects with emphasis on antenna integration with other MMICs at G-band.

5.5.1 Antenna Design

The geometry of the elevated proximity coupled patch antenna is shown in Figure 5 - 16. The antenna structure combines the advantages of an elevated antenna with the advantages of proximity coupled antennas and simplifies the structure of the antenna to make the patch antenna easier to integrate with MMICs. The antenna patch is elevated above a CPW ground plane by $20 \times 20 \mu\text{m}^2$ gold posts with a height of $5.5\mu\text{m}$, and they are positioned within $25 \times 25 \mu\text{m}^2$ rectangular slots in the ground plane. The patch height has an important effect on the antenna

bandwidth and coupling level between the patch and feed. Increasing the patch height results in wider bandwidth and higher gain, but it gives less coupling with the feed line and increases the back radiation lobe level. Also, the length of the patch determines the resonant frequency of the antenna and the width of the patch affects the resonant radiation resistance of the antenna. For the proposed operating frequencies at G-band the dimensions of the patch have been optimized using HFSS simulation software, and they are $W \times L = 640\mu\text{m} \times 800\mu\text{m}$.

The patch is excited by proximity coupling using a loop slot formed in the ground plane and connected with the end of a 50Ω CPW feed line underneath the patch on GaAs substrate. Using the loop slot to feed the antenna gives symmetrical coupling between the feed and the radiating patch. Coupling the patch with the feed is usually determined by the location and the size of the loop slot. The dominant coupling mechanism between the patch and feed slot is a magnetic coupling, so the maximum of magnetic field for the TM_{10} mode is located in the centre of the rectangular patch antenna; therefore the best coupling will be obtained for a centered loop slot. Generally, the magnetic field in the slot loop is much stronger in the loop edges parallel to the radiating sides of the patch than in the two other edges of the loop. In other words, the patch excitation is mainly due to these excited edges. When the size of the centered square loop increases, the exciting edges are removed from the centre of the antenna. Therefore, the coupling mechanism is no longer optimum and the energy provided by the slot loop is not only coupled to the patch antenna, but also directly radiated to the back side. The worst coupling obviously occurs for loop edges close to the patch sides. In this case, the patch behaves more like a reflector (bad coupling) than a radiator (good coupling) toward the power radiated by the loop [107]. Therefore, the size and location of the loop slot can be adjusted below the patch to enhance the electromagnetic coupling and to obtain an appropriate input impedance.

The antenna ground plane is large enough ($W_s \times L_s = 1.5\text{mm} \times 1.5\text{mm}$) to reduce diffraction of the edges for reducing ripples in the main pattern and backward radiation, and it will completely shield the antenna from the underlying elements

and vice versa. The antenna ground plane is used both as a conducting plane for the CPW line and a reflector plane for the radiating patch. The antenna also features an air-bridge which is used to eliminate the unwanted even mode of the CPW feed line.

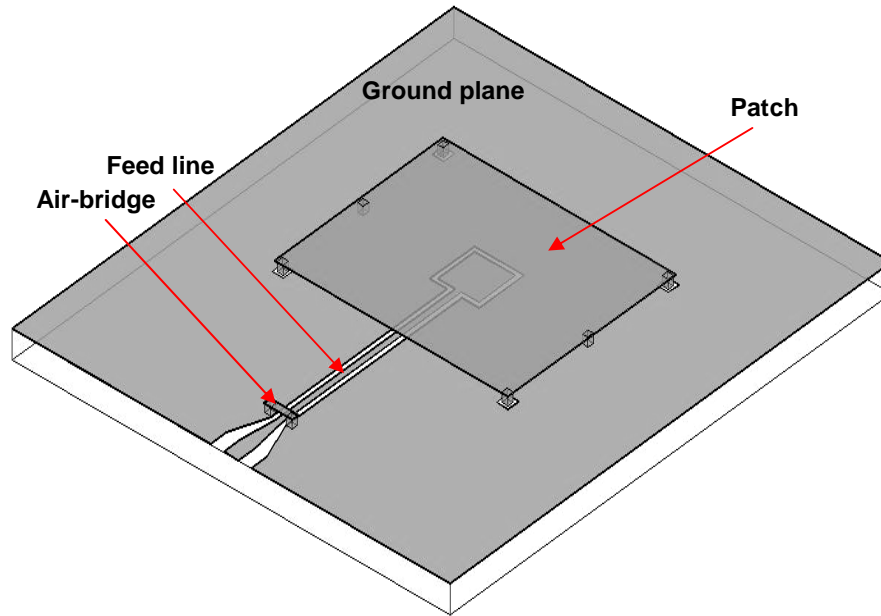


Figure 5 - 16 : Geometry of the proximity coupled elevated patch antenna.

The antenna was built on a GaAS substrate with a thickness of $630\mu\text{m}$ and a dielectric constant of 12.9 . Figure 5 - 17 shows the SEM image of the fabricated antenna. With this configuration, a broadband patch antenna can be realized, no separate substrates are needed, greater radiation pattern symmetry and a low-substrate dielectric constant can be achieved, since the antenna substrate is essentially air which is the lowest possible dielectric constant.

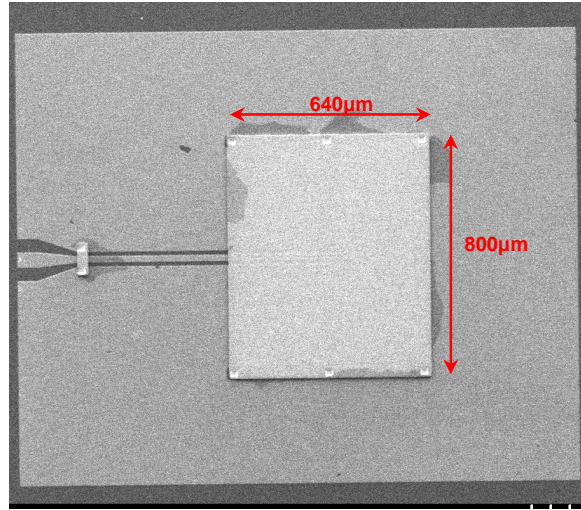


Figure 5 - 17: SEM photo of proximity coupled elevated patch antenna.

5.5.2 Analysis of Result

Figure 5 - 18 shows the measured and simulated return loss between 140GHz and 220GHz for the antenna.

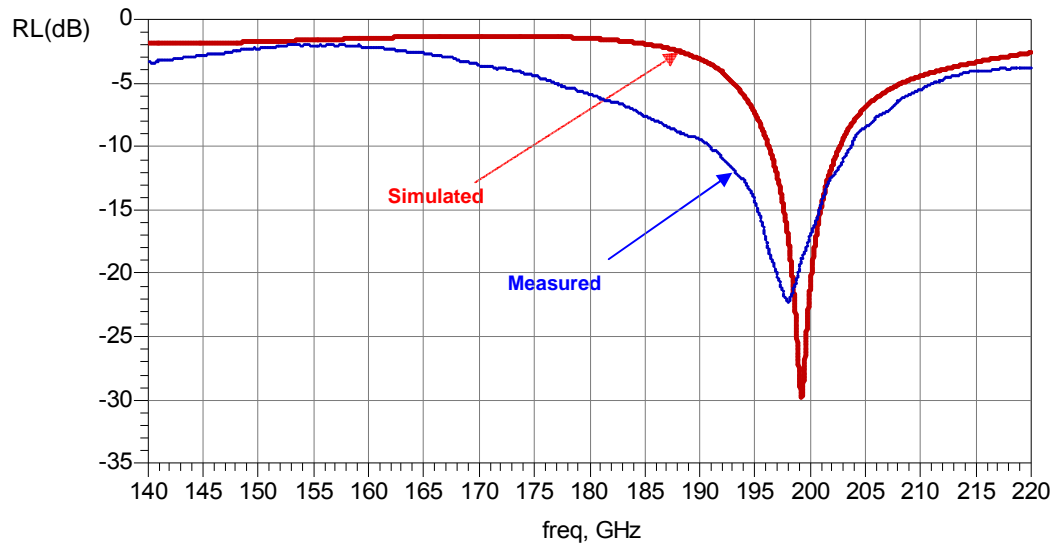


Figure 5 - 18 : Simulated and measured return loss of elevated proximity coupled patch antenna.

This Figure shows a resonant frequency at about 200GHz with a return loss of 22.3dB , the measured resonant frequency is shifted down by 1% , which can be attributed to factors, such as fabrication dimension variations and tolerances. A

very wide bandwidth of 13GHz has been achieved (for 10dB return loss) from 190.8GHz to 203.8GHz for the fabricated antenna, which is slightly higher than the simulated one.

Simulation demonstrates a symmetrical radiation pattern about the broadside direction across antenna bandwidth with gain of 2.97dB and 3dB beam width of 64° in the XZ -plane and 58° in the YZ -plane as shown in Figure 5 - 19. The gain diminishes slowly towards the edges of the antenna bandwidth, and falls sharply for frequencies out of the antenna bandwidth. It is postulated that this is due to significant surface wave generation outside the impedance bandwidth of the antenna as the energy is no longer strongly coupled to the patch element. Another effect of this surface wave generation is the high return loss out of antenna bandwidth (3 to 4dB). Also, the pattern is found to be stable across the whole bandwidth of the antenna with low back-lobe and excellent front-to-back ratio of 11.7dB (worst case) as shown in Figure 5 - 20, indicating a good coupling between the excitation loop slot and the patch. The cross polarization levels are better than -30dB in each plane.

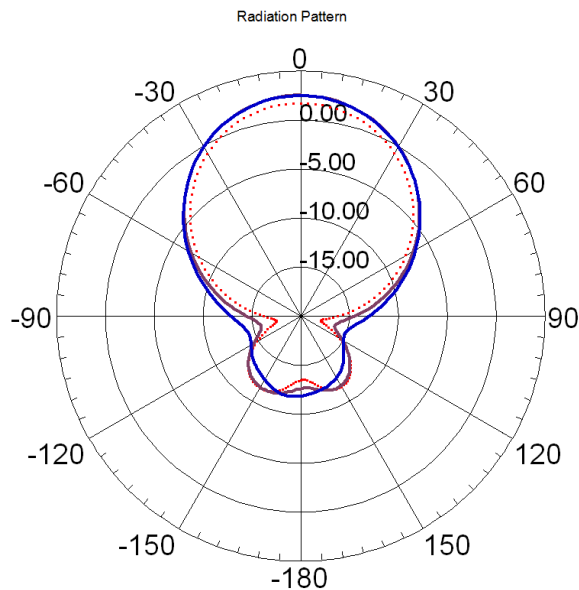


Figure 5 - 19: Radiation pattern at several frequencies across antenna bandwidth at xz -plane of elevated proximity coupled patch antenna.

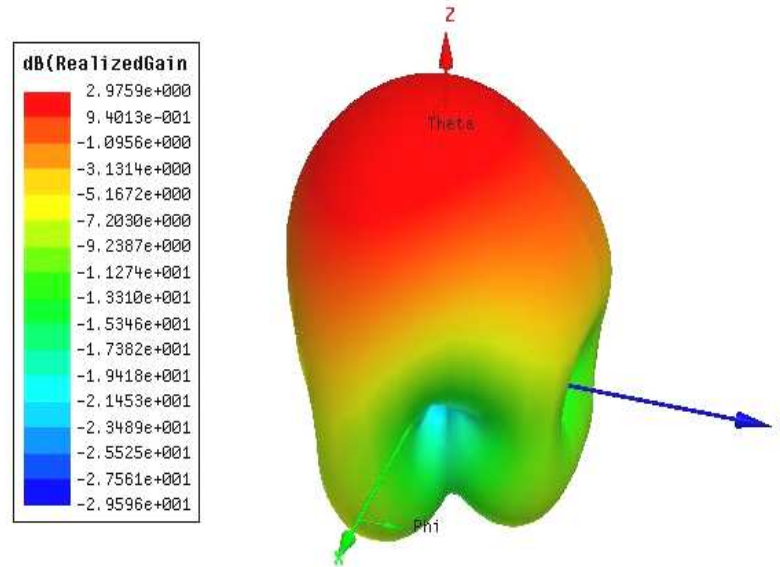


Figure 5 - 20 : Simulated 3D gain radiation pattern of elevated proximity coupled patch antenna.

The antenna configuration has several advantages over previously considered patch antennas. First, using a proximity coupled patch configuration yields greater bandwidths than direct contact fed patch antennas without significant degrading the front-to-back ratio of the antenna. Second, the slot loop can be used both as the antenna excitation and the isolation for dc bias when MEMS switches are used and it can be adjusted to get suitable input antenna impedance. The solution also reduces undesired substrate moding effects, and offers a viable route to higher levels of integration and functionality. Finally, the fabrication scheme offers a relatively simple method for monolithic integration with active MMIC transceiver circuitry.

5.6 EC-CPW Fed Elevated Patch Antenna

The elevated patch antenna has advantages of broad bandwidth, ease of integration with MMICs and reduced substrate effects. However, feed network loss has prevented them from being efficiently implemented in integrated form. For good antenna performance, a low loss feed is desirable since it will provide better radiation efficiency. Elevated conductor coplanar waveguide EC-CPW has the advantage of low loss compared with conventional CPW at G-band

frequencies as we discussed in section 5.2. This will increase the radiation efficiency, gain, and bandwidth of the antenna. Therefore, the aim of this design is to integrate patch antenna with RF circuit designs on high dielectric substrates without losing the advantages of low dielectric materials. This is achieved for the first time by elevating both the patch and centre conductor of the CPW feed line.

5.6.1 Antenna Design

Figure 5 - 21 shows a schematic of the antenna design structure. The elevated rectangular patch and EC-CPW feed are supported using a number of gold posts which offer a mechanically strong and rigid solution. In order to match the elevated patch, EC-CPW feed line is inset into the patch where the resonant resistance is equal to feed line impedance, and also EC-CPW feed is matched with feeding post by an elevated $\lambda/4$ transformer. The input impedance of the inset fed patch antenna mainly depends on the inset distance and to some extent on the inset width (spacing between feeding line and patch conductor) [77]. Therefore, the spacing between the patch conductor and feed line in this design is kept constant, $15\mu\text{m}$, and inset length is optimized using the simulation software HFSS and final length is $50\mu\text{m}$.

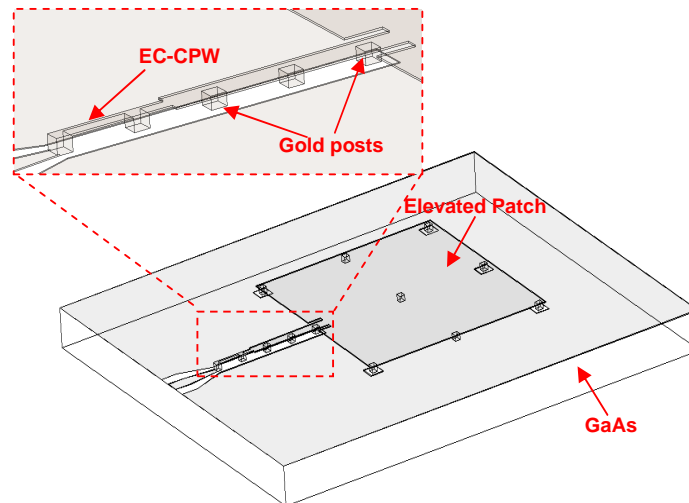


Figure 5 - 21 : EC-CPW fed elevated patch antenna structure.

For operation at G-band simulation suggested the geometry of the rectangular patch antenna to be $W \times L$ of $806\mu\text{m} \times 738\mu\text{m}$. Also, the antenna ground plane extends $W_s \times L_s$ of $1.5\text{ mm} \times 1.65\text{ mm}$ which is sufficiently large to reduce diffraction from the edges and reduces ripples in the main radiation pattern and minimizes backward radiation. The elevated central conductor CPW feed and patch were built on a $630\mu\text{m}$ thickness GaAs substrate with dielectric constant of 12.9. The height of the CPW central conductor and patch above the substrate can be varied as required for optimum antenna performance by changing the thickness of the photoresist used in the air bridge process. Figure 5 - 22 shows SEM photo of the fabricated antenna.

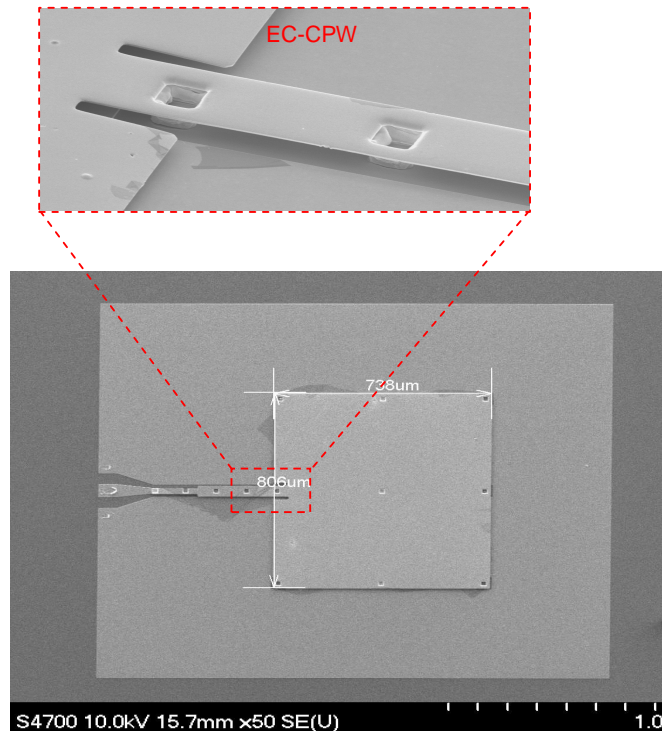


Figure 5 - 22 : SEM photo of fabricated EC-CPW fed elevated patch antenna.

The antenna topology effectively will create a low-substrate dielectric constant and undesired substrate effects can be eliminated, since the antenna substrate is essentially air and most of the electric field of EC-CPW is confined in the air region between the centre line and the ground, not in the substrate. This will help

increase the radiation efficiency, gain, and the radiation bandwidth. In addition, the type and thickness of the substrate can be varied without significantly impacting the antenna performance. This will allow the use of high dielectric substrates with different thicknesses.

5.6.2 Analysis of Results

Figure 5 - 23 shows the measured and the simulated input match (return loss) data of the antennas. A very good agreement between simulation and measurement was obtained, validating the electromagnetic simulation. The experimental results show a good match of -20dB at 172GHz and bandwidth of 7.9GHz from 169.2GHz to 177.1GHz (return loss $< -10\text{dB}$). However, there is quite high loss at higher frequency more, this probable because of discontinuity of electrical field due to the inset feed and $\lambda/4$ transformer.

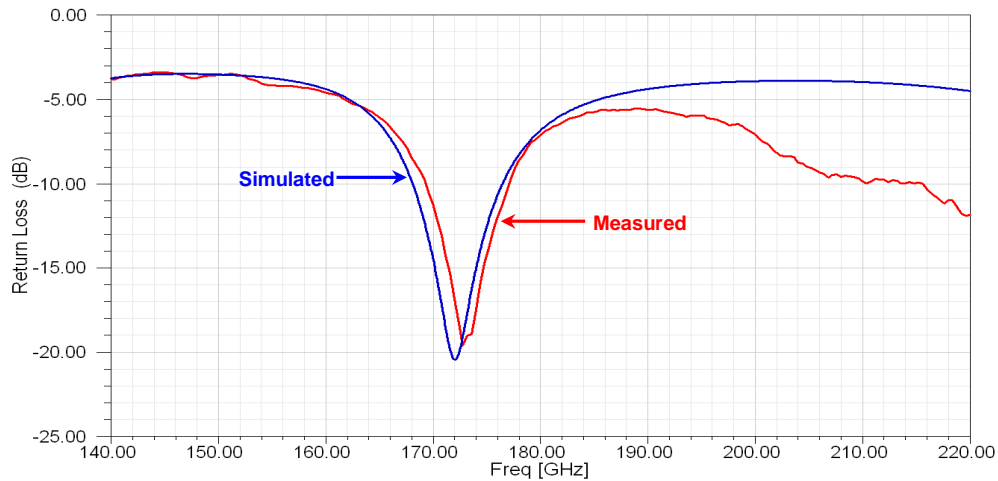


Figure 5 - 23 : Simulated and measured results of return loss for $5.5\mu\text{m}$ elevated antenna.

Simulation predicts a nearly constant broadside radiation pattern in both E and H plane cross the designed bandwidth with beam-width of 64° in the E-plane and 46° in the H-plane at resonant frequency as show in Figure 5 - 25. The simulated antenna gain in the vertical axis at resonant frequency is about 6.7dB with the front-to-back ratio (worst case) of about 7.8dB , showing high radiation efficiency

of the antenna structure. Figure 5 - 25 shows the simulated 3-D gain radiation pattern of the antenna.

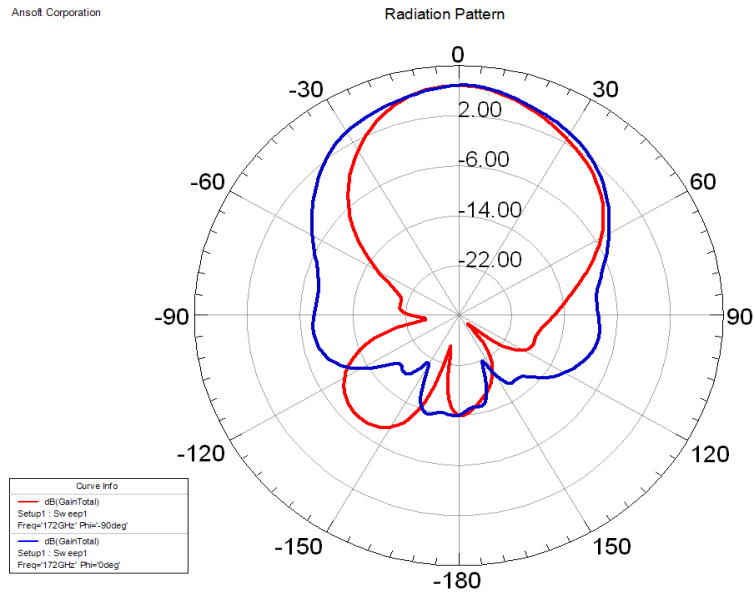


Figure 5 - 24: 2-D radiation pattern in E and H plane at resonant frequency (gain).

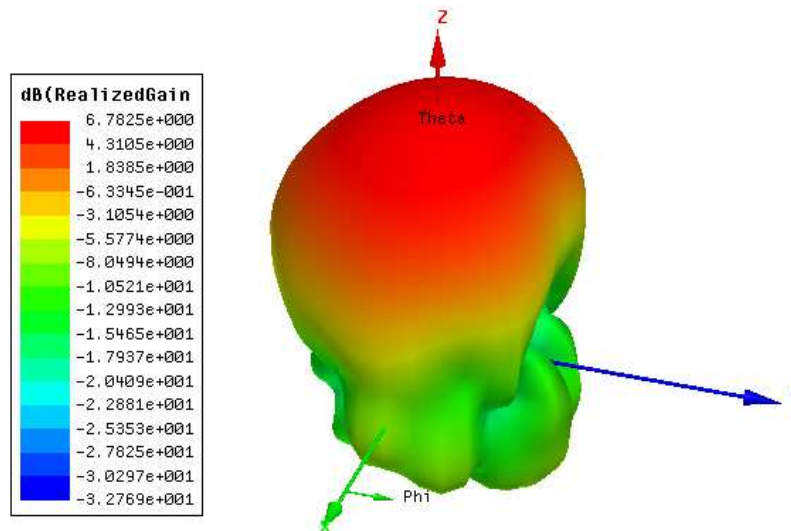


Figure 5 - 25 : 3-D simulated radiation pattern for the antenna gain.

From these results, it can be concluded that the proposed antenna configuration in this work offers significant improvements in performance compared with those

previously reported. The antenna scheme offers an easy method to integrate antenna with other MMICs, eliminate the undesired substrate effects, gives good matching with the feed line and maximizes antenna performance on high dielectric substrates. The structure also demonstrates broadband impedance matching and symmetry radiation pattern in G-band frequencies.

5.7 EMS Fed Elevated Overlapped Patch Antenna

The performance of patch antennas basically depends on the shape of the patch, feeding technique, and the dielectric constant of the substrate. Both patch shape and feed network can be improved. However, to integrate printed antennas with MMICs a high dielectric substrate must be used. Therefore, the basic idea of this antenna design is based on modifying the geometry of the antenna patch and exciting it by using elevated microstrip feed line EMS. Using EMS to feed an elevated antenna will reduce the substrate effects since the antenna and feed substrate is essentially air, and modifying the geometry of the patch will enhance the antenna bandwidth due to different resonant lengths of the patch.

In this design, an elevated microstrip line fed elevated overlapped patch antenna is proposed for the first time. This scheme is realized by elevating both the microstrip line and the patch using gold posts on high dielectric substrate.

5.7.1 Antenna Design

For a conventional rectangular elevated patch antenna of length L and width W , the resonance frequency for the dominant TM_{10} mode is only dependent on the length L of the patch. Therefore it is clear that the resonance frequency of the rectangular patch antenna is a function of its length L , so if the patch antenna has multiple lengths it will be a multi-resonance antenna i.e. for every different length there will be a different resonance frequency, hence the bandwidth of the patch antenna can be enhanced. This technique is utilized in the design of this antenna. Two small square patches are overlapped in the diagonal of the main rectangular patch and combining them in a single metallization to form a non-regular single

patch with different resonant lengths. The difference between resonant frequencies of the patch must be separated such that the overall integration of the resonant frequencies will give wider band width as shown in Figure 5 - 26.

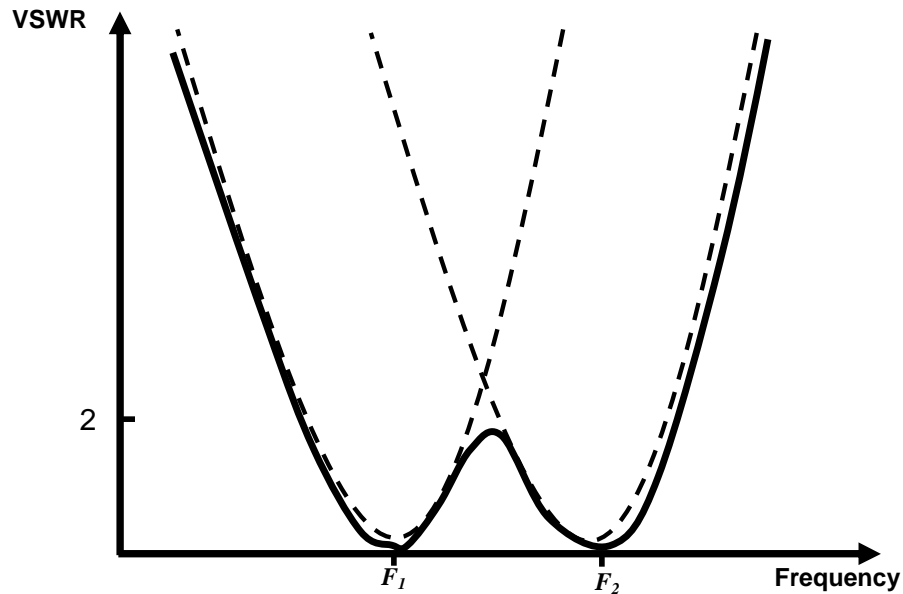


Figure 5 - 26 : VSWR plots of overlapped patch antenna has a narrow different between resonant frequencies.

The configuration of the proposed patch antenna is shown in Figure 5 - 27. The elevated overlapped patch is fed by an elevated microstrip line EMS via a $\lambda/4$ transformer to match to the 50Ω CPW port. By elevating both the patch and feed, the antenna topology effectively will create a low dielectric substrate since the antenna substrate is essentially air and all of the electric field of the elevated microstrip line is confined in the air not in the substrate. The overlapping patch and microstrip feed line are elevated above the antenna ground plane by $7.5\mu\text{m}$ gold posts height, which are positioned within rectangular slots in the ground plane to prevent shorting circuits. For the proposed operating frequencies at G-band the dimensions of the patch are shown in Figure 5 - 27. The antenna ground plane dimension is $1.5\text{mm} \times 1.5\text{mm}$ which is large enough to reduce diffraction of the edges for reducing ripples in the main pattern and backward radiation.

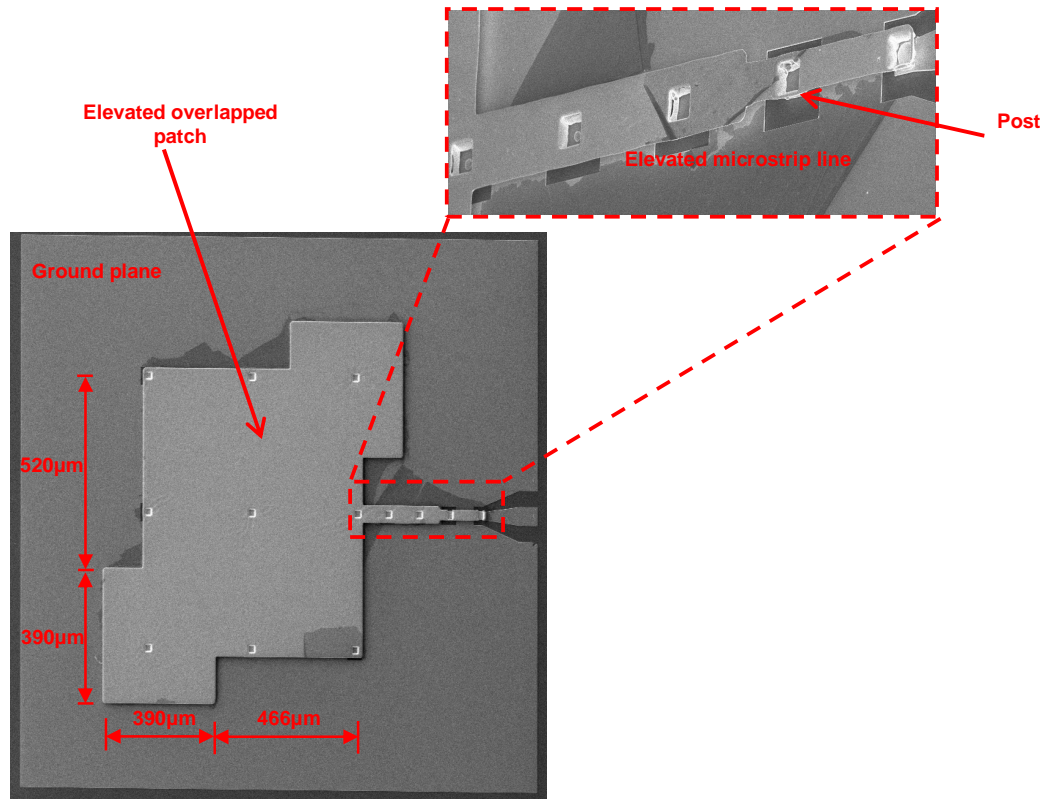


Figure 5 - 27 : Configuration of fabricated elevated overlapped patch antenna.

The antenna topology effectively creates a low-substrate dielectric constant and the patch geometry enhances antenna bandwidth without significantly enlarging the size since it employs multiple resonances.

5.7.2 Analysis of Results

Figure 5 - 28 shows the simulated and measured return loss between 140GHz and 220GHz for the elevated microstrip patch antenna. These results are in good agreement with the simulated results, validating the electromagnetic simulation. The measurement results show -39.7dB return loss (antenna match) at approximately 206GHz resonant frequency, and a very wide bandwidth of 12.5GHz has been achieved from 199GHz to 211.5GHz for a return loss than -10dB .

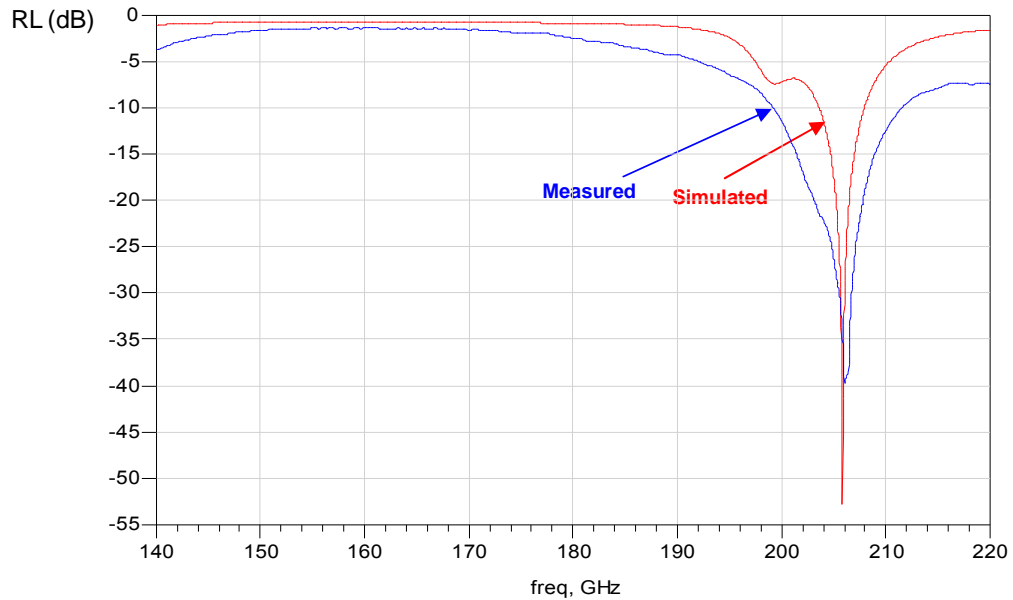


Figure 5 - 28 : Simulated and measured return losses and simulated 3-D radiation pattern.

Simulation predicts a nearly constant broadside radiation pattern ($3dB$ beamwidth of 60° in the XZ -plane and 48° in the YZ -plane) with low side lobes, and excellent front-to-back ratio of $11dB$ (worst case) as shown in Figure 5 - 29. The antenna has gain of $5.5dB$ at resonant frequency and it decreases at higher frequencies due to the fact that the radiating apertures of the two edge patches are relatively smaller compared to those of the main patch. Also, it is quite clear that the radiation pattern is not symmetrical because of the asymmetry of the patch. However, it is apparent that this antenna provides stable far field radiation characteristics in the entire operating band with relatively high gain. This indicates a high radiation efficiency structure across the designed bandwidth. The cross polarization is better than $-40dB$ at the centre frequency.

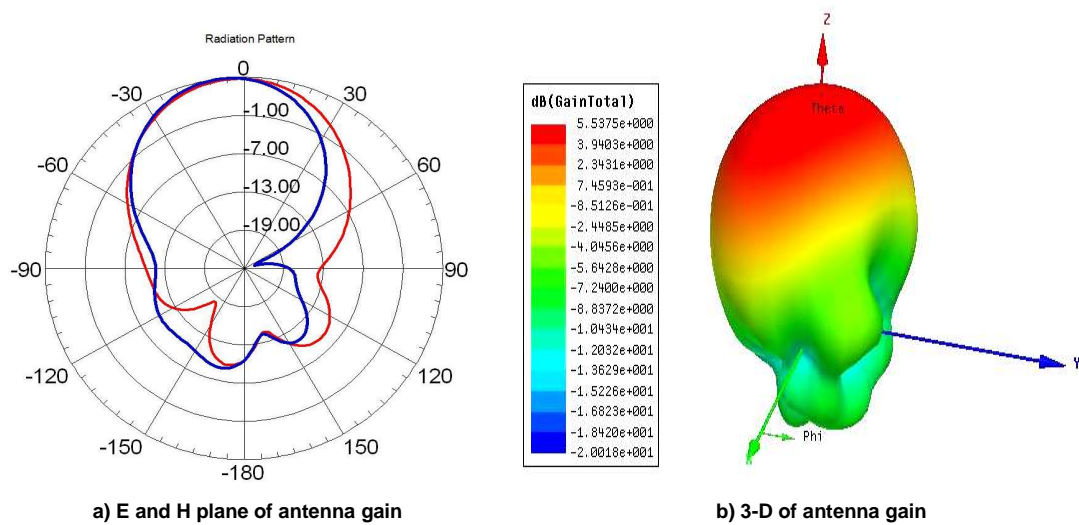


Figure 5 - 29 : Radiation pattern of elevated overlapped patch antenna.

This proposed configuration has several advantages over previous elevated patch antennas such as: surface wave loss associated with the feed network is eliminated, since all of the electric field of elevated microstrip line is confined in the air not in the substrate. Also, using an elevated overlapped patch configuration yields greater bandwidth without significantly enlarging the size since it employs multiple resonances on single patch, thus allowing integration of 3-D antennas with RF circuitry on a single chip.

5.8 EC-CPW Fed Three Level Proximity Coupled Antenna

The proximity coupled elevated patch antenna using a loop slot approach as we discussed in section 5.5 has advantages of broader bandwidth, reduced influence of substrate moding effects, no separate substrates needed, and this approach also gives symmetrical coupling between the feed and the radiating patch. However, feed network loss has prevented proximity coupled elevated patch antennas from being efficiently implemented in integrated form. Therefore, using elevated conductor coplanar waveguide (EC-CPW) to feed an elevated patch has the advantage of lower loss at high frequencies when compared with conventional transmission line structures.

A new concept for feeding a proximity coupled elevated patch antenna is presented in this design to maximise the antenna performance on high dielectric substrates. This design proposes a new antenna design that uses an elevated loop slot connected with EC-CPW to feed elevated patch antennas instead of using a loop slot which is printed directly on the substrate. This scheme has been realized by elevating both the centre conductor of a CPW line and loop slot at one level, and elevating the patch at a higher level. The main goal of this design is to enhance the antenna bandwidth and reduce the substrate effects with emphasis on antenna integration with other MMICs at G-band.

5.8.1 Antenna Design

An important principle for antenna design is to avoid the dielectric effects. The high dielectric substrate is an easier medium in which the propagation of surface waves can take place, hence our design is based on elevated antenna structures. However, elevated patch antennas on high dielectric substrate at G-band have been already demonstrated in previous sections in this chapter, exhibiting a significant improvement in the antenna performance. Specifically, in proximity coupled elevated patch antenna an impedance bandwidth of $13GHz$ was achieved. In this design, the substrate effect of the proximity coupled elevated patch antenna is further reduced by using EC-CPW connected with an elevated loop slot to feed the antenna. The antenna design takes advantage of the elevated patch antenna approach to eliminate surface waves, and advantage of the proximity coupled antenna approach to enhance the bandwidth without the need for separate substrates.

Figure 5 - 30 shows a schematic of the antenna structure. The patch is excited by proximity coupling using an elevated loop slot connected with an EC-CPW feed line underneath the patch on a gallium arsenide substrate. The elevated loop slot can be adjusted to an appropriate location below the patch to enhance the electromagnetic coupling and to obtain a suitable input impedance. Therefore, the antenna can be directly matched to various input impedances without using any

kinds of transformers. The EC-CPW feed line is connected with the CPW wave port by a gold post, and is designed to be 50Ω in order to match to the reference impedance of the measurement system.

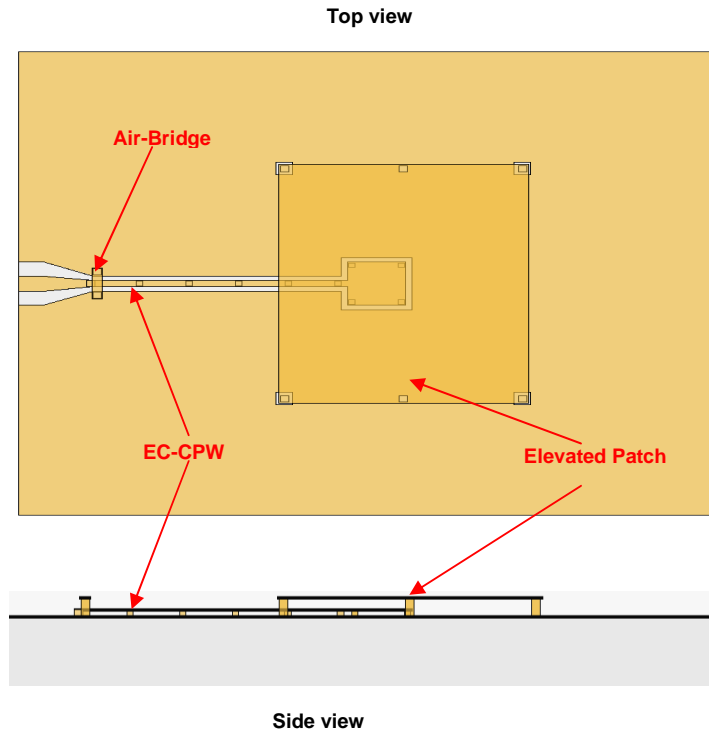


Figure 5 - 30 : EC-CPW fed elevated proximity patch antenna.

The main advantage of this feed technique is that it provides very high bandwidth, gives symmetrical coupling between the feed and the radiating patch, and reduces the substrate effects. The elevated loop slot and EC-CPW feed are supported using a number of $5.5\mu\text{m}$ gold posts. On the other hand, the rectangular patch is elevated above the EC-CPW and the loop slot by $13\mu\text{m}$ gold posts, which offer a strong and rigid mechanical performance. The EC-CPW ground plane on the substrate will completely shield the antenna from the underlying elements and vice versa.

The antenna was designed and simulated using the Ansoft HFSS simulator. A waveport at the antenna input terminal was used for the simulation with meshing

at $\lambda/4$ to obtain higher simulation resolution. For operation at G-band for radiometer applications at $200GHz$ simulation suggested the geometry of the rectangular patch antenna to be $W \times L$ of $806\mu m \times 738\mu m$, with a ground plane extent, $W_s \times L_s$, of $1.5mm \times 1.65mm$, which is large enough to reduce diffraction at the edges for reducing ripples in the main pattern and backward radiation. The antenna was fabricated on a $630\mu m$ thickness GaAs substrate with a dielectric constant of 12.9 . Figure 5 - 31 shows an SEM image of the completed antenna. The fabrication scheme offers a relatively simple method for monolithic integration with active MMIC transceiver circuitry.

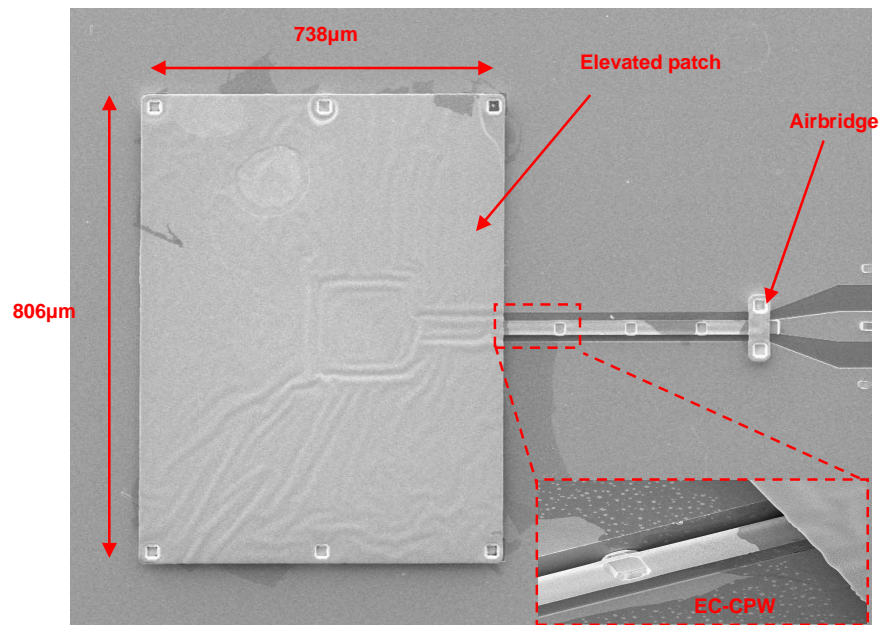


Figure 5 - 31: SEM photo of the fabricated EC-CPW fed proximity coupled antenna.

5.8.2 Analysis of Results

Figure 5 - 32 shows the measured and the simulated return loss of the antenna. Good agreement between simulation and measurement was obtained, validating the electromagnetic simulation. The measurement results show an excellent match of $-32dB$ at $196GHz$ and bandwidth of $15GHz$ from $188GHz$ to $203GHz$ (return loss $< -10dB$). This bandwidth is higher than the simulated value which has

5.5GHz bandwidth. As a comparison, the patch antenna which is reported in section 5.5 gives a narrower bandwidth of 13GHz than measurement results indicate.

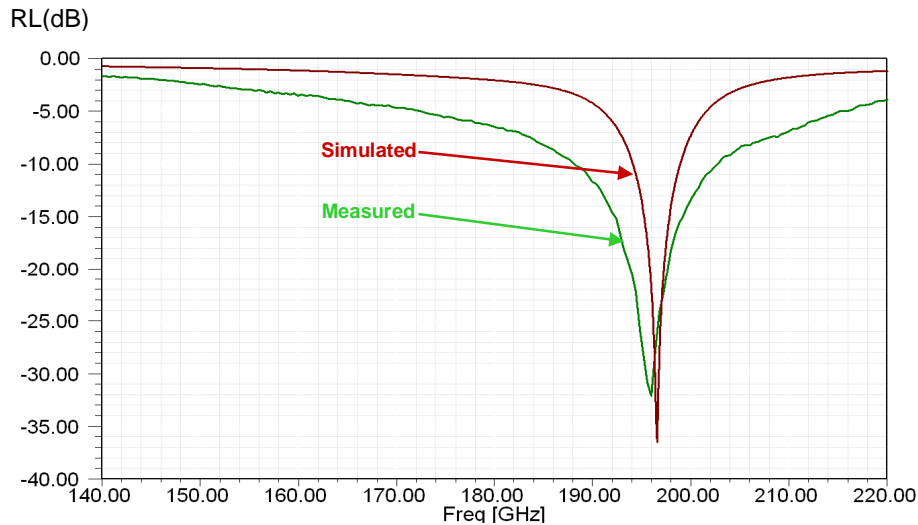


Figure 5 - 32 : Simulated and measured results of antenna return loss.

The proposed antenna demonstrates a significantly improved radiation characteristics compared with the two-level antenna which uses a feed network directly printed on substrate. A comparison is shown in Table 5 - 1.

Table 5 - 1 : Comparison of three-level and two-level antenna performances

	Bandwidth	Matching	Gain	XZ-plane beam width	YZ-plane beam width	Front-to-back ratio
Three-level antenna	15GHz	32dB	7.18dB	68°	56°	32.2dB
Two-level antenna	13GHz	22.3dB	2.97dB	64°	58°	11.7dB

Simulation results of the designed antenna predict a nearly constant broadside radiation pattern with high gain of 7.18dB and an excellent front-to-back ratio of 32.2dB indicating good coupling between the feed and the patch as shown in Figure 5 - 33. This indicates a high radiation efficiency structure across the

designed bandwidth. It can be clearly observed from Table 5 - 1 that the proposed antenna configuration in this paper offers significant improvements in the radiation performance compared with the previously reported proximity coupled antenna. Using EC-CPW connected with an elevated loop slot to feed an elevated patch has the advantage of broad bandwidth, low substrate loss and elimination of the excitation of surface waves since most of the electric field of the feed is confined in the air rather than the substrate - thus avoiding undesired coupling between the feed and the substrate. This increases the radiation efficiency, gain, and the radiation bandwidth. The antenna demonstrates a desirable broad bandwidth and low-loss performance suitable for many wireless short range communication applications.

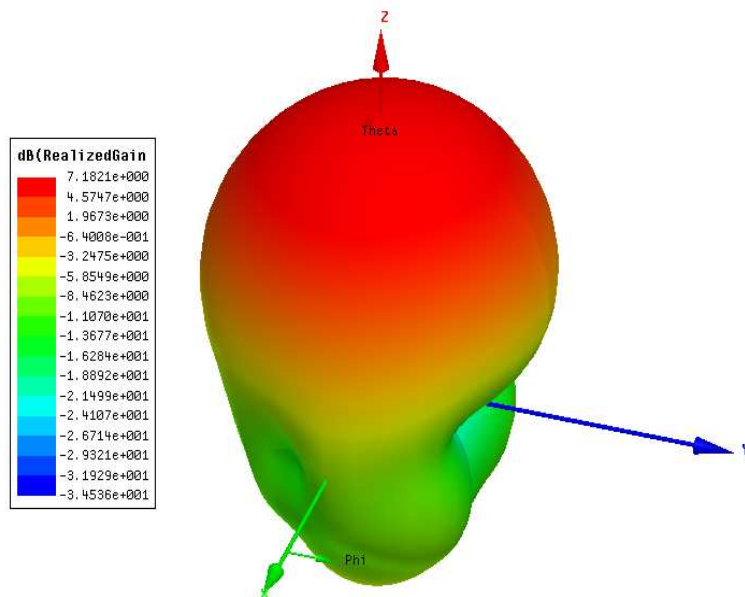


Figure 5 - 33 : 3-D simulated radiation pattern at the centre frequency (Gain dB).

5.9 Conclusion

In conclusion, it can be seen that the proposed antenna configurations, which are designed in this chapter, offer significant improvements in performance compared with previously reported work. Different new feeding mechanisms of elevated micromachined antennas were presented for first time offer more degrees of freedom for antenna design, and they provide low radiation loss, less dispersion and less dependence of the characteristic impedance on the substrate height and permittivity. In addition, new alternative topologies of G-band micromachined antennas on high dielectric substrate MMICs have been presented. Experimental and simulation results are provided to demonstrate the effectiveness of the antenna designs. The proposed antenna configurations have several advantages over previously reported micromachined antennas on high dielectric substrate such as: (a) antennas schemes effectively create a low dielectric constant substrate and maximize the antenna performance on high dielectric substrates; (b) the corresponding dimension for antennas working at G-band is on millimetre scale, thus allowing integration of 3-D antennas with RF circuitry on a single chip; (c) for traditional printed antennas integrated with other components, once the substrate specifications are chosen for the whole module, the thickness is a universal variable for each component on this substrate and it cannot be tailored freely and thus optimized for antenna design. However, for the elevated antennas presented in this work, the height of the patch can be changed, regardless of the substrate that is used. This can be used to further enhance the antenna performance when we cannot change the substrate thickness for the sake of the rest of the module circuits. Thus, elevated micromachined antennas can meet different application requirements and be utilized as a substrate-independent solution.

6. Reconfigurable Micromachined Antenna

6.1 Introduction

Reconfigurable antennas have become more attractive as the demand for multiband antennas has increased. They provide greater levels of functionality to a system by eliminating the need for complicated wideband antenna solutions. Common antenna designs not involving re-configurability impose restrictions. Reconfiguring antennas can enhance their performance by providing the ability to adapt to new operating scenarios. MEMS switches have been introduced as a prime candidate to replace the conventional solid state switches in reconfigurable antennas. The first part of this chapter covers the rapid development of MEMS switch technology and their limitations and advantages in reconfigurable printed antennas at millimetre-wave regimes and focuses on cantilever beam metal-contact MEMS switches. This is followed by proposing a new design of a low-actuation voltage cantilever beam MEMS switches for high-frequency applications, which can overcome the limitations associated with cantilever MEMS switches. The second part of this chapter discusses the concept of reconfigurable antennas and details the emerging technologies that make reconfigurable antennas possible with a primary focus on MEMS reconfigurable frequency antennas. Also, in order to incorporate the proposed new MEMS switch with the 3D antenna technology, a novel reconfigurable elevated patch antenna is described and its performance discussed. The antenna design demonstrates the feasibility of reconfigurable printed antennas on high dielectric substrates at G-band.

6.2 Integrated MEMS Switch with Reconfigurable Antennas

The development of wireless communications requires miniaturization, multi-function and multi-systems integration. For various communication systems, the operation frequencies can vary. Different frequencies correspond to various structures or dimensions associated with the antenna. As the key device of the wireless communication system, the antenna also needs to realize the multi-function capability. A reconfigurable antenna is such a kind of multi-function antenna, which can change the frequency, radiation pattern or polarization in real-time without changing the whole dimension and structure of the antenna. The goal of a reconfigurable antenna is to reduce the complexity of an antenna system operating over a wide frequency band, and to reduce the need for multiple antennas to perform a specific task - providing a relatively large bandwidth and achieving a dynamic configuration. Compared with broad band antennas, reconfigurable antennas offer the advantages of compact size, similar radiation pattern for all designed frequency bands, efficient use of electromagnetic spectrum and frequency selectivity useful for reducing the adverse effects of co-site interference and jamming [108-111].

A key enabling technology for the successful development of reconfigurable multi-band antennas is the development of switches with low loss, high isolation and low bias power requirements. Switches based on PIN diodes and FET transistors can be successfully used at microwave region, but they exhibit inherently high insertion loss at millimetre-wave regimes that reduce the radiating efficiency of the antenna to a point where it might be unacceptable for many applications [29, 112]. Furthermore, the use of solid state switches introduce a limitation on the power that can be handled by the antenna and the possibility of unwanted nonlinear effects both on transmission and reception. It would be highly desirable to have a switch for reconfigurable antennas that alleviates these potential problems. It appears that MEMS switches can offer promising characteristics in this regard. Integration of MEMS technology with antenna technology makes the antennas smaller, 'smarter' and cheaper, thereby meeting the demands of rapid development of communication systems [6, 113]. The

tuneable characteristics of MEMS switches enable their integration with antennas and make very efficient use of limited area by taking advantage of combined multiple functions in one single antenna. This results in significant reduction in the total area with possible enhanced functionality and performance. Also, the monolithic fabrication of these components with antennas can reduce parasitic effects, losses and costs [26, 27, 114].

6.3 MEMS Switches

A MEMS switch is a switching device that is fabricated using the micromachining technology, where the switching between the on- and off-states is achieved via the mechanical movement of a freely movable structure [115-117]. The forces required for the mechanical movement can be obtained using various actuation mechanisms include electrostatic, magnetic, thermal and piezoelectric. (a) The Electrostatic method relies on the basic columbic force of attraction between two oppositely charged plates. (b) Electromagnetic methods of actuation rely on aligning a magnetic material in a magnetic field. By changing the direction of the alignment the switch can be turned *On* or *Off* [118]. (c) Thermal actuation involves using two materials with different thermal expansion coefficients. When the materials are heated the beam bends away from the material with the higher thermal expansion coefficient. (d) Piezoelectric actuation is typically based on a bimorph cantilever or membrane, where a differential contraction due to the piezoelectric effect causes the structure to bend.

Each method has its own set of problems; high power requirements and slow switching speed for thermal; high voltages for electrostatic which may lead to difficulty of integration; high complexity, cost, and power requirements for magnetic actuation; and integrating piezoelectric materials for piezoelectric actuation is very problematic, because films are difficult to pattern and the processing involves high crystallization temperatures [29, 112]. Among these actuation mechanisms, MEMS switches that operate electrostatically are most commonly used to tune printed antennas, as it is the simplest of all, the most

compact solution, has low power consumption and does not involve any special processing steps which are not supported by normal MMICs processes [6, 8, 115, 116, 119]. Generally speaking, MEMS switches are based on designs that employ electrostatic actuation.

6.3.1 MEMS Switches types

The MEMS switches can be classified into three classes based on mechanical structure, contact mechanisms or circuit configuration [29, 120] - each type has certain advantages in performance or manufacturability. Figure 6 - 1 shows MEMS switches types.

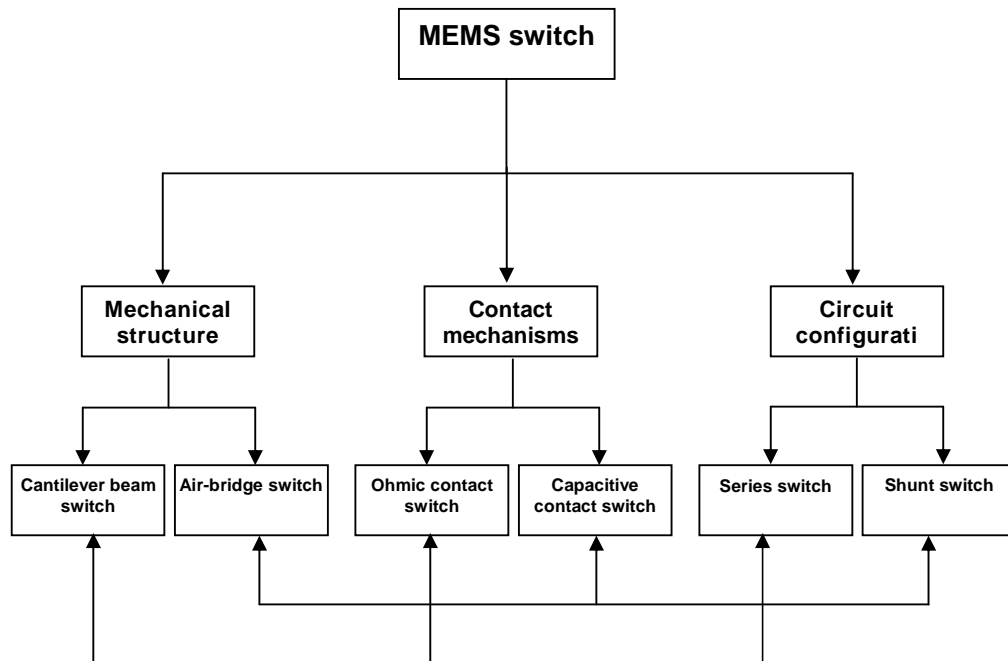


Figure 6 - 1 : MEMS switches types

In terms of the mechanical structure, MEMS switches can be divided into those that have architectures based on suspension air-bridges or cantilever beams [29, 114]. With the air-bridge structure, there are two supporting posts at both ends of a membrane suspended over an electrode, and the membrane contacts the electrode at its centre. The membrane of the cantilever structure has one fixed end at the supporting post, and the other free end has electrodes for position biasing.

MEMS switches are also categorized by the contact mechanisms: capacitive (metal-insulator-metal) contact [121, 122] and resistive (metal-to-metal) contact [123-125]. Capacitive switches use a thin layer of dielectric material to separate two conducting electrodes when actuated. The dielectric layer prevents direct metal-to-metal contact. Therefore, stiction of contacts is less of a concern. However, the thin layer of dielectric material will only conduct signals with reasonable insertion loss when the coupling between conductor electrodes is above a certain frequency. Moreover, the operation frequency of capacitive switches is limited by the ratio between the on and off capacitance. Metal-to-metal switches utilize physical contact of metal with low contact resistance to achieve low insertion loss when actuated. Therefore, the metal-to-metal MEMS switches can be operated from DC to RF frequency with isolation defined by the coupling capacitance of the electrodes when the switch is in up-state. The broad frequency range of MEMS metal contacting switches is a major advantage of this kind of switches.

Switches can also be designed to have either series or shunt configurations within the RF circuit. Although both metal contacting and capacitive coupling switches can be used as either as a serial or a shunt switch, metal contacting switches are often used as serial switches, while capacitive coupling switches are used for shunt switches. The advantage and disadvantage comparison between the two ways of using the switches is primarily within the RF circuit design, rather than MEMS switch components. The final design selection is heavily guided by specific applications [8, 29, 116].

6.3.2 Advantages of the MEMS Switches Over Current Technologies

MEMS switches offer significant performance enhancement over current electromechanical and solid state switch technologies. The significant performance improvements possible with these MEMS devices have important implications in antenna designs at microwave and millimetre-wave frequencies

[29, 112, 115, 116, 126-128]. The basic advantages that MEMS switches offer can be summarized as follows:

- **Low power consumption:** Many MEMS switches are actuated using electrostatic mechanisms which consume very small amounts of energy ($10\text{-}100\text{nJ}$ per switching cycle).
- **Low insertion loss:** Insertion loss is a measure of how much loss is being introduced to the system due to the switch. MEMS technology offers switches with very low loss. The reported loss of MEMS switches are 0.1dB up to millimetre-wave frequencies.
- **High isolation:** Isolation determines how well the output is isolated from the input. Higher isolation translates to less coupling between the output and input ports in the off state. As MEMS switches are fabricated with air gaps, they have very low off-state capacitance resulting in excellent isolation well into the millimetre-wave region.
- **Linearity and low inter-modulation products:** The quality of the signal passed through the switch is measured by its linearity. Switches which pass signals without distortion or the introduction of harmonics are highly linear. Since the MEMS switches contain no semiconductor or any other electrically nonlinear components they are extremely linear devices and result in very low inter-modulation products in switching and tuning applications.
- **Wide Bandwidth:** Similar to conventional mechanical switches, the bandwidth of MEMS switches is quite large. Unlike solid state switches which rely on a semiconductor junction, the conduction path is based on a metal to metal contact. The upper limit on frequency of operation is mainly restricted by device isolation in the *off* state.

6.3.3 Limitations of the MEMS Switches

Even though MEMS switches have very good performance metrics, the current implementations still suffer from a number of important limitations which restrict their application in reconfigurable antennas at millimetre-wave regimes. It is necessary to identify the characteristics of MEMS switches that could potentially cause problems for reconfigurable antennas [29, 114, 115, 126, 128-131]. The following problems have not been solved yet:

- **High pull-down voltage:** Most electrostatic MEMS switches have high pull-down (actuation) voltage for reliable operation. This can present a problem for portable devices where high voltage signals may not be readily available and up-converters would be needed to provide adequate switching potential. Low voltage switches are being developed to help mitigate this problem.
- **Slow switching speed:** The switching speed of most MEMS switches is relatively low compared to semiconductor devices. This is because of the low resonant frequencies of its mechanical structure, and also the improvement of switching speed of a MEMS switch affects adversely the switching voltage. Faster switching can be obtained with increased stiffness, but it will inevitably increase the pull-down voltage.
- **Low reliability:** The reliability of MEMS switches still are not sufficient for current wireless systems some of which require more than 100 billion cycles.
- **Low power handling:** One of the biggest limitations that MEMS switches currently face is power handling capability. Most MEMS switches can only handle medium power levels. MEMS switches that handle high power with high reliability still do not exist today.
- **Packaging considerations:** MEMS switches are inherently moving devices and thus are easily affected by environmental contaminants and physical contact. Special attention must be given to the protective packaging used to

shield the components and hermetic sealing is an essential part of the package assembly. Packaging costs are currently high, and the packaging technique itself may adversely affect the reliability of the MEMS switch.

- **Stiction:** one of the most common failures both in fabrication and operation of MEMS switch is stiction. It refers to any kind of adhesion that can occur between switch contacts. Although it is particularly problematic in metal-to-metal switches, the addition of a thin dielectric layer between the metals contacts may help mitigate this problem.

6.4 Cantilever Beam Metal-Contact MEMS Switch

Cantilever beam metal-contact switches have been selected for this work for integration with an elevated patch antenna since they utilise direct physical contact between metals with a low contact resistance to achieve low insertion losses when actuated. It can therefore be operated at G-band frequencies with low loss and an isolation defined by the coupling capacitance of the electrodes when the switch is open. Also the cantilever switch offers the important advantage of reduction in the pull-down voltage, when compared to that required by the air-bridge switch. This section will cover the basics principle of such switches.

6.4.1 Working Principle

The basic operation of a cantilever beam switch is very simple; it relies on the basic columbic force of attraction between two oppositely charged electrodes (cantilever contact pad and bottom metal contact). The cantilever beam of the switch is suspended over a bottom metal contact in such a way that the two contacts form a capacitor [112]. When a bias voltage is applied across the contacts, charge distributes in such a way that an electrostatic force occurs between them. Independent of the voltage polarity, the voltage forces the top contact down toward the bottom one, creating an opposing mechanical restoring force as the structure is bent. If the voltage is increased, the cantilever beam gets

close to the bottom contact, the increasing charge on the contacts increases the force and the equilibrium is held by an increase in the restoring force at some point between the plates. However, after the voltage value exceeds some value (threshold value) the restoring force can not afford the electrostatic force. At this point, the system goes to an unstable state, and the beam collapses upon the bottom electrode. If the magnitude of voltage is then reduced, the cantilever releases back up due to the intrinsic stress, but typically at a much lower voltage than the pull-down voltage [29]. The basic structures and operation of switch is shown in Figure 6 - 2.

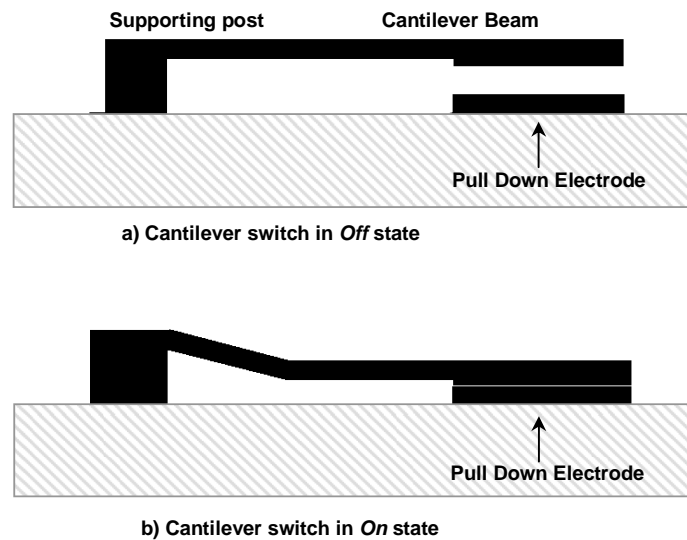


Figure 6 - 2 : Basic operation of MEMS cantilever switch

6.4.2 Electromechanical Mode

The essential problem of MEMS switches is the coupling of the mechanics and the electrostatics, which governs the behaviour of the MEMS switches. The two most important features of a MEMS switch are the pull-down voltage and the deflection. Both of these quantities can be calculated by treating the MEMS switch as a mechanical spring with an equivalent spring constant k . The equivalent spring constant depends on the geometrical dimensions of the cantilever beam and on the Young's modulus of the material used to fabricate the switch. The actuation

behaviour of the switch can be understood from the equivalent parallel plate capacitor shown in the Figure 6 - 3. The bottom plate is fixed in space and the cantilever (top plate) is held by a mechanical spring. The movement of the cantilever can be analyzed as a flat problem [113, 115, 132-134].

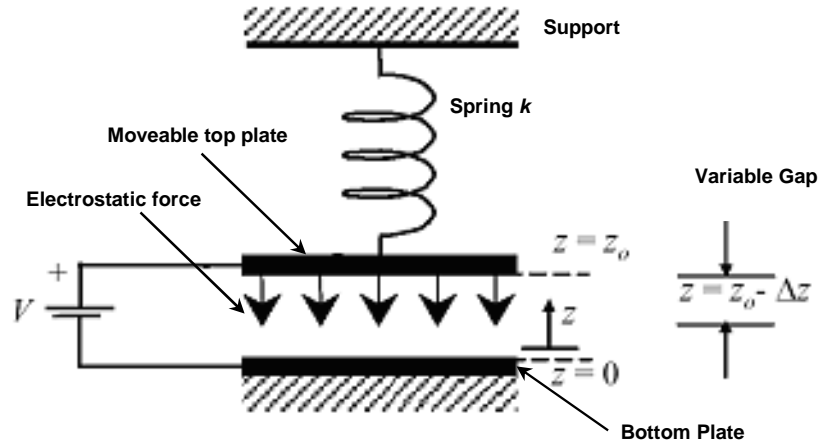


Figure 6 - 3 : MEMS switch mechanical modelling

When a bias voltage V is applied, the cantilever moves toward the bottom plate from an initial gap height z_0 to a new gap height z , where $z = z_0 - \Delta z$. The electrostatic energy stored in the capacitor is given by:

$$U_E = \frac{1}{2} \frac{\epsilon_0 A}{z} V^2 \quad (6.1)$$

where z is the gap height between the plates, A is the area of actuating plate, and ϵ_0 is permittivity of free space.

The movement of the cantilever will cause the electrostatic force which is equal to the rate of changing stored electrostatic energy with displacement (dU_E/dz) at a constant voltage between the plates; the electrostatic force is given by:

$$F_E = -\frac{1}{2} \frac{\epsilon_0 A V^2}{z^2} \quad (6.2)$$

The negative sign in implies that the electrostatic force is in the downward direction. Electrostatic actuation results in very low forces, but this is enough for MEMS switch actuation. The reason is that, as the switch is pulled down to the bottom electrode, the gap is reduced, and the pull down force on the switch increases. Considering the fact that the electrostatic actuation force increases at a rate of $1/z^2$ as the gap closes, it takes much less time to pull down the switch than it does to release back up the upper plate. In addition to the electrostatic force, gravity also plays a role in pulling down the switch cantilever beam. Calculation of this force is simple and straightforward, $F_g = mg_g$, where m is the cantilever mass, g_g is the gravity, which has a typical value of $g_g = 9.8$ (N / kg). Although F_g is usually small in magnitude, it may be in the same order of electrostatic force for some architectures. Therefore, it shouldn't be ignored in calculations.

There is also a pull up force due to the spring constant of the switch. The force pushing up from the spring using Hooke's Law is

$$F_M = k\Delta z = k(z_o - z) \quad (6.3)$$

The cantilever will be stable as long as the mechanical force balances the electrostatic force by downward movement. Equating the mechanical restoring force and the electrostatic force in the stable state and solving for V gives

$$V = z \sqrt{\frac{2k(z_o - z)}{\epsilon_o A}} \quad (6.4)$$

The above equation gives the voltage V required to pull the cantilever towards the bottom plate by a distance of Δz from an initial gap height z_o . This equation yields a parabolic like variation of normalized gap height (z/z_o) with V as shown in Figure 6.4. When the gap reduces to certain point, the cantilever beam becomes unstable and then a complete collapse of the switch to the down-state position. This behavior

is known as pull-down and the voltage at this point is termed as the Pull-down Voltage V_p .

The pull-down position can be found by taking the derivative of Equation 6.4 with respect to cantilever height and setting that to zero as

$$\frac{dV}{dz} = \left(\sqrt{\frac{2k}{\epsilon_o A}} \right) \sqrt{z_o - z} - \left(\sqrt{\frac{2k}{\epsilon_o A}} \right) \frac{1}{2} \frac{z}{\sqrt{z_o - z}} = 0 \quad (6.5)$$

The height at which the pull-down occurs is found to be exactly two-third the zero bias cantilever beam height $z = \frac{2}{3} z_o$. Substituting this value back into Equation 6.4, the pull-down voltage is found to be:

$$V_p = \sqrt{\frac{8 k z_o^3}{27 A \epsilon_o}} \quad (6.6)$$

Pull-down voltage is an important factor in the design of the switch as this alone decides the compatibility of the switch with other circuitry on the die. If the switch voltage is reduced, the cantilever releases back up, but typically at a lower voltage than the pull-down voltage. Therefore, the voltage required for holding the cantilever in the down position is lower than the pull-down voltage. The voltage at which the cantilever is completely released from the bottom contact is known as Release voltage V_R [112, 135]. This creates a hysteresis characteristic (typical of all MEMS switches) as shown in Figure 6 - 4.

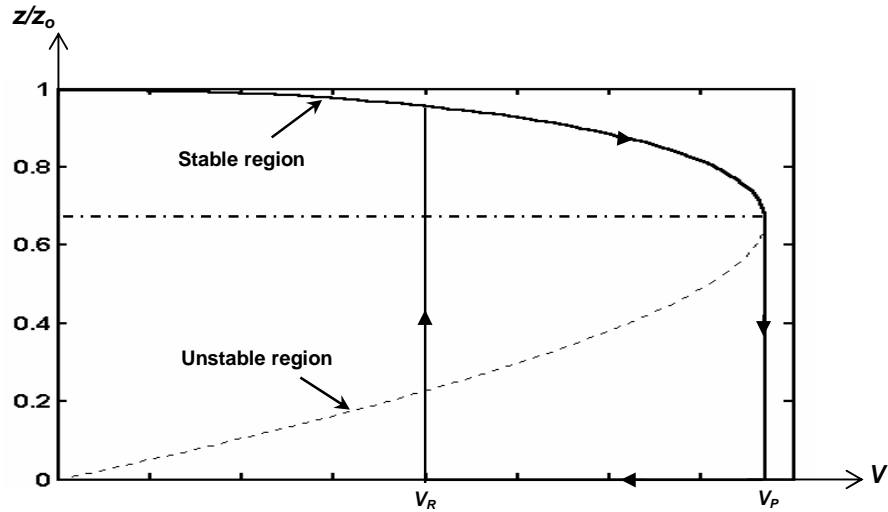


Figure 6 - 4 : Variation of normalized gap height (z/z_0) with applied voltage (V)

6.4.3 Electrical Model

The simplest electrical model of the cantilever beam MEMS is a series capacitance, C , in the up-state position and a small resistance, R_s , in the down-state position, since the actuation region exhibits a capacitance, and the metal beam exhibits a resistance as shown in Figure 6 - 5. The down-state resistance is effectively representing the on-state insertion loss, whereas up-state capacitance is effectively representing the off-state isolation [29, 114, 115, 117, 133, 135].

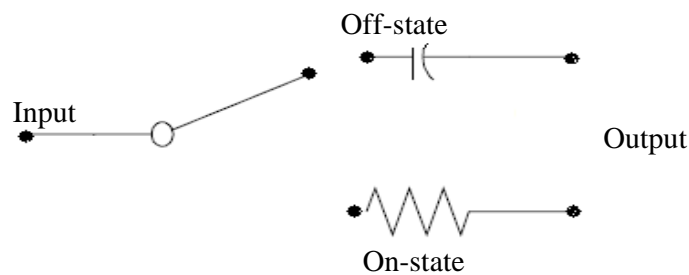


Figure 6 - 5 : Equivalent circuit model for cantilever switch.

The isolation of the switch in the up-state position can be calculate by

$$|S_{21}|^2 = 4\omega^2 C^2 z_0^2 \quad (6.8)$$

where z_0 is the transmission-line impedance. Also, the insertion loss in the on-state can be calculate by

$$|S_{21}|^2 = 1 - \frac{R_s}{z_0} \quad (6.9)$$

The R_s , and C value can be calculated within an order of magnitude by using fundamental equations[39].

$$R_s = \frac{\rho l}{tw} \quad (6.10)$$

Where ρ is the resistivity of the cantilever metal, l is the length of the cantilever, t is the thickness of the cantilever and w is the width of the cantilever. Also, the up-state capacitance of the MEMS switch can be calculated by

$$C = \frac{\epsilon_o A}{z_o} \quad (6.11)$$

where A is the effective contact area of the electrode, and z_o is the gap height between the contacts.

6.5 Design Challenging of Cantilever Beam MEMS Switch

Even though cantilever beam MEMS switches show very good performance, current implementations still suffer from a high pull-down voltage and the stiction problem - restricting their integration with printed antennas. Therefore, the design of a cantilever beam MEMS switch with low pull-down voltage and compatibility with reconfigurable printed antennas at G-band frequencies and which can overcome the stiction problem is still a very challenging task. This section addresses these design challenges of electrostatically actuated cantilever beam metal-contact MEMS switches.

6.5.1 Pull-Down Voltage

The pull-down voltage of the MEMS switch is determined by the effective spring constant, the air gap height, and the effective area of contact pads (capacitor). In order to lower the pull-down voltage of the switch, three different routes can be pursued which are: increasing the area of actuation (contact pads), diminishing the gap between the cantilever and bottom electrode, and designing a cantilever beam with low spring constant. In the first case, the area can only be increased by so much before compactness becomes a prevailing issue. In the second case, the switch isolation associated with the RF signal restricts the value of the gap. Design of a cantilever beam with low equivalent spring constant is the approach with the most potential which is used to reduce the pull-down voltage, since the design of the springs does not considerably impact the size, weight, and RF performance of the circuit [112, 126, 127, 130].

To reduce the pull-down voltage, the key is a cantilever beam structure of low spring constant k . There are many variations of shapes of cantilever beam that can be used to lower the effective spring constant, but the cantilever beam structure should be chosen to provide very low values of spring constant in a compact area as well as providing high cross-axis sensitivity between vertical and lateral dimensions. Cantilever beams with different spring constants are studied in this work. Figure 6 - 6 show cantilever beam structures with different spring constants which have been used in this work to reduce the pull-down voltage of MEMS switch.



a) Cantilever beam with solid suspensions



b) Cantilever beam with meandered suspensions

Figure 6 - 6 : Cantilever beam structure of different spring constant.

The effective spring constant of a cantilever beam can be derived for non-meandered suspension as

$$k = \frac{Ewt^3}{4l^3} \quad (6.12)$$

and for meandered suspensions by

$$k = \frac{Ew\left(\frac{t}{L_c}\right)^3}{1 + \frac{L_s}{L_c} \left(\left(\frac{L_s}{L_c}\right)^2 + 12 \frac{1+\nu}{1 + \left(\frac{w}{t}\right)^2} \right)} \quad (6.13)$$

where E and ν are the Young's modulus and Poisson's ratio for the metal, t is the thickness, w is the width, l is the length of the cantilever beam, L_s is the overall width of the spring, and L_c is the distance from the end of the spring to the start of the

meander [112, 115, 130]. The dimensions of meandered suspension are illustrated in Figure 6 - 7.

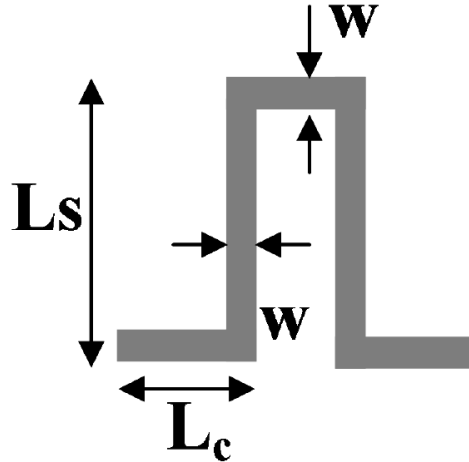


Figure 6 - 7: Illustration of dimensions of the meandered suspension.

The effective spring constant, k_{eff} , for the number of suspensions attached to the structure is

$$K_{eff} = \frac{nk}{m} \quad (6.14)$$

where m is the number of meanders in the suspension, and n is the number of suspensions attached to the structure [115].

The spring constant decreases linearly with successive addition of meanders to the meandered suspension. The design of the meandered suspension is of crucial importance in realizing switches with low pull-down voltage. Although this route is the one with the most flexibility in order to design MEMS switches with low pull-down voltages, it is very important to design the switch with a high cut-off frequency suitable for integration with the printed antenna at G-band frequencies.

6.5.2 Stiction Problem

Stiction is referring to any kind of adhesion that can occur between the MEMS switch contacts. The stiction is a consequence of the dominance of adhesion forces (surface force) over mechanical restoring force of the switch contact [136]. Stiction can be divided into two main categories: release stiction and in-use stiction. Release stiction occurs during the release process of the fabrication of MEMS switches, in which the elevated structures can collapse and adhere to the substrate due to the act of capillary forces and low spring force of the structures [137]. In-use stiction refers to adhesions that occur after the release stage, when the switch is in normal use. Release stiction reduces MEMS yield, while in-use stiction can greatly limit MEMS switches reliability. Many techniques have been reported to solve the problem of release stiction such as critical point drying, freeze sublimation drying, vapour phase etching of sacrificial layers, and surface modification to reduce the contact area [136, 138, 139]. These techniques can be effective at the elimination of release stiction, but they do not prevent in-use stiction. Therefore, in this work, we are only concerned on in-use stiction between the switch contacts.

One of the major problems in cantilever beam MEMS switch with metal-to-metal direct contact is stiction within operation, which occurs when the cantilever beam touches the contact pad, where the contacts surface become stuck in the form of strong adhesion [30-34]. These surfaces may be unable to separate even if the applied voltage has been removed as shown in Figure 6 - 8. It is difficult to predict the stiction, as this depends on the surface quality of the contact pads as well as on the environmental conditions. Also, with low pull-down voltage switches, stiction can be a serious problem. Therefore, before the integration of MEMS switches with printed antennas, the adhesion problem associated with the contacts needs to be resolved.

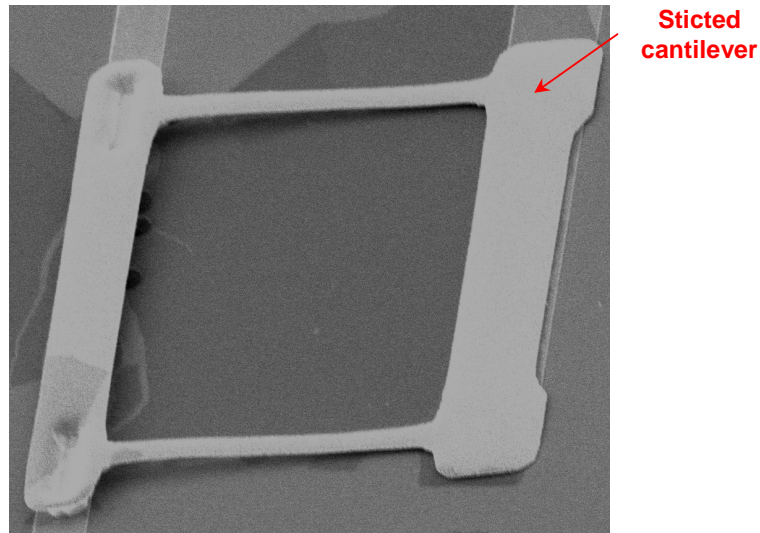


Figure 6 - 8 : Stiction phenomenon in the cantilever MEMS switch

In order to overcome the adhesion forces generated at the contact interface, many researchers have proposed reducing the surface adhesion by: (a) selecting contact materials with less adhesion; (b) addition of a thin dielectric layer to separate two conducting electrodes when actuated between the electrodes; (c) applying chemical surface treatment; (d) eliminating contamination with plasma cleaning; (e) increasing the equivalent spring constant by increasing cantilever thickness and shortening cantilever length.

Although these techniques can increase restoring forces, the pull-down voltage and insertion loss will increase significantly as a result, which reduces the device efficiency. Hence, the design parameters should be properly selected based on the knowledge of adhesive forces [32, 34, 126, 140]. In this work, we propose a new approach to provide enough restoring force to overcome the adhesion at the interface.

6.6 Proposed a New Cantilever Beam MEMS Switch Design

In managing the trade-offs between the switch parameters in this design, the pull-down voltage and stiction problem are given the highest priority, followed by the insertion loss and the electrical isolation. To reduce the spring constant of the cantilever beam to obtain a low pull-down voltage, there are three parameters that can be changed, which are cantilever beam material, thickness, and cantilever beam geometry. Of these parameters, only the changing of the beam geometry does not require any fabrication changes. Making changes to a fabrication process can be a costly endeavour and may add additional variables. For example, it can be more challenging to precisely control the beam thickness. For these reasons, we chose to alter the cantilever geometry. Also, changing the cantilever beam configuration can be used to lower the effective spring constant in a compact area as well as providing high cross-axis sensitivity between vertical and lateral dimensions. By carefully controlling the spring constant of the switch beam, the pull-down voltage can be tailored to a desired value.

In this work many cantilever beam MEMS switch configurations have been designed and fabricated in order to lower the pull-down voltage and solve the stiction problem. Figure 6 - 9 shows cantilever beam switches with different configurations. As a conclusion from the analysis of the measured performance of these MEMS switch configurations, it is clearly seen that the cantilever beam is the most crucial part of a MEMS switch since it determines the pull-down voltage and operation frequency and it is the source of the most dominant failure mechanisms in the switch. The cantilever beam must be strong enough so that the restoring force can overcome the stiction to ensure proper operation of the switch. However, while we aim to maximize the restoring force, there are several constraints that must be considered such as: the resonant frequency, which must be in G-band; the pull-down voltage, which must be in a reasonable range; the gap between cantilever contact and bottom pad contact, which must be above a minimum height to ensure proper isolation; and the switch size must be reasonable in order to ensure compatibility with printed antennas at G-band.

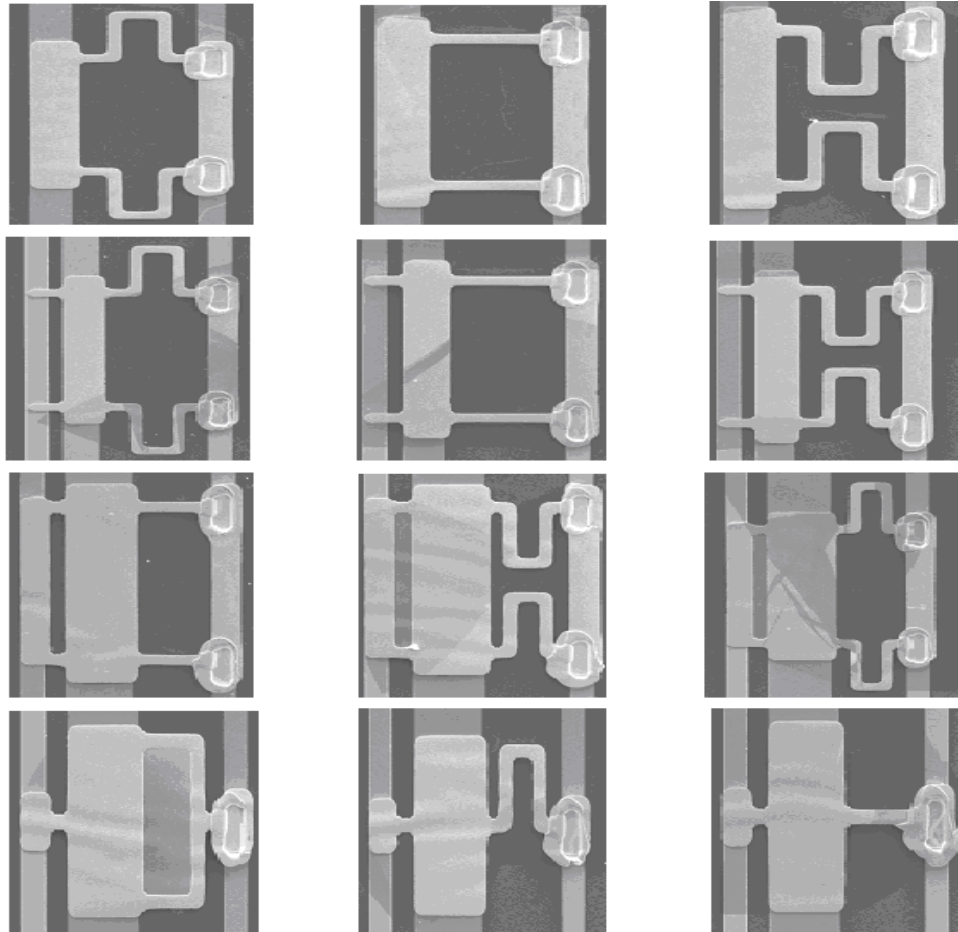


Figure 6 - 9 : Cantilever beam switches with different configuration.

Perhaps the best candidates for integration with a G-band printed antenna is the cantilever beam MEMS switch with non-meandered suspension which is shown in Figure 6 - 10, since it can be operated at high frequencies and is easy to integrate with the antenna.

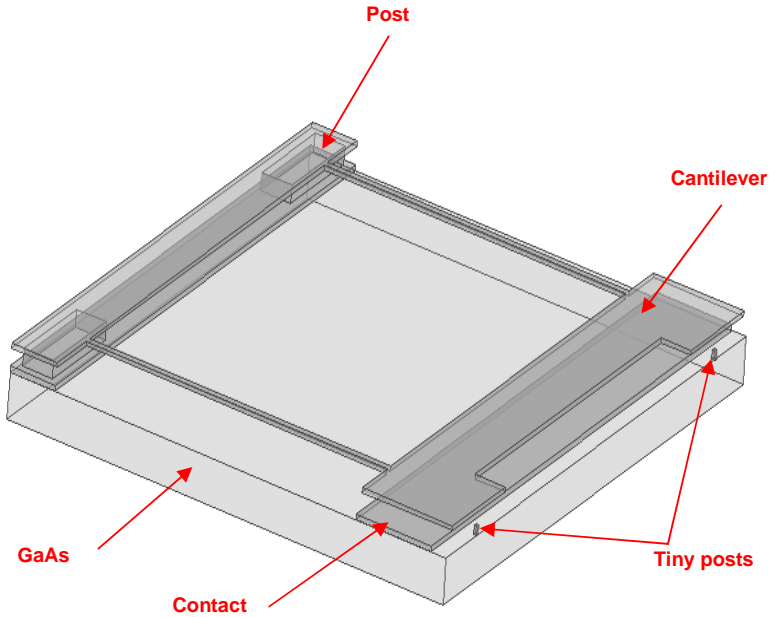


Figure 6 - 10 : Structure of cantilever beam MEMS switch

The proposed MEMS switch structure has a movable top cantilever beam which consists of a contact pad and two non-meandered suspensions connected with two supporting posts from one side at the input signal line. The other side is elevated above the bottom output signal line. The contact pad connects RF signal lines and enables actuation when a DC voltage is applied. The area of contact pad is a more limited variable than others because the larger contact pad, the lower the insertion loss, but also the poorer the Off-state electrical isolation because of the increased capacitive coupling between the contacts pads. This capacitance can be reduced by increasing the air gap, but this increase in the gap also increases the pull-down voltage because the same gap distance also determines the actuation capacitance. Also, the increase in the pad area increases the overall mass of the cantilever beam and thus the switching time of the MEMS switch. Many switches with different contacts pad area have been fabricated and their electrical and mechanical performance tested. The switch with $3175\mu\text{m}^2$ contact pad area was chosen to be integrated with the elevated patch antenna. It is large enough to provide lower pull-down voltages, good isolation and minimize the contact resistance - avoiding any ohmic heating due to passing a large DC or RF signal; hence the cantilever beam with $2\mu\text{m}$ thickness of gold was used.

When there is no DC voltage applied, the cantilever beam will be in the up position where the contact pad does not allow the RF signal to directly pass through the switch. The cantilever beam can be pulled down to the bottom contact by applying a DC voltage - creating a short circuit that allows the RF signal to pass through the switch. If the DC voltage is then reduced, the cantilever beam releases back up (typically at a lower voltage than the actuation voltage).

The geometry of cantilever beam in this design was chosen to produce the lowest possible pull-down voltage. Also, the gold was chosen as switch material since it provides a low Young's Modulus of 57GPa. However, reduction of the spring constant k might cause more stiction problems during operation. Therefore, in this design, we propose a simple integrated way to prevent the stiction problem using two tiny posts located on the substrate at the free end of the cantilever beam. These tiny posts will limit the downward motion of the contact pad and maximize the mechanical restoring force without significant effect on pull-down voltage. This solution should be effective no matter what the actual cause of stiction is.

To calculate pull-down voltage and compare with designed values, the cantilever beam dimensions were measured using a Scanning Electron Microscope S4700 as shown in Figure 6 - 11.

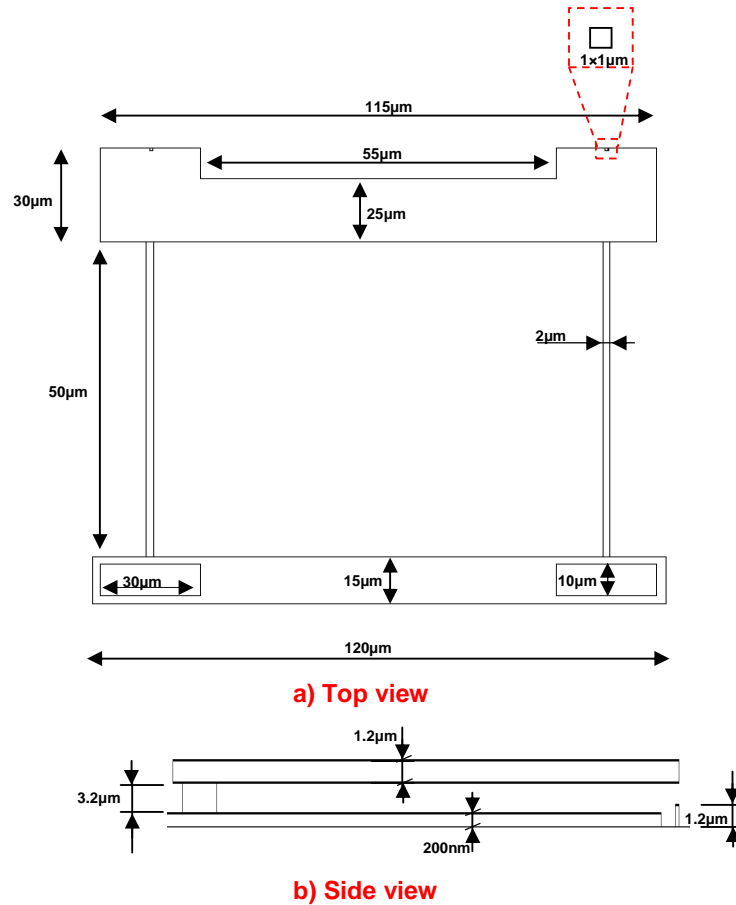


Figure 6 - 11 : Dimensions of cantilever beam MEMS switch.

The calculated pull-down voltage was 14.8 volt based on the Equation 6.6, which agrees very well with the measured value of 12.5 volt with an actuation current on the order of 1 mA which corresponds to a power consumption of 12.5 mw . It requires zero power to maintain the switch in either the Off-state due to the nature of the electrostatic actuation. Figure 6 - 12 shows I-V measurements of the proposed switch, this measurement was done using an on-wafer DC probe station. The switch Off-state capacitance and contact resistance have been calculated based on the measured dimensions and were approximately 9.54 fF and 0.615Ω , respectively. This results in high electrical isolation of -32.4 dB and low insertion loss of 0.053 dB at 200 GHz .

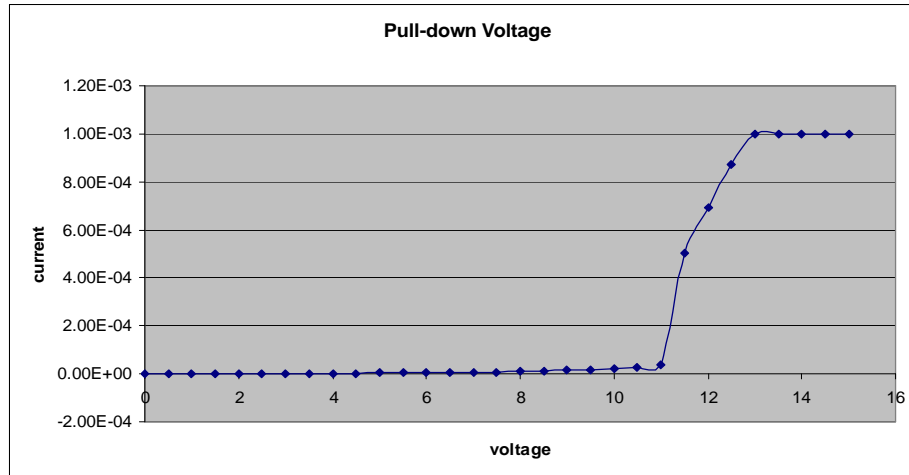


Figure 6 - 12 : I-V measurement of the fabricated cantilever MEMS switch.

The proposed switches utilize physical contact of metal with low contact resistance to achieve low insertion loss when actuated, so it can be operated at G-band frequencies with isolation defined by the coupling capacitance of the electrodes when the switch is open.

6.7 Fabrication Process of Proposed MEMS Switch

The cantilever beam MEMS switch fabrication is based on elevated micromachined structures technology. The switches were fabricated on a GaAs substrate with a substrate thickness of $630\mu\text{m}$ and a dielectric constant of 12.9. The most common materials that could be used for the fabrication of the MEMS switches are copper (Cu), aluminum (Al), and gold (Au). Examining the trade-offs of each one of them, gold was a logical choice as the switch material for our design [128], since it has good conductivity ($0.452 / \text{cm}\mu\Omega$), a smaller young's modulus, low propensity to form alien surface films, high melting point, easily deposited and is corrosion resistant. A schematic diagram of the cantilever beam MEMS switch fabrication process is shown in Figure 6 - 13.

The first two layers (dc switch pads, tiny posts) are built with the same process using E-beam lithography and evaporation and lift-off of a $30\text{nm}/250\mu\text{m}$ thickness for the switch pads and $50\text{nm}/1.2\mu\text{m}$ thickness for the tiny posts of nichrome/gold layer.

This was the stage where accurate pattern transfer was most important as the e-beam markers must be accurately reproduced to ensure that the alignment of subsequent layers is correct.

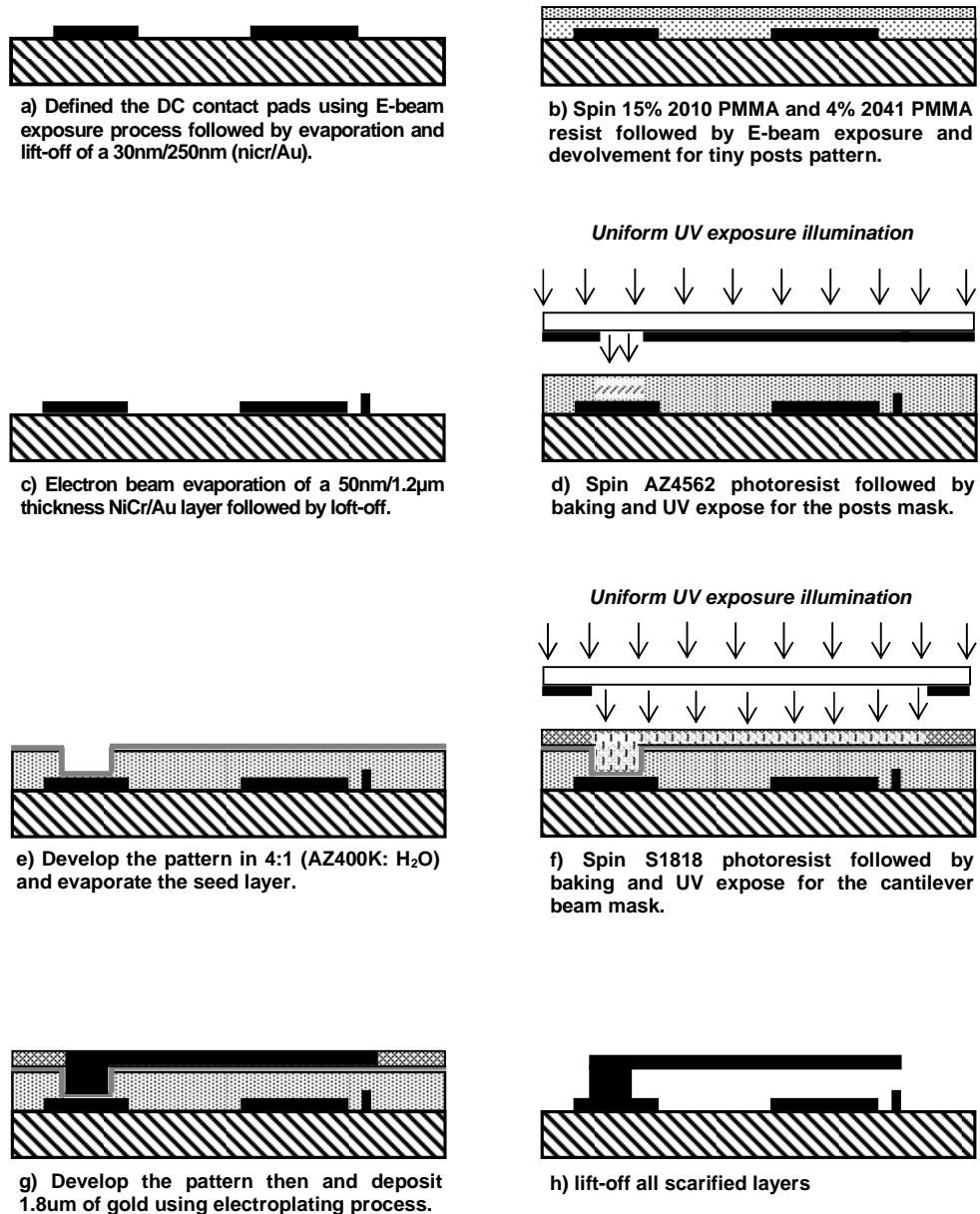


Figure 6 - 13 : A schematic diagram of the cantilever beam MEMS switch fabrication process.

The second stage is to build the cantilever beam using an air-bridge process. This stage starts with defining the supporting posts in AZ4562 photoresist followed by exposure and development. The thickness of photoresist will determine the height of the cantilever. The thickness can be varied as required by using different spinning speeds. A 50nm/10nm thickness nichrome/gold seed layer was deposited using the Plassys MEB Electron Beam Evaporator. The Titanium (Ti) layer provides adhesion for the posts contact, and the 10nm Au layer prevents the Ti layer from oxidising. A 40nm layer of Au was then sputtered to provide electrical contact for the subsequent electroplating. Next the switch cantilever beams were formed in 2 μ m thick S1818 photoresist followed by electroplating of 2 μ m thickness of gold. The top layer of 1818 photoresist was removed by flood exposure and development. The seed layer was then etched away in gold etching to remove the Au followed by Ti etch in 4:1 buffered HF. Finally the bottom layer of AZ4562 is removed by flood exposure and development. Figure 6 - 14 shows the SEM photo of cantilever beam MEMS switch.

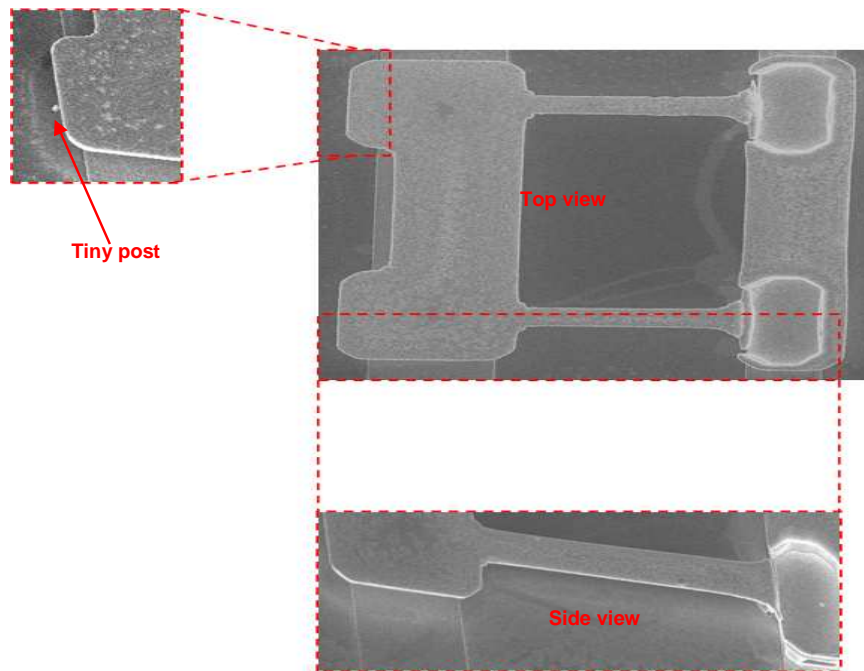


Figure 6 - 14 : SEM photo of cantilever beam MEMS switch.

6.8 Reconfigurable MEMS Antennas

An antenna that possesses the ability to modify its characteristics such as resonant frequency, polarization, radiation pattern or even a combination of these features, in real time is referred to as a reconfigurable antenna [26, 119]. Based on the definition, reconfigurable antennas can be divided into: frequency reconfigurable antennas, radiation pattern reconfigurable antennas, polarization reconfigurable antennas and multiple reconfigurable parameters of the antenna. However, frequency reconfigurable antennas are the most common and attractive for many applications, where it is required to have a single antenna that can be dynamically reconfigured to transmit or receive on multiple frequency bands [112, 119].

6.8.1 Antenna Design

An integral step in the implementation process is the selection of an appropriate antenna design. Before an antenna design is selected, several factors must be taken into consideration, such as the system performance requirements (minimum efficiency, power consumption, bandwidth, operating frequency, etc.), and also other constraints, such as the antenna size, cost, fabrication capabilities, etc. For static single-antenna designs, these factors need only be considered once in the selection of the antenna structure. However, when it comes to reconfigurable antennas, these factors must be considered at least twice; once for the antenna structure selection, and again for the reconfigurable technology being used. In reality, the system performance requirements should be considered each time the reconfigurable antenna switches from one reconfigurable state to the next, so the antenna design works optimally for all possible configurations[112].

The first part of the reconfigurable antenna design is the antenna structure. The structure of an antenna can take many shapes and sizes, depending on the established design requirements. Usually, the most important parameters to consider will be size, profile, ease of fabrication, and ability to reconfigure. The second part of the reconfigurable antenna design is selecting how the actual reconfiguration takes place. The reconfiguration process depends heavily on

which performance parameter should be altered, and which performance parameters should remain fixed. For example, a frequency reconfigurable antenna can be designed in two ways: one is to change the physical length of the antenna in order to change the operation frequency, the other is to change the impedance of the antenna [141].

6.8.2 Tuning Techniques for Frequency Reconfigurable Antennas

MEMS switches can be integrated with an antenna to tune the operating frequency of an antenna in a narrow frequency range. Many examples of frequency reconfigurable antennas have been described in the literature using different techniques, and their practical applications have been successfully used in communication systems. Most techniques are based on using MEMS either in the form of switches or as variable capacitances. In general, the techniques that are used to design and implement frequency reconfigurable antennas are:

- ***Design of reconfigurable antennas by changing resonance length of radiator element:*** The radiator element of the printed antenna may be a patch, dipole or slot. The resonant frequency of operation is selected by varying the length of the radiating element and thus changing its electrical length. The length of the radiating element can be altered by using MEMS switches along the radiator length. This will enable the antenna to operate at selective frequencies, i.e. f_1 or f_2 [108, 112, 113, 115, 142, 143]. Examples of reconfigurable printed antennas are shown in Figure 6 - 15.

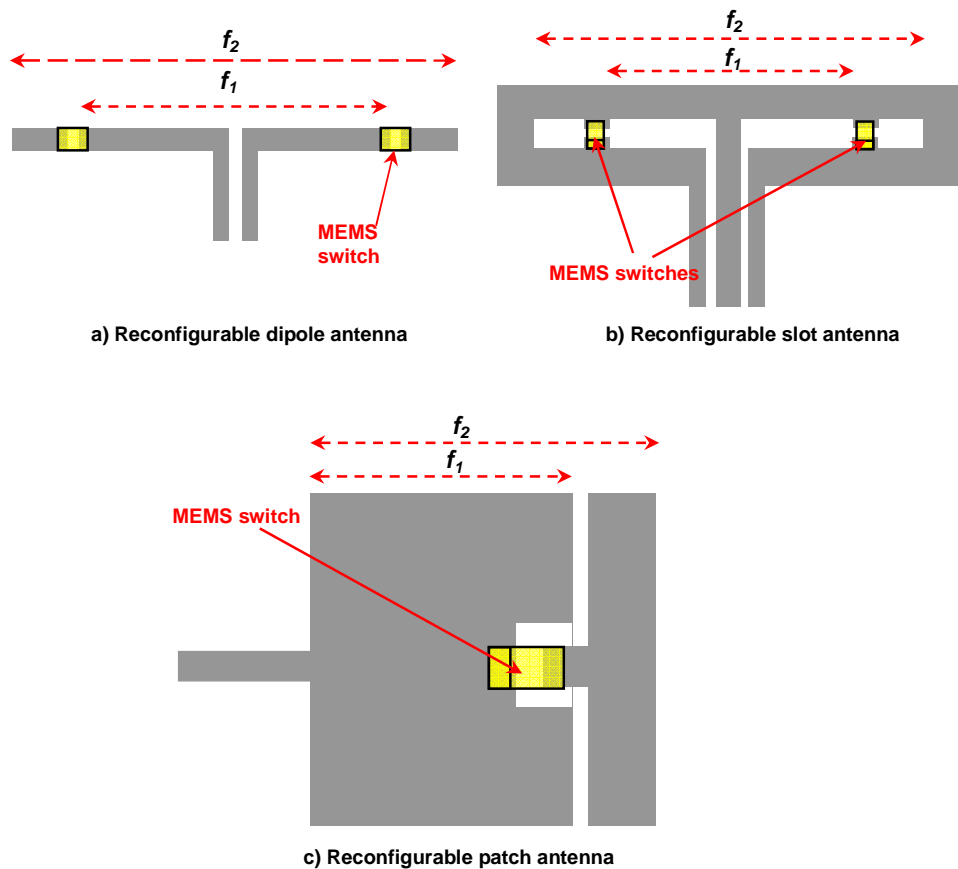


Figure 6 - 15 : Examples of reconfigurable printed antennas by changing resonance length.

Design of reconfigurable antennas by using slots in the radiator element: A variety of slots are usually introduced to detour the current path on the radiator element of printed antennas to control their resonant length. The length of these slots can be controlled by MEMS switches to reconfigure the printed antenna operating frequency [115, 144]. An example of a reconfigurable patch antenna is shown in Figure 6 - 16 - a using a slot to control the antenna resonance frequency. When the switch is in the off-state, the electric currents on the patch have to flow around the slot, as shown in Figure 6 - 16 - b, resulting in a relatively long length of the current path. Therefore, the antenna resonates at a low frequency. In contrast, when the switch is in the on-state, some of the electrical currents can go directly through the switch, as shown in Figure 6 - 16 - c. In this state, the average length of the current path is shorter so that the antenna resonates at a higher frequency. This method also utilizes a slot to meander the excited patch

surface current, which leads to a large reduction in the patch dimensions. It is important to realize miniaturization of the antenna [141, 145].

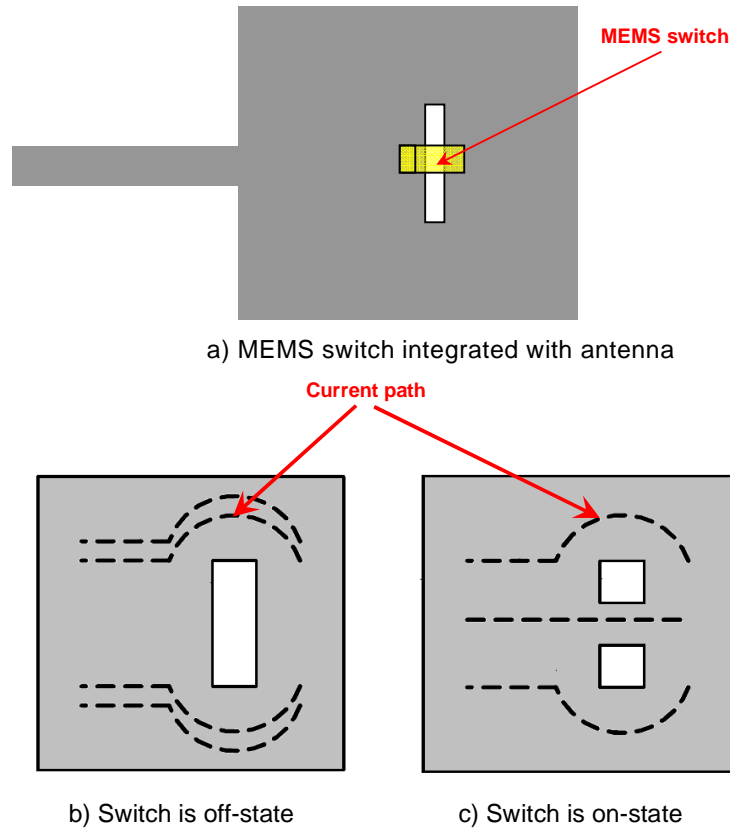


Figure 6 - 16 : Slotted patch antenna and its surface current path at different switch state

- **Design of reconfigurable antennas by using variable capacitors:** Loading the antenna with variable MEMS capacitors is an effective method to achieve frequency reconfiguration. The frequency is controlled by the change of the capacitance of the variable capacitor. Figure 6 - 17 shows reconfigurable antennas integrated with a stub connected with MEMS capacitors to tune the operating frequency. The characteristic impedance of the stub affects the resonant frequencies. MEMS capacitors are placed along the stub to change the characteristic impedance of the stub and to dynamically load the antenna [146].

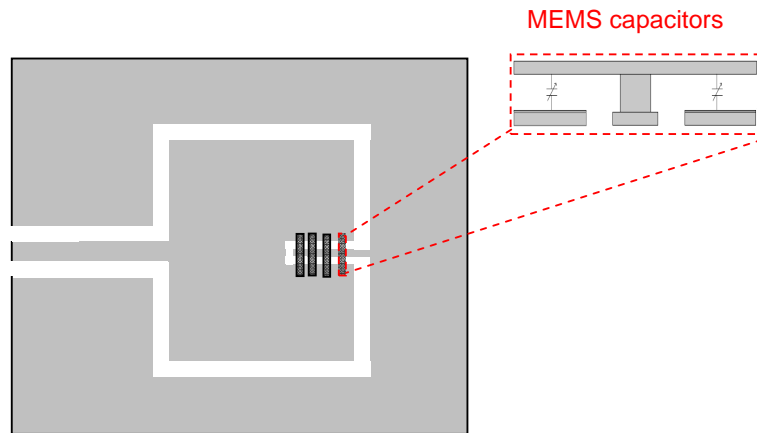


Figure 6 - 17 : Rectangular slot antenna loaded with MEMS cantilever type capacitors.

- Design of reconfigurable antennas by shorting the radiator element:**
 This approach can be used to tune the patch antenna via two integrated MEMS switches as shown in Figure 6 - 18. The MEMS switches are positioned at the far end of the patch radiating edge. The patch operates at its nominal frequency when the MEMS switches are in the *off* state. As with other rectangular patch antennas, frequency of operation is determined by the patch length L . When the MEMS actuators are turned to the *on* state, they add a capacitance in shunt with the input impedance of the patch. This added capacitance has the effect of lowering the resonant frequency of the antenna[147].

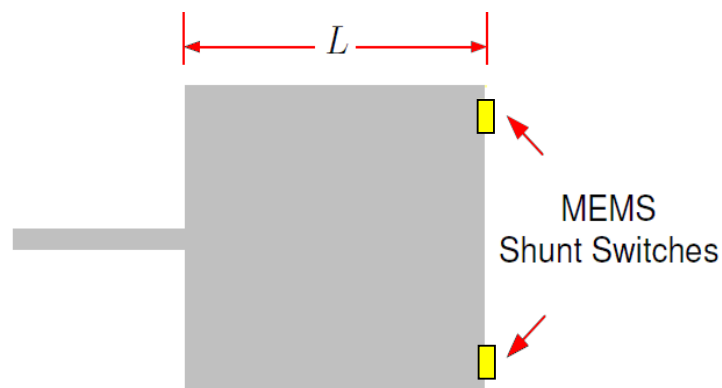


Figure 6 - 18 : Reconfigurable patch antenna using shorting switches

- **Design of reconfigurable antennas by changing the thickness of the antenna substrate:** It is well known that the thickness of the dielectric layer of the printed antenna is a major factor in determining the antenna resonant frequency. The antenna can be tuned by introducing an air gap between the substrate and the ground plane, which could lower the effective permittivity of the cavity under the patch. Hence, the resonant frequency of the antenna could be tuned by adjusting the thickness of the air gap [19]. For example the patch of a microstrip antenna can be printed on the thin movable film which is elevated above the ground plane as shown in Figure 6 - 19. The movable film deflects downward toward the fixed ground plane due to the electrostatic force of attraction caused by the applied dc bias voltage between the patch and the ground plane. This deflection decreases the air gap thereby increasing the effective permittivity of the antenna. This increase in effective permittivity results in a downward shift in the resonant frequency.

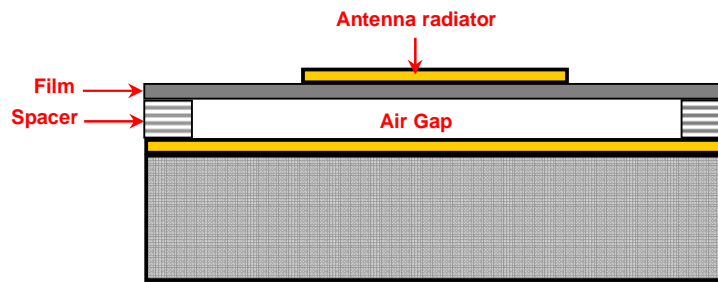


Figure 6 - 19 : Tuning printed antennas by changing the substrate thickness.

6.9 Proposed New Reconfigurable Antenna Designs

The real challenge is developing interconnect and feed structures to join the antenna elements and MEMS switches together in such a way that the antenna may be reconfigured to meet the needs of various applications. In this section we will present novel two reconfigurable elevated patch antennas, which are designed on a high dielectric substrate GaAs and operated at G-band frequencies. Still other reconfigurable antennas are under investigation and their configurations are shown in the Appendix B

6.9.1 Reconfigurable Elevated Patch Antenna

This design presents novel compact designs of frequency reconfigurable elevated patch antennas capable of achieving high tuning ranges with using low voltage cantilever beam MEMS switch. The antenna design is based on elevated patch antenna configuration since it is particularly suitable for operation at G-band frequencies - as discussed in chapter 5.

Antenna Design

Figure 6 - 20 shows the schematic view of the proposed frequency reconfigurable elevated patch antenna. The antenna is monolithically integrated with MEMS switches placed on a CPW stub for tuning the resonant frequency.

Reconfigurability of the operating frequency of the patch antenna is achieved by loading the antenna feed line with a variable reactive load. The MEMS reactive load is a CPW stub on which MEMS switch is placed to change the state of the stub from open circuit to short circuit, or in the other words from capacitance reactive load to inductance reactive load. Changing the imaginary part of the antenna input impedance lead to tuning the resonance frequency of the antenna. The tuning range of the antenna can be controlled by adjusting the length of the stub at short and open circuit and connected position from the antenna patch. The length and position of the CPW stub were optimized using HFSS simulation software. The stub length is $0.14mm$ when the switch is in the up-state while

0.047mm when the switch is in down-state, and it is located at 0.46mm from the patch feeding post. The cantilever beam MEMS switch which has been discussed in section 6.6 was used to tune the antenna resonant frequency. The states of the MEMS switch, hence the loading reactance, can be changed by the dc actuation voltage applied between the dc contact pads and switch cantilever beam. Thus, the CPW stub with MEMS switch provides a variable reactance input impedance, resulting in tuneability in the resonant frequency.

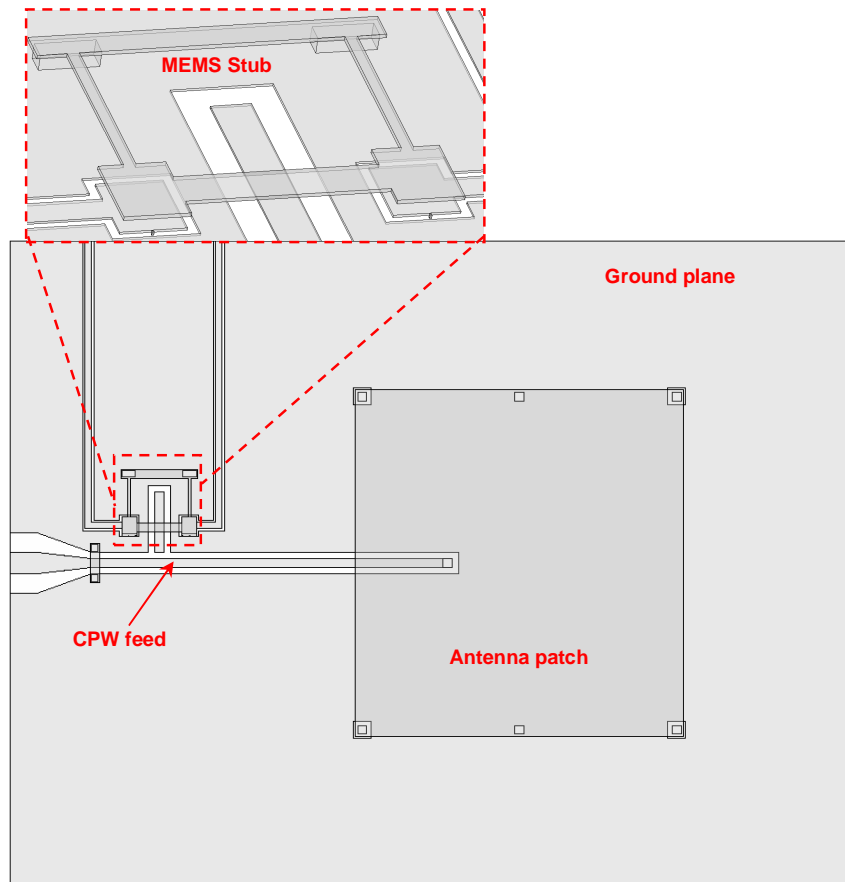


Figure 6 - 20 : Configuration of rectangular elevated patch antenna design.

The antenna radiated patch is elevated above a CPW ground plane by $13\mu\text{m}$ height of gold posts to reduce the dielectric substrate effects, and in order to decide appropriate dimensions of the antenna and the optimum design, investigation was performed by simulation software HFSS. The dimensions of the rectangular patch are $L \times W = 746\mu\text{m} \times 806\mu\text{m}$ with $2\mu\text{m}$ thickness. The patch is

fed by a gold feeding post connected to a CPW feed line on gallium arsenide (GaAs) substrate. The antenna ground plane has to be large enough to reduce diffraction of the edges for reducing ripples in the main pattern and backward radiation, and to shield the antenna from the underlying elements and vice versa. Hence, for this design, the ground plane dimensions were chosen as $W_s \times L_s = 1.5\text{mm} \times 2.03\text{mm}$ with $1.2\mu\text{m}$ thickness of gold to reduce the antenna ohmic losses.

Fabrication Process

The antenna fabrication was based on elevated micromachined structures technology. The antenna has four levels of height, the first level consists of $30\text{nm}/250\text{nm}$ NiCr/Au for dc switch feed network pads, then the dc contact pads covered with 50nm of silicon nitride to isolate them from the antenna ground plane, this is followed by layer of $50\text{nm}/1.2\mu\text{m}$ NiCr/Au to form the antenna ground plane and the switch posts. The cantilever beam of MEMS switch and air-bridge were elevated by $3.2\mu\text{m}$ gold posts, and finally the patch was elevated by $13\mu\text{m}$ gold posts. The antenna was fabricated on a $630\mu\text{m}$ thickness SI GaAs substrate with a dielectric constant of 12.9 . The height of the MEMS switch and patch above the substrate can be varied as required for optimum antenna performance by changing the thickness of the photoresist layers, which is used in the airbridge process. This can be used to further enhance the patch bandwidth when we cannot change the substrate thickness for the sake of the rest of the module circuits. Figure 6 - 21 shows a micrograph of the fabricated reconfigurable antenna.

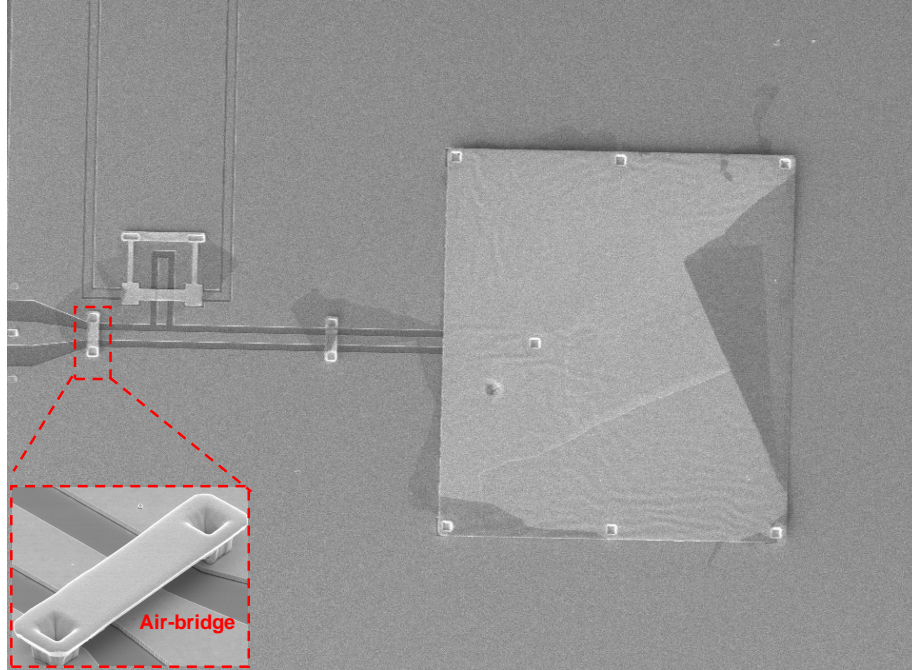


Figure 6 - 21 : SIM photo of fabricated reconfigurable antenna

Results

The proposed antenna is designed using an Ansoft HFSS simulator, and the fabricated antennas were characterized using an Agilent PNA Vector Network Analyzer and 140GHz to 220GHz OML heads and in wafer dc prop station. The resonant frequency of the antenna when the MEMS switch is in the up-state occurs at 173GHz with good matching of 22dB and bandwidth of 5GHz from 171GHz to 176GHz . As the height of the cantilevers moves down to short the stub at 12.5volt pull-down voltage, the resonant frequency shifts to 184GHz with excellent matching of 36dB and with nearly the same bandwidth as in the off-state. Figure 6 - 22 and Figure 6 - 23 show the simulation and measurement return loss of the reconfigurable antenna at different switch states. The slight different between the simulation and measurement return losses can be attributed to the small geometrical disparity between the fabricated prototype and the simulated one. However, this can be easily overcome in an industry manufacturing process where all of the fabrication conditions are optimized for a specific process. The antenna radiates broadside for the two resonances and changing the reactive input impedance does not cause any adverse effect on the radiation patterns. Also, the

dc biasing connection between the top and bottom plates of MEMS switch does not have a significant effect on the antenna performance since it is separately connected.

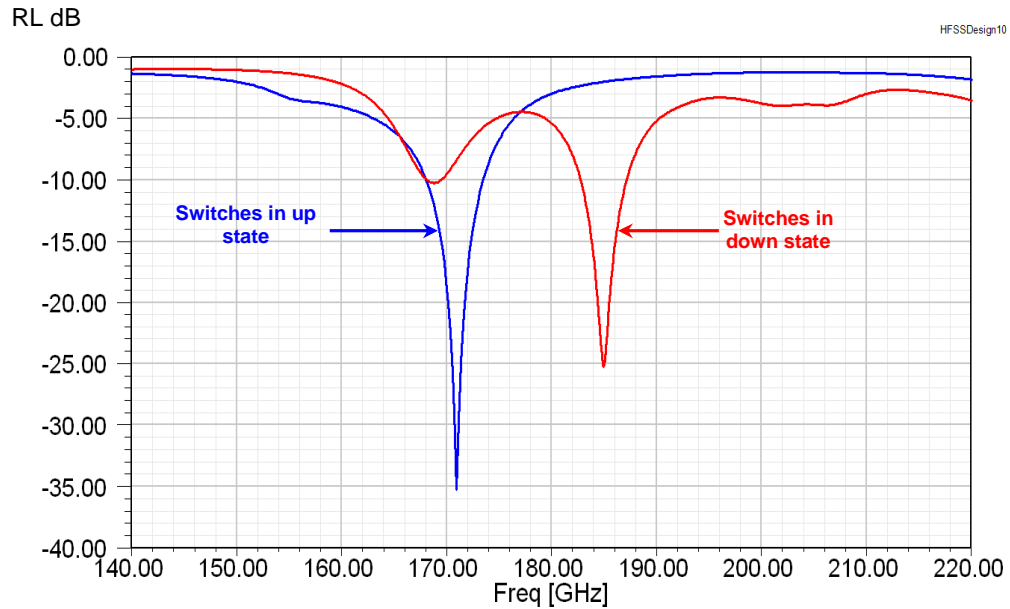


Figure 6 - 22 : Simulated results of return loss antenna at different switch states.

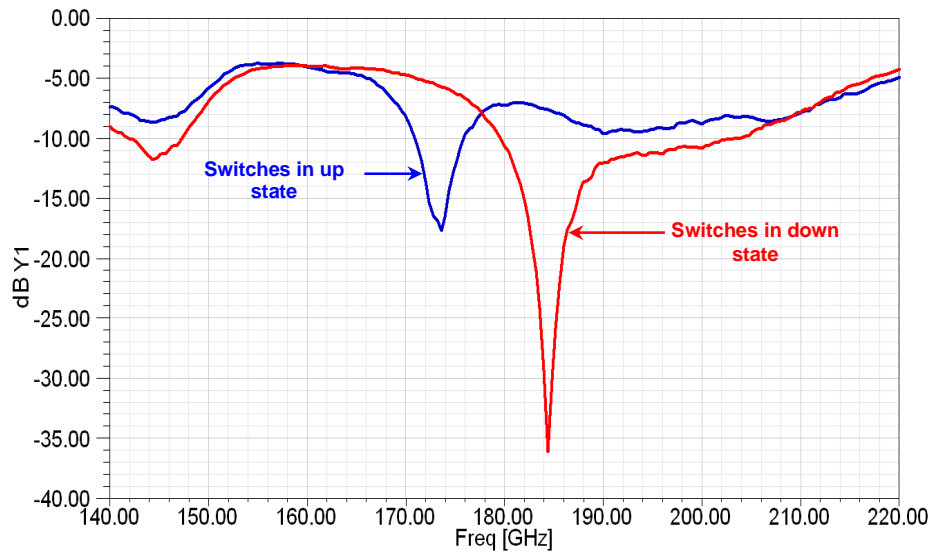


Figure 6 - 23 : Measured results of return loss antenna at Off and On state of MEMS switch.

Proposed antenna demonstrates a broadside radiation pattern over its bandwidth. The maximum antenna gain is 1dB when the switch at off-state while is 1.3dB when the switch at on-state. Figure 6 - 24 shows 3-D simulated radiation pattern for the antenna gain at Off and On state of MEMS switch.

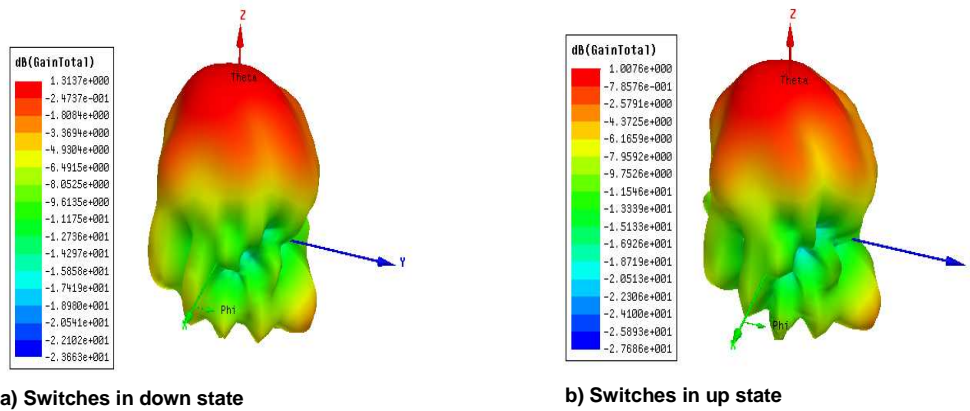


Figure 6 - 24: 3-D simulated radiation pattern (Gain dB) at Off and On state of MEMS switch.

Although the CPW stub increases the antenna dimensions significantly, it is a simple way of loading the elevated patch antenna with a MEMS switch without a significant effect on the antenna performance. Therefore, it can be concluded that the proposed antenna configuration offers new method to tune elevated antenna at G-band region.

6.9.2 Reconfigurable Proximity Coupled Elevated Patch Antenna

Other new design of reconfigurable elevated patch antenna without using MEMS switch will be discussed in this design. It is well known that the patch height of the elevated patch antenna is a major factor in determining the antenna resonant frequency, as it has been discussed in chapter 3. For example, By decreasing the patch height, the fringing fields from the patch edges will decrease, which decreases the extension in the patch length and hence the effective length of the patch, thereby increasing the resonance frequency. Therefore, the basic idea of this design is based

on electrostatically adjusting the patch height to control the resonate frequency of the antenna.

Antenna design

The reconfigurable antenna design based on the proximity coupled elevated patch antenna configuration which has been discussed in section 5.5. The geometry of the reconfigurable elevated proximity coupled patch antenna is shown in Figure 6 - 25. The antenna patch was elevated using a number of meandered suspensions connected with gold posts over the ground plane. The meandered suspensions were used to reduce the actuation voltage, since they give low value of spring constant. The posts number was determined considering the trade-off between electrical performance and mechanical robustness. A large number of posts would offer a stronger and more rigid mechanical performance at the expense of an increase the actuation voltage and back lobs radiation. In this design, the smallest possible number of posts, while maintaining mechanical robustness, is decided as six; one gold supporting post is used for each patch vertex positioned within $25 \times 25 \mu\text{m}^2$ rectangular slots and one for each middle point of the patch length edge connected directly with substrate. The patch is excited by proximity coupling using a loop slot formed in the ground plane and connected with end of 50Ω CPW feed line underneath the patch on GaAs substrate. The centre of the loop slot is also used as dc pad to actuate the elevated patch. The patch is designed at $10.5\mu\text{m}$ height when they are not actuated and it can be lowered down to different heights at different actuation voltages.

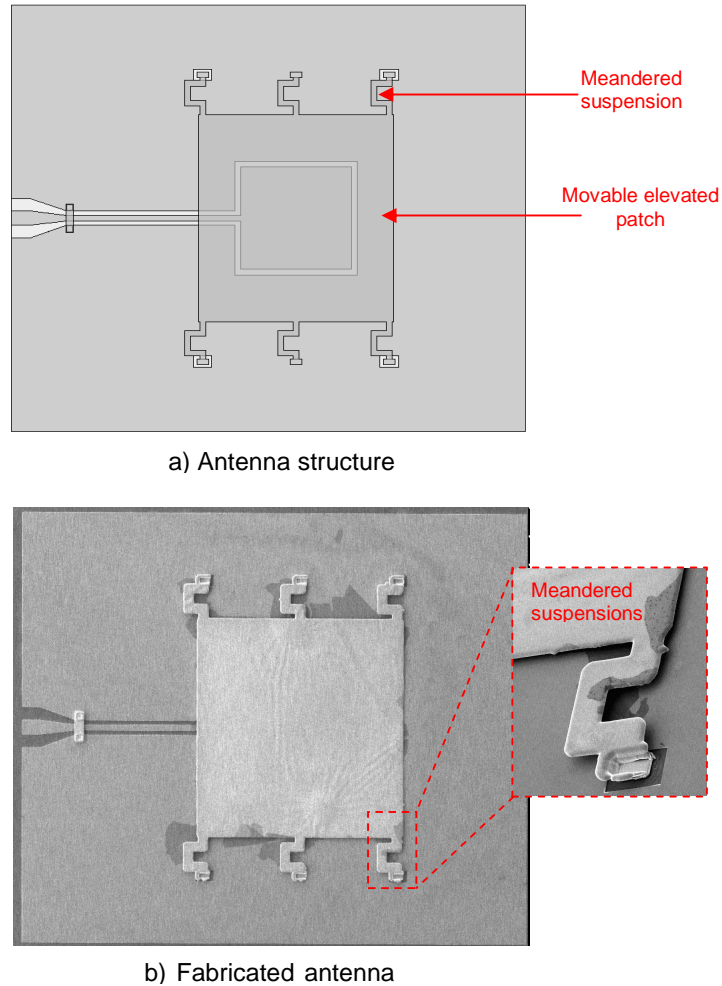


Figure 6 - 25 : Geometry of the reconfigurable elevated proximity coupled patch antenna.

The operating frequency of this antenna is electrostatically tuned by applying a dc bias voltage between the patch and the centre of the loop slot. The movable elevated patch deflects downward toward the fixed ground plane due to electrostatic force of attraction caused by the applied dc bias voltage. Below the pull-down voltage, the patch height gradually decreases with increasing dc voltage and therefore the antenna exhibits a continuous upward shift in the resonant frequency. Above the pull-down voltage, the elevated patch antenna collapses onto the ground plane; hence the antenna should not operate above the pull-down voltage. To determine the pull-down voltage, the elevated patch can be modeled as an air-bridge switch with six meandered suspensions; therefore the Equation 6.6 can be used to calculate the pull-

down voltage and Equation 6.13 to calculate the effective spring constant. Based on measurement dimension of the antenna the calculated pull-down voltage is *115 volt*.

The antenna was fabricated on a GaAS substrate with a thickness of $630\mu\text{m}$ and a dielectric constant of 12.9 using the same process which has been used to fabricate two level antennas. Figure 6 - 25 - b shows the SEM image of the fabricated antenna. For the proposed operating frequencies at G-band the dimensions of the patch have been optimized using HFSS simulation software, and they are $W \times L = 685\mu\text{m} \times 730\mu\text{m}$.

Results

The return loss of the elevated patch antenna was measured using an agilent vector network analyzer with coplanar probes with $100\mu\text{m}$ pitch size. For dc biasing the antenna the grounds of the pitch connected with the ground of the dc source and signal connected with positive. The measured return loss of the antenna for applied DC bias voltages of 0 volt and 42volt corresponding to the up and down positions, respectively. In the up-position, the resonant frequency of the antenna is about 189.2GHz with 18.7dB return loss. As the height of the patch reduced by Applying the dc voltage, the resonant frequency shifts to 191GHz at 42volt dc voltage and with nearly the same bandwidth. Figure 6 - 26 shows the measurement return loss of the reconfigurable antenna at different voltage.

Proposed reconfigurable antenna demonstrates also a nearly broadside radiation pattern over its resonant frequencies. The maximum antenna directivity is 6.2dB when there is no applied voltage. Figure 6 - 27 shows 3-D simulated radiation pattern for the antenna directivity when there is no applied voltage.

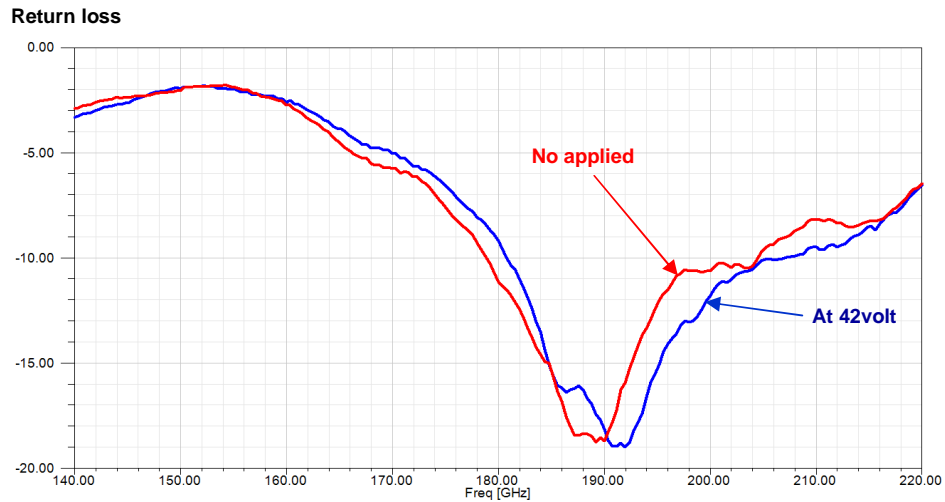


Figure 6 - 26 : Measured return loss of reconfigurable proximity coupled patch antenna at 0 and 42volt.

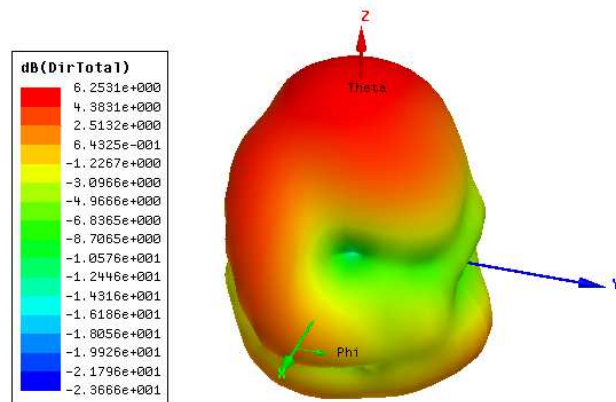


Figure 6 - 27 : 3-D simulated radiation pattern for the antenna directivity when there is no applied voltage.

The important feature of the reconfigurable elevated patch antenna presented here in this section is that it is easy to fabricate using two level fabrication processes and there is no need for dc feeding network since the dc biasing and RF signal can be connected between the signal and grounds of CPW port. This new tunable elevated patch antenna is also suitable for implementation of low cost and low profile RF front end, tunable antenna arrays, and tunable reflector arrays.

6.10 Conclusion

In conclusion, it can be seen that the proposed antenna and switch configurations described in this chapter, offer new method to design and fabricate MEMS switches and reconfigurable patch antennas. The fabrication scheme offers a new method for monolithic integration with active MMIC transceiver circuitry. Also, the antenna design is a solution reduces undesired substrate effects, and a viable route to higher levels of integration and functionality problem. To our knowledge, this is the first ever-reported MEMS reconfigurable elevated patch antenna operating at G-band frequencies and fabricated on high dielectric substrate.

7. Conclusions and Future Work

7.1 Conclusions

The continued growth in applications exploiting the millimetre and sub-millimetre frequency bands for imaging and sensing and communications has increased the need for improved high-frequency on-chip antenna performance. As discussed in the previous chapters, micromachining technology is key to high-frequency antennas, and requires careful design and realisation to improve performance as the device is scaled at wavelength size dimensions.

This thesis presented a wide ranging insight into the design, analysis, fabrication and testing of micromachined printed antennas that are suitable for MMIC integration at G-band frequencies (140GHz - 220GHz). A number of different novel antenna configurations have been presented in this thesis for the first time. The presented antenna configurations offer significant improvements in performance compared with previously reported work. This thesis has also investigated MEMS integrated antennas in order to achieve multiband operation at G-band. The developed work detailed various aspects associated with lowering the pull-down voltage and preventing the stiction problem of MEMS switches and shows how they can be integrated with industry standard MMICs fabrication process. This allows on chip integration and realization of novel multiband antennas, and also high isolation MEMS switches can be realized using the same developed technology in this thesis. Antennas have been designed as a single

element and all the limitations of the design and fabrication have been taken into account with promising performance and integration capabilities.

The introduction chapter described the motivating factor for carrying out this work. In that process, it outlined the future wireless communication systems requirements and challenges, the advantages and applications of G-band frequencies are also presented. Accordingly, the outline of the study was worked out, with a brief description of what is to be expected in each of the chapters.

To help evaluate antenna performance and to understand the challenges faced when designing and analysing antennas, it is necessary to provide some background information on some of the key parameters and performance metrics. The second chapter presented the basic theory of antennas and the fundamental parameters used for evaluating antenna performance. An insight is given into the printed antennas with a focus on the characteristics of patch antennas and their substrate-related effects at millimetre-wave frequencies. The high dielectric constant substrate is an easier medium for the propagation of surface waves; hence our designs are based on elevated antenna structures to avoid these effects.

Before starting to design an antenna, specifications or requirements that the antenna has to fulfil have to be taken into account. The design of printed antennas require an understanding of the electrical and physical properties of the antennas and an awareness of fabrication and simulation software related issues in order to obtain proper results. There is no ideal process to design and analyse patch antennas and closed form equations to calculate the parameters which give the best performance do not exist. Therefore the dimensions of the antenna are roughly evaluated and then altered iteratively until the desired performance, or the closest possible approximation, is achieved. The antenna designs of this work were done through using transmission line model analysis to calculate the initial dimensions of the antenna and then simulation software is used to predict the antenna performance, taking into account its desired specifications. This thesis presents High Frequency Structure Simulator (HFSS) simulation software as an

effective tool for modelling and predicting antenna performance, combining it with a powerful PC to increase the design accuracy through finer meshing. However, understanding of the electromagnetic behaviour of the structure to be simulated is usually needed. Therefore, a designer has also to be aware of the software-related issues, such as the port definition and boundary conditions, in order to properly model the real environment of the antenna. Many design factors have been studied and optimised in this work as a part of a trade-off between the antenna performance and the physical realization considerations of the elevated patch antennas. The electromagnetic design validation of the proposed antennas in this work depends on matching between the simulation and measurement s-parameters, which are measured using a Vector Network Analyzer.

A new approach for fabricating micromachined antennas, based on the development of the elevated structure process, has been introduced in this work to fulfil the fabrication process requirements. A key enabling technology for the successful development of the fabrication process is combining the photolithography with e-beam lithography processes to create 3-D structures. The antenna fabrication scheme provides a new method for fabrication of 3-D multilevel structures without etching the substrate. The antennas went through several fabrication steps and experience was accumulated through repeated cycles of fabrication and measurement of antenna performance. The antennas were fabricated on a GaAs substrate with a substrate thickness of 630 μm and a dielectric constant of 12.9. Gold was used as a metal to build the antenna structures because of its high performance and low resistivity characteristics. The new process of the antenna fabrication has the advantage that the antennas can be fabricated using multiple levels, and the height of the elevated antennas can be specified in the process and can be varied by several microns, regardless of the substrate used. This can be used to further enhance the antenna bandwidth when we cannot change the substrate thickness for the sake of the rest of the module circuits. Thus, the elevated antenna can meet different application requirements and can be utilized as a substrate independent solution.

Different new feeding mechanisms for elevated micromachined antennas were presented in this work for the first time and offer more degrees of freedom for antenna design. These feeds provide low loss and less dependence of the characteristic impedance on the substrate height and permittivity. In addition, new alternative topologies of G-band micromachined antennas on high dielectric substrate for MMICs applications have been presented. Experimental and simulation results are provided to demonstrate the effectiveness of the antenna designs and demonstrate the feasibility of G-band micromachined antennas on high dielectric substrates. For example, the measurement results of three level proximity coupled patch antenna showed an excellent match of -32dB at 196GHz and bandwidth of 15GHz with high gain of 7.18dB and an excellent front-to-back ratio of 32.2dB indicating good coupling between the feed and the patch. This indicates a high radiation efficiency structure across the designed bandwidth. All proposed antenna configurations have several advantages over previously reported micromachined antennas on high dielectric substrates such as: the antenna topologies offer an easy method for integration with MMIC processes and they eliminate the undesired substrate effects since the antenna substrate is essentially air (the lowest possible dielectric constant). This increases the radiation efficiency, gain, and the radiation bandwidth. Furthermore, the corresponding dimension for antennas working at G-band is on the millimetre scale, thus allowing integration of 3-D antennas with RF circuitry on a single chip. Therefore, the performance exhibited by the antenna makes it an attractive candidate for many millimetre-wave applications.

A key enabling technology for the successful development of reconfigurable multi-band antennas is the development of switches with low loss, high isolation and low bias power requirements. MEMS switches were introduced in chapter six as a prime candidate for integration with elevated patch antennas at G-band to enhance the antenna performance and make very efficient use of limited area. Cantilever beam metal-contact switches have been selected for this work to integrate with elevated patch antenna. Recent work by other researchers show the cantilever beam MEMS switches have very good performance, but the current

implementations still suffer from a high pull-down voltage and the stiction problem - restricting their integration with printed antennas. Lowering the pull-down voltage in this work is based on reducing the spring constant by changing the cantilever beam geometry of the MEMS switch, since it does not require any fabrication changes and lowers the effective spring constant in a compact area as well as providing high cross-axis sensitivity between vertical and lateral dimensions. The stiction problem has been overcome in this work by a simple integrated method using two tiny posts located on the substrate at the free end of the cantilever beam. These tiny posts limit the downward motion of the contact pad and maximize the mechanical restoring force without significantly affecting the pull-down voltage. Also, this chapter has presented two novel reconfigurable elevated patch antennas. The first antenna is monolithically integrated with MEMS switch for tuning the resonant frequency. Reconfigurability of the operating frequency is achieved by loading the antenna feed line with a CPW stub on which the MEMS switch is placed to change the CPW stubs imaginary part of the antenna input impedance. The resonant frequency of this antenna when the MEMS switch is in the up-state occurs at 173GHz with good matching of 22dB and bandwidth of 5GHz , and as the height of the cantilevers moves down to short the stub at 12.5volt pull-down voltage, the resonant frequency shifts to 184GHz with excellent matching of 36dB and with nearly the same bandwidth as in the off-state. The second antenna is a new design of reconfigurable elevated patch antenna without using MEMS switch. The basic idea of this design is based on electrostatically adjusting the patch height to control the resonate frequency of the antenna. To our knowledge, this is the first ever-reported MEMS reconfigurable elevated patch antenna which operates at G-band frequencies and is fabricated on a high dielectric substrate.

7.2 Future Work

Although the research for this thesis has been extensive, there are still several unexplored areas of research that can be suggested for future work such as:

- Build more complicated 3-D structures to enhance a high-level integration of several passive components and transmission media.
- The packaging of printed antennas and MEMS switches is very important and has proven to be very challenging due to requirements related to performance and cost requirements.
- Elevated patch antenna arrays fed with CPW, EC-CPW or EMS lines can be designed and investigated on high dielectric substrates to increase the gain and radiation efficiency of the antenna. Also, it is possible to have an array whose pattern can be reconfigured by controlling the patches feed using MEMS switch. This can add another degree of freedom to the design of the array.
- Building an on-wafer anechoic chamber to measure the printed antenna radiation pattern at G-band using standard microwave laboratory equipment will be a very challenging task as antenna measurements at this band pose several difficulties, mainly due to the small physical size of the antennas and the requirement for wafer probing as the only means of connecting to the antenna.
- The examination and development of new reconfigurable antenna designs which incorporate low pull-down voltage MEMS switches to achieve bandwidth control or allow the antenna to steer the antenna beam is a challenging area in which these antennas could be improved.

References

- [1] S. K. Pavuluri, C. H. Wang, and A. J. Sangster, "A High-Performance Aperture-Coupled Patch Antenna Supported by a Micromachined Polymer Ring," *Antennas and Wireless Propagation Letters, IEEE*, vol. 7, pp. 283-286, 2008.
- [2] S. E. Gunnarsson, N. Wadefalk, J. Svedin, S. Cherednichenko, I. Angelov, H. Zirath, I. Kallfass, and A. Leuther, "A 220 GHz Single-Chip Receiver MMIC With Integrated Antenna," *Microwave and Wireless Components Letters, IEEE*, vol. 18, pp. 284-286, 2008.
- [3] K. Hettak, G. A. Morin, and M. G. Stubbs, "The integration of thin-film microstrip and coplanar technologies for reduced-size MMICs," *Microwave Theory and Techniques, IEEE Transactions on*, vol. 53, pp. 283-291, 2005.
- [4] G. M. Rebeiz, "Millimeter-wave and terahertz integrated circuit antennas," *Proceedings of the IEEE*, vol. 80, pp. 1748-1770, 1992.
- [5] G. P. Gauthier, J. P. Raskin, L. P. B. Katehi, and G. M. Rebeiz, "A 94-GHz aperture-coupled micromachined microstrip antenna," *Antennas and Propagation, IEEE Transactions on*, vol. 47, pp. 1761-1766, 1999.
- [6] G. Liu, C. L. Law, M. J. Rajanik, and H. Yang, "A switchable MEMS antenna for 38/60 GHz millimeter wave communications," in *Microwave and Millimeter Wave Technology, 2004. ICMMT 4th International Conference on, Proceedings, 2004*, pp. 86-89.
- [7] E. Erdil, K. Topalli, M. Unlu, O. A. Civi, and T. Akin, "Frequency Tunable Microstrip Patch Antenna Using RF MEMS Technology," *Antennas and Propagation, IEEE Transactions on*, vol. 55, pp. 1193-1196, 2007.
- [8] E. R. Brown, "RF-MEMS switches for reconfigurable integrated circuits," *Microwave Theory and Techniques, IEEE Transactions on*, vol. 46, pp. 1868-1880, 1998.
- [9] C. Balanis, *Antenna Theory: Analysis and Design*: John Wiley & Sons Inc, 2005.
- [10] D. Pozar, "Consideration for Millimetre Wave Printed Antennas," *IEEE Transactions on Antennas and Propagation*, vol. AP-31, 1983.
- [11] K. Hettak, G. Delisle, and M. Boulmalf, "A novel integrated antenna for millimeter-wave personal communications systems," *Antennas and Propagation, IEEE Transactions on*, vol. 46, pp. 1757-1758, 1998.

References

- [12] L. B. Lok, C. J. Hwang, H. M. H. Chong, K. Elgaid, and I. G. Thayne, "Measurement and modeling of CPW transmission lines and power dividers on electrically thick GaAs substrate to 220GHz," in *Infrared, Millimeter and Terahertz Waves*, 2008. IRMMW-THz 2008. 33rd International Conference on, 2008, pp. 1-2.
- [13] K. Elgaid, I. G. Thayne, G. Whyte, J. Martens, and D. Culver, "Parasitic Moding Influences on Coplanar Waveguide Passive components at G-Band Frequency," in *Microwave Conference*, 2006. 36th European, 2006, pp. 486-488.
- [14] I. Papapolymerou, R. Franklin Drayton, and L. P. B. Katehi, "Micromachined patch antennas," *Antennas and Propagation, IEEE Transactions on*, vol. 46, pp. 275-283, 1998.
- [15] G. P. Gauthier, A. Courtay, and G. M. Rebeiz, "Microstrip antennas on synthesized low dielectric-constant substrates," *Antennas and Propagation, IEEE Transactions on*, vol. 45, pp. 1310-1314, 1997.
- [16] L. Yoonjae, L. Xuesong, H. Yang, Y. Shoufeng, J. Evans, and C. G. Parini, "Low-Profile Directive Millimeter-Wave Antennas Using Free-Formed Three-Dimensional (3-D) Electromagnetic Bandgap Structures," *Antennas and Propagation, IEEE Transactions on*, vol. 57, pp. 2893-2903, 2009.
- [17] Y. Lee, X. Lu, Y. Hao, S. Yang, R. Uvic, J. R. G. Evans, and C. G. Parini, "Directive millimetre-wave antenna based on freeformed woodpile EBG structure," *Electronics Letters*, vol. 43, pp. 195-196, 2007.
- [18] R. Alkhatib and M. Drissi, "Improvement of bandwidth and efficiency for directive superstrate EBG antenna," *Electronics Letters*, vol. 43, pp. 702-703, 2007.
- [19] R. E. Jackson and R. Ramadoss, "MEMS Based Electrostatically Tunable Circular Microstrip Patch Antenna," in *Wireless and Microwave Technology Conference*, 2006. WAMICON '06. IEEE Annual, 2006, pp. 1-4.
- [20] L. Hyung Suk, K. Jeong-Geun, H. Songcheol, and Y. Jun-Bo, "Micromachined CPW-fed suspended patch antenna for 77 GHz automotive radar applications," in *Wireless Technology*, 2005. The European Conference on, 2005, pp. 249-252.
- [21] K. Jeong-Geun, L. Hyung Suk, L. Ho-Seon, Y. Jun-Bo, and S. Hong, "60-GHz CPW-fed post-supported patch antenna using micromachining technology," *Microwave and Wireless Components Letters, IEEE*, vol. 15, pp. 635-637, 2005.
- [22] B. Pan, Y. K. Yoon, G. E. Ponchak, M. G. Allen, J. Papapolymerou, and M. M. Tentzeris, "Analysis and Characterization of a High-Performance Ka-

References

- Band Surface Micromachined Elevated Patch Antenna," *Antennas and Wireless Propagation Letters, IEEE*, vol. 5, pp. 511-514, 2006.
- [23] Nicolas Tiercelin, Philippe Coquet, Ronan Sauleau, Vincent Senez, and H. Fujita, "Polydimethylsiloxane membranes for millimeter-wave planar ultra flexible antennas," *Journal of Micromechanics and Microengineering*, vol. 16, pp. 2389–2395, 2006.
- [24] Girish Kumar and K. Ray, *Broadband Microstrip Antennas: Artech House antennas and propagation library Inc.*, 2003.
- [25] L. Giauffret, J. Laheurte, and A. Papiernik, "Study of various shapes of the coupling slot in CPW-fed microstrip antennas," *IEEE Transition Antennas Propagation*, vol. 45, pp. 642-647, 1997.
- [26] J. Zhang, A. Wang, and P. Wang, "A Survey on reconfigurable antennas," in *Microwave and Millimeter Wave Technology, 2008. ICMMT 2008. International Conference on*, 2008, pp. 1156-1159.
- [27] D. Langoni, M. H. Weatherspoon, E. Ogunti, and S. Y. Foo, "An overview of reconfigurable antennas: Design, simulation, and optimization," in *Wireless and Microwave Technology Conference, 2009. WAMICON '09. IEEE 10th Annual*, 2009, pp. 1-5.
- [28] B. A. Cetiner, J. Y. Qian, H. P. Chang, M. Bachman, G. P. Li, and F. De Flaviis, "Monolithic integration of RF MEMS switches with a diversity antenna on PCB substrate," *Microwave Theory and Techniques, IEEE Transactions on*, vol. 51, pp. 332-335, 2003.
- [29] G. M. Rebeiz and J. B. Muldavin, "RF MEMS switches and switch circuits," *Microwave Magazine, IEEE*, vol. 2, pp. 59-71, 2001.
- [30] R. Maboudian and R. T. Howe, "Critical Review: Adhesion in surface micromechanical structures," *Journal of Vacuum Science & Technology B: Microelectronics and Nanometer Structures*, vol. 15, pp. 1-20, 1997.
- [31] N. Tas, T. Sonnenberg, H. Jansen, R. Legtenberg, and M. Elwenspoek, "Stiction in Surface Micromachining," *J. Micromech. Microeng.*, vol. 6, pp. 385-397, 1996.
- [32] L. Wu, V. Rochus, L. Noels, and J. C. Golinval, "Influence of adhesive rough surface contact on microswitches," *Journal of Applied Physics*, vol. 106, pp. 113502-113502-10, 2009.
- [33] W. Ling, V. Rochus, L. Noels, and J. C. Golinval, "Prediction of stiction in microswitch systems," in *Thermal, Mechanical & Multi-Physics Simulation, and Experiments in Microelectronics and Microsystems (EuroSimE), 2010 11th International Conference on*, pp. 1-4.

References

- [34] L. L. Mercado, S. M. Kuo, T. Y. T. Lee, and L. Lianjun, "Mechanics-based solutions to RF MEMS switch stiction problem," *Components and Packaging Technologies, IEEE Transactions on*, vol. 27, pp. 560-567, 2004.
- [35] J. S. Seybold, *Introduction to RF Propagation*: John Wiley & Sons, Inc., 2005.
- [36] Antti V. Raisanen and A. Lehto, *Radio Engineering for Wireless Communication and Sensor Applications*: Artech House, Inc., 2003.
- [37] W. Stutzman and G. Thiele, *Antenna Theory and Design*: John Wiley & Sons Inc, 1998.
- [38] C. A. Balanis, "Antenna theory: a review," *Proceedings of the IEEE*, vol. 80, pp. 7-23, 1992.
- [39] D. Pozar, *Microwave Engineering, Third Edition ed.*: John Wiley & Sons Inc, 2004.
- [40] C. Johnk, *Engineering Electromagnetic Fields and Waves*: John Wiley & Sons Inc, 1988.
- [41] John Kraus and R. Marhefka, *Antennas for All Applications*: McGraw-Hill, 1988.
- [42] D. M. Pozar, *Microwave and RF Design of Wireless Systems*: John Wiley & Sons, Inc., 2001.
- [43] "IEEE Standard Definitions of Terms for Antennas," *IEEE Std 145-1993*, p. i, 1993.
- [44] T. A. Milligan, *Modern Antenna Design, Second Edition ed.*: John Wiley & Sons, Inc., 2005.
- [45] K. Chang, *RF and Microwave Wireless Systems*: John Wiley & Sons, Inc., 2000.
- [46] A. Bensky, *Short-range Wireless Communication : Fundamentals of RF System Design and Application*: LLH Technology Publishing, 2000.
- [47] R. Munson, "Conformal microstrip antennas and microstrip phased arrays," *Antennas and Propagation, IEEE Transactions on*, vol. 22, pp. 74-78, 1974.
- [48] J. Howell, "Microstrip antennas," *Antennas and Propagation, IEEE Transactions on*, vol. 23, pp. 90-93, 1975.
- [49] D. M. Pozar, "Microstrip antennas," *Proceedings of the IEEE*, vol. 80, pp. 79-91, 1992.

References

- [50] F. K. Schwing, "Millimeter wave antennas," *Proceedings of the IEEE*, vol. 80, pp. 92-102, 1992.
- [51] Phillip Grajek, Bernhard Schoenlinner, and G. Rebeiz, "A 24-GHz High-Gain YagiUda Antenna Array," *IEEE Transactions on Antennas and Propagation*, vol. 52, 2004.
- [52] M. Kim, C. Cho, and J. KimA, "Dual Band Printed Dipole Antenna With Spiral Structure for WLAN Application," *IEEE Antenna and Wireless Propagation Letters*, vol. 15, 2005.
- [53] J. Jiao, G. Zhao, F. Zhang, H. Yuan, and Y. Jiao, "A Brodband CPW-Fed T-Shape Slot Antenna," *Progress In Electromagnetics Research, PIER* 76, 2007.
- [54] K. Yngvesson , T. Korzeniowski , Y. Kim, E. Kollberg, and J. Johansson, "The Tapered Slot Antenna: A New Integrated Element for Millimeter-Wave Application," *IEEE Transaction on Microwave Theory and Techniques*, vol. 37, 1989.
- [55] M. Weiss, "Microstrip Antennas for Millimeter Waves," *IEEE Transactions On Antennas And Propagation*, vol. AP-29, 1981.
- [56] R. N. Simons, *Coplanar Waveguide Circuits, Components, and Systems: John Wiley & Sons, Inc.*, 2001.
- [57] T. J. Ellis, J. P. Raskin, G. M. Rebeiz, and L. P. Katehi, "A wideband CPW-fed microstrip antenna at millimeter-wave frequencies," in *Antennas and Propagation Society International Symposium, 1999. IEEE, 1999*, pp. 1220-1223 vol.2.
- [58] R. W. Jackson, "Considerations in the Use of Coplanar Waveguide for Millimeter-Wave Integrated Circuits," *Microwave Theory and Techniques, IEEE Transactions on*, vol. 34, pp. 1450-1456, 1986.
- [59] K. Carver and J. Mink, "Microstrip antenna technology," *Antennas and Propagation, IEEE Transactions on*, vol. 29, pp. 2-24, 1981.
- [60] D. Sanchez-Hernandez and I. D. Robertson, "A Survey of Broadband Microstrip Patch Antennas," *Microwave Journal*, pp. 60-82, 1996.
- [61] K.-L. Wong, *Compact and Broadband Microstrip Antennas: John Wiley & Sons, Inc.*, 2002.
- [62] D. Jackson, J. Williams, A. Bhattacharyya, R. Smith, S. Buchheit, and S. Long, "Microstrip Patch Designs that do Not Excite Surface Waves," *IEEE Transactions on Antennas and Propagation*, vol. 41, p. 11, 1993.

References

- [63] G. Gauthier, A. Courtay, and G. M. Rebeiz, "Microstrip antennas on synthesized low dielectric-constant substrates," *IEEE Transition on Antennas and Propagation*, vol. 45, p. 3, 1997.
- [64] C. Cheype, C. Serier, M. Thevenot, T. Monediere, A. Reinix, and B. Jecko, "An electromagnetic bandgap resonator antenna," *IEEE Transition on Antennas and Propagation*, vol. 50, p. 5, 2002.
- [65] P. Bo, Y. Yoon, P. Kirby, J. Papapolymerou, M. M. Tenzeris, and M. Allen, "A W-band surface micromachined monopole for low-cost wireless communication systems," in *Microwave Symposium Digest, 2004 IEEE MTT-S International*, 2004, pp. 1935-1938 Vol.3.
- [66] K. Hettak, M. G. Stubbs, K. Elgaid, and G. Thayne, "Design and characterization of elevated CPW and thin film microstrip structures for millimeter-wave applications," in *Microwave Conference, 2005 European*, 2005, p. 4 pp.
- [67] W. S. T. Rowe and K. Ghorbani, "Millimetre-wave InP antenna for monolithic integration," *Electronics Letters*, vol. 42, pp. 733-734, 2006.
- [68] S. K. Koul, "Millimeter wave micromachined antenna development," in *Recent Advances in Microwave Theory and Applications, 2008. MICROWAVE 2008. International Conference on*, 2008, pp. 70-70.
- [69] S. E. Gunnarsson, N. Wadefalk, I. Angelov, H. Zirath, I. Kallfass, and A. Leuther, "A 220 GHz (G-Band) Microstrip MMIC Single-Ended Resistive Mixer," *Microwave and Wireless Components Letters, IEEE*, vol. 18, pp. 215-217, 2008.
- [70] W. Huei, L. Kun-You, T. Zuo-Min, L. Liang-Hung, L. Hsin-Chia, W. Chi-Hsueh, T. Jeng-Han, H. Tian-Wei, and L. Yi-Cheng, "MMICs in the millimeter-wave regime," *Microwave Magazine, IEEE*, vol. 10, pp. 99-117, 2009.
- [71] K. Elgaid and I. G. Thayne, "Monolithic Millimetrewave Integrated Circuits (MMICs) issues beyond 100GHz for High Resolution Imaging and Radar Applications," in *MM-Wave Products and Technologies, 2006. The Institution of Engineering and Technology Seminar on*, 2006, pp. 78-80.
- [72] I. J. Bahl and P. Bhartia, *Microstrip Antennas* Artech House, 1980.
- [73] Y. Lo, D. Solomon, and W. Richards, "Theory and experiment on microstrip antennas," *Antennas and Propagation, IEEE Transactions on*, vol. 27, pp. 137-145, 1979.

References

- [74] J. S. Row, "A simple impedance-matching technique for patch antennas fed by coplanar microstrip line," *Antennas and Propagation, IEEE Transactions on*, vol. 53, pp. 3389-3391, 2005.
- [75] D. Pozar, "Input impedance and mutual coupling of rectangular microstrip antennas," *Antennas and Propagation, IEEE Transactions on*, vol. 30, pp. 1191-1196, 1982.
- [76] L. I. Basilio, M. A. Khayat, J. T. Williams, and S. A. Long, "The dependence of the input impedance on feed position of probe and microstrip line-fed patch antennas," *Antennas and Propagation, IEEE Transactions on*, vol. 49, pp. 45-47, 2001.
- [77] M. Ramesh and Y. KB, "Design Formula for Inset Fed Microstrip Patch Antenna," *Journal of Microwaves and Optoelectronics*, vol. 3, pp. 5-7, December 2003.
- [78] K. Gupta and P. Hall, *Analysis and Design of Integrated Circuit - Antenna Modules*: John Wiley & Sons, Inc., 2000.
- [79] Ansoft, "<http://www.ansoft.com/products/hf/hfss/>," 2010.
- [80] Ansoft, *Advanced Notes-High Frequency Structure Simulator*, 2007.
- [81] P. R. Young, D. S. McPherson, C. Chrisostomidis, K. Elgaid, I. G. Thayne, S. Lucyszyn, and I. D. Robertson, "Accurate non-uniform transmission line model and its application to the de-embedding of on-wafer measurements," *Microwaves, Antennas and Propagation, IEE Proceedings -*, vol. 148, pp. 153-156, 2001.
- [82] S. E. Gunnarsson, "Mixers and Multifunctional MMICs for Millimeter-Wave Applications," in *Department of Microtechnology and Nanoscience – MC2*. vol. PhD: Chalmers University of Technology, 2008.
- [83] R. C. Jaeger, *Introduction to Microelectronic Fabrication*: Prentice Hall Publishing Co, 2002.
- [84] A. K. Wong, "Microlithography: trends, challenges, solutions, and their impact on design," *Micro, IEEE*, vol. 23, pp. 12-21, 2003.
- [85] Serope Kalpakjian and S. R. Schmid, *Manufacturing Engineering and Technology*: Prentice Hall Publishing Co, 2006.
- [86] P. J. Silverman, "Extreme ultraviolet lithography: overview and development status," *Journal of Microlithography, Microfabrication, and Microsystems*, vol. 4, p. 011006, 2005.

References

- [87] Mark A. McCord and M. J. Rooks, Handbook of Microlithography, Micromachining and Microfabrication vol. 1: SPIE- the International Society for Optical Engineering, 1997.
- [88] S. Thomas and D. Macintyre, "Electronic Beam Lithography Course," James Watt Nanofabrication Centre (JWNC), University of Glasgow, 2008.
- [89] A. A. Tseng, C. Kuan, C. D. Chen, and K. J. Ma, "Electron beam lithography in nanoscale fabrication: recent development," Electronics Packaging Manufacturing, IEEE Transactions on, vol. 26, pp. 141-149, 2003.
- [90] S. Thoms, "BELLE - beamwriter exposure layout for lithographic engineers," University of Glasgow, 2009.
- [91] S. Bentley, "The Development of Sub-25 nm III-V High Electron Mobility Transistors." vol. PhD: University of Glasgow 2009.
- [92] E. Reichmanis and A. E. Novembre, "Lithographic resist materials chemistry," Annual Reviews Inc, vol. 23, pp. 11-43, 1993.
- [93] T. Yamaguchi and H. Namatsu, "Effect of developer molecular size on roughness of dissolution front in electron-beam resist," Journal of Vacuum Science & Technology B: Microelectronics and Nanometer Structures, vol. 22, pp. 1037-1043, 2004.
- [94] R. Tiron, L. Mollard, O. Louveau, and E. Lajoinie, "Ultrahigh-resolution pattern using electron-beam lithography HF wet etching," Journal of Vacuum Science & Technology B: Microelectronics and Nanometer Structures, vol. 25, pp. 1147-1151, 2007.
- [95] K. I. Elgaid, "A ka-band GaAs MESFET Monolithic Downconverter." vol. PhD: University of Glasgow, 1998.
- [96] Y. Konaka and M. G. Allen, "Single- and multi-layer electroplated microaccelerometers," in Micro Electro Mechanical Systems, 1996, MEMS '96, Proceedings. 'An Investigation of Micro Structures, Sensors, Actuators, Machines and Systems'. IEEE, The Ninth Annual International Workshop on, 1996, pp. 168-173.
- [97] T. A. Green, "Gold Electrodeposition for Microelectronic, Optoelectronic and Microsystem Applications," Gold Bulletin, vol. 40, p. 10, 2007.
- [98] Y. Okinaka, "Some Recent Topics in Gold Plating for Electronics Applications," Gold Bulletin, vol. 31, p. 10, 1998.
- [99] S. Ferguson, "Airbridge Fabrication Process Notes," James Watt Nanofabrication Centre (JWNC), University of Glasgow, 2006.

References

- [100] S. Sangsub, K. Youngmin, M. Jimin, L. Heeseok, K. Youngwoo, and S. Kwang-Seok, "A Millimeter-Wave System-on-Package Technology Using a Thin-Film Substrate With a Flip-Chip Interconnection," *Advanced Packaging, IEEE Transactions on*, vol. 32, pp. 101-108, 2009.
- [101] P. Sewell and T. Rozzi, "Characterization of air-bridges in MM-wave coplanar waveguide using the complete mode spectrum of CPW," *Microwave Theory and Techniques, IEEE Transactions on*, vol. 42, pp. 2078-2086, 1994.
- [102] K. Beilenhoff and W. Heinrich, "Excitation of the Parasitic Parallel-Plate Line Mode at Coplanar Discontinuities," in *ARFTG Conference Digest-Spring*, 49th, 1997, pp. 244-247.
- [103] A. Reichelt and I. Wolff, "New coplanar-like transmission lines for application in monolithic integrated millimeter-wave and submillimeter-wave circuits," in *Microwave Symposium Digest, 1998 IEEE MTT-S International*, 1998, pp. 99-102 vol.1.
- [104] F. Schnieder, R. Doerner, and W. Heinrich, "High-impedance coplanar waveguides with low attenuation," *Microwave and Guided Wave Letters, IEEE*, vol. 6, pp. 117-119, 1996.
- [105] S. Kanthamani, S. Raju, N. Dhamodharan, and K. S. Chidambaram, "Characterization of elevated CPW on different substrates for high speed digital interconnects," in *Recent Advances in Microwave Theory and Applications, 2008. MICROWAVE 2008. International Conference on*, 2008, pp. 754-756.
- [106] D. M. Pozar and B. Kaufman, "Increasing the bandwidth of a microstrip antenna by proximity coupling," *Electronics Letters*, vol. 23, pp. 368-369, 1987.
- [107] L. Giauffret, J. M. Laheurte, and A. Papiernik, "Study of various shapes of the coupling slot in CPW-fed microstrip antennas," *Antennas and Propagation, IEEE Transactions on*, vol. 45, pp. 642-647, 1997.
- [108] J. Kiriazi, H. Ghali, H. Ragaie, and H. Haddara, "Reconfigurable dual-band dipole antenna on silicon using series MEMS switches," in *Antennas and Propagation Society International Symposium, 2003. IEEE*, 2003, pp. 403-406 vol.1.
- [109] W. H. Weedon, W. J. Payne, and G. M. Rebeiz, "MEMS-switched reconfigurable antennas," in *Antennas and Propagation Society International Symposium, 2001. IEEE*, 2001, pp. 654-657 vol.3.
- [110] R. N. Simons, C. Donghoon, and L. P. B. Katehi, "Polarization reconfigurable patch antenna using microelectromechanical systems (MEMS)

References

- actuators," in Antennas and Propagation Society International Symposium, 2002. IEEE, 2002, pp. 6-9 vol.2.
- [111] C. Yibo, L. Xufeng, J. Yongchang, and Z. Fushun, "A frequency reconfigurable slot antenna," in Microwave, Antenna, Propagation and EMC Technologies for Wireless Communications, 2007 International Symposium on, 2007, pp. 516-518.
- [112] V. K. Varadan, K. J. Vinoy, and K. A. Jose, RF MEMS and Their Applications: John Wiley & Sons Ltd, 2003.
- [113] Duixian Liu, Brain Gaucher, Ullrich Pfeiffer, and J. Grzyb, Advanced Millimeter-wave Technologies: Antennas, Packaging and Circuit: John Wiley and Sons, Ltd, Publication, 2009.
- [114] S. Lucyszyn, "Review of radio frequency microelectromechanical systems technology," Science, Measurement and Technology, IEE Proceedings -, vol. 151, pp. 93-103, 2004.
- [115] G. M. Rebeiz, RF MEMS-Theory, design and technology: John Wiley & Sons 2003.
- [116] L. P. B. Katehi, J. F. Harvey, and E. Brown, "MEMS and Si micromachined circuits for high-frequency applications," Microwave Theory and Techniques, IEEE Transactions on, vol. 50, pp. 858-866, 2002.
- [117] A. Q. Liu, RF MEMS Switches and Integrated Switching Circuits: Design, Fabrication, and Test: Springer Science and Business Media, 2010.
- [118] A. A. Fomani, S. Fouladi, and R. R. Mansour, "Magnetically-actuated dielectric cantilever RF MEMS switches," in Microwave Symposium Digest (MTT), 2010 IEEE MTT-S International, pp. 296-299.
- [119] Y. Yashchyshyn, "Reconfigurable antennas by RF switches technology," in Perspective Technologies and Methods in MEMS Design, 2009. MEMSTECH 2009. 2009 5th International Conference on, 2009, pp. 155-157.
- [120] G. Yanjue, W. Ping, Z. Fu, L. Liang, Z. Li, and M. Chunling, "Analysis and simulation of RF MEMS switch," in Antennas, Propagation and EM Theory, 2008. ISAPE 2008. 8th International Symposium on, 2008, pp. 1482-1485.
- [121] L. Vietzorreck, "Modeling of the millimeter-wave behavior of MEMS capacitive switches," in Microwave Symposium Digest, 1999 IEEE MTT-S International, 1999, pp. 1685-1688 vol.4.

References

- [122] J. Y. Park, G. H. Kim, K. W. Chung, and J. U. Bu, "Electroplated rf MEMS capacitive switches," in *Micro Electro Mechanical Systems, 2000. MEMS 2000. The Thirteenth Annual International Conference on, 2000*, pp. 639-644.
- [123] J. J. Yao and M. F. Chang, "A Surface Micromachined Miniature Switch For Telecommunications Applications With Signal Frequencies From DC Up To 4 Ghz," in *Solid-State Sensors and Actuators, 1995 and Eurosensors IX.. Transducers '95. The 8th International Conference on, 1995*, pp. 384-387.
- [124] David Becher, Richard Chan, Michael Hattendorf, and M. Feng, "Reliability Study of Low-Voltage RF MEMS Switches," in *GaAs Mantech Conference San Diego, CA, 2002*, pp. 54-57.
- [125] H. U. Rahman, T. Hesketh, and R. Ramer, "Low actuation voltage RF MEMS series switch with novel beam design," in *Emerging Technologies, 2008. ICET 2008. 4th International Conference on, 2008*, pp. 116-119.
- [126] D. Peroulis, S. P. Pacheco, K. Sarabandi, and L. P. B. Katehi, "Electromechanical considerations in developing low-voltage RF MEMS switches," *Microwave Theory and Techniques, IEEE Transactions on*, vol. 51, pp. 259-270, 2003.
- [127] J. B. Muldavin and G. M. Rebeiz, "High-isolation CPW MEMS shunt switches. 2. Design," *Microwave Theory and Techniques, IEEE Transactions on*, vol. 48, pp. 1053-1056, 2000.
- [128] S. Patton and J. Zabinski, "Fundamental studies of Au contacts in MEMS RF switches," *Tribology Letters*, vol. 18, pp. 215-230, Feb. 2005.
- [129] G. M. Rebeiz, "RF MEMS switches: status of the technology," in *TRANSDUCERS, Solid-State Sensors, Actuators and Microsystems, 12th International Conference on, 2003, 2003*, pp. 1726-1729 vol.2.
- [130] S. P. Pacheco, L. P. B. Katehi, and C. T. C. Nguyen, "Design of low actuation voltage RF MEMS switch," in *Microwave Symposium Digest., 2000 IEEE MTT-S International, 2000*, pp. 165-168 vol.1.
- [131] L. C. Kretly, A. A. S. Tavora, and C. E. Capovilla, "MEMS switch for wireless communication circuits: fabrication process and simulation," in *Microwave and Optoelectronics, 2005 SBMO/IEEE MTT-S International Conference on, 2005*, pp. 427-429.
- [132] S. Simion, "Modeling and design aspects of the MEMS switch," in *Semiconductor Conference, 2003. CAS 2003. International, 2003*, p. 128 Vol. 1.
- [133] L. Liang, D. Zhongliang, Z. Fu, L. Yude, and H. Ke, "Analysis and simulation of RF MEMS switch for wireless communication," in

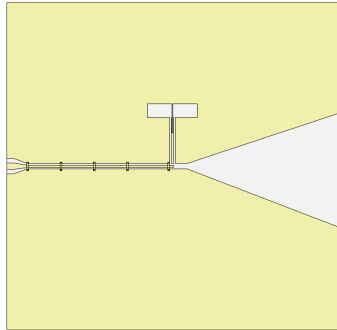
References

- Communications and Information Technology, 2005. ISGIT 2005. IEEE International Symposium on, 2005, pp. 1132-1135.
- [134] L. X. Zhang and Y.-P. Zhao, "Electromechanical model of RF MEMS switches," *Microsystem Technologies*, Springer-Verlag vol. 9 pp. 420-426.
- [135] J. B. Muldavin and G. M. Rebeiz, "High-isolation CPW MEMS shunt switches. 1. Modeling," *Microwave Theory and Techniques, IEEE Transactions on*, vol. 48, pp. 1045-1052, 2000.
- [136] W. Robert Ashurst, M. P. de Boer, C. Carraro, and R. Maboudian, "An investigation of sidewall adhesion in MEMS," *Applied Surface Science*, vol. 212-213, pp. 735-741, 2003.
- [137] A. Hariri, J. Zu, and R. B. Mrad, "Modeling of Wet Stiction in Microelectromechanical Systems (MEMS)," *Microelectromechanical Systems, Journal of*, vol. 16, pp. 1276-1285, 2007.
- [138] Roya Maboudian, W. R. Ashurst, and C. Carraro, "Tribological challenges in micromechanical systems," *SpringerLink, Tribology Letters* vol. 12, pp. 95-100, 2002.
- [139] R. Maboudian, "Surface processes in MEMS technology," *Surface Science Reports*, vol. 30, pp. 207-269, 1998.
- [140] T. Yamashita, T. Itoh, and T. Suga, "Investigation of Anti-Stiction Coating for MEMS Switch using Atomic Force Microscope," in *Solid-State Sensors, Actuators and Microsystems Conference, 2007. TRANSDUCERS 2007. International*, 2007, pp. 1657-1660.
- [141] S. Zhaohui, L. Yinghong, and C. Wei, "Reconfigurable multiple-band antenna using switches," in *Antennas, Propagation and EM Theory, 2008. ISAPE 2008. 8th International Symposium on*, 2008, pp. 316-319.
- [142] N. Kingsley, D. E. Anagnostou, M. Tentzeris, and J. Papapolymerou, "RF MEMS Sequentially Reconfigurable Sierpinski Antenna on a Flexible Organic Substrate With Novel DC-Biasing Technique," *Microelectromechanical Systems, Journal of*, vol. 16, pp. 1185-1192, 2007.
- [143] P. Arcioni, L. Perregriani, and G. Conciauro, "A novel low reflection-loss MEMS reconfigurable patch antenna," in *Microwave Conference, 2007. European*, 2007, pp. 1015-1018.
- [144] S. L. S. Yang, A. A. Kishk, and L. Kai-Fong, "Frequency Reconfigurable U-Slot Microstrip Patch Antenna," *Antennas and Wireless Propagation Letters, IEEE*, vol. 7, pp. 127-129, 2008.

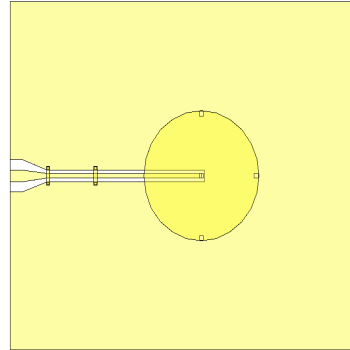
References

- [145] Y. Fan and Y. Rahmat-Samii, "Patch antenna with switchable slots (PASS): reconfigurable design for wireless communications," in *Antennas and Propagation Society International Symposium, 2002. IEEE, 2002*, pp. 462-465 vol.1.
- [146] E. Erdil, K. Topalli, O. A. Civi, and T. Akin, "Reconfigurable CPW-fed dual-frequency rectangular slot antenna using RF MEMS technology," in *Antennas and Propagation Society International Symposium, 2005 IEEE, 2005*, pp. 392-395 vol. 2A.
- [147] R. N. Simons, C. Donghoon, and L. P. B. Katehi, "Reconfigurable array antenna using microelectromechanical systems (MEMS) actuators," in *Antennas and Propagation Society International Symposium, 2001. IEEE, 2001*, pp. 674-677 vol.3.

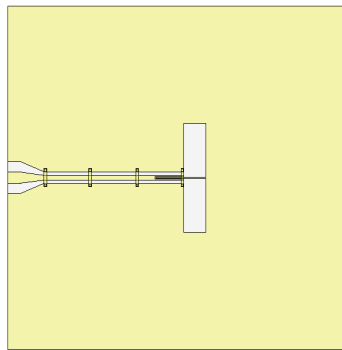
Appendix A



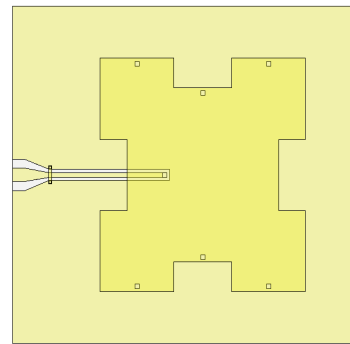
Tapered antenna



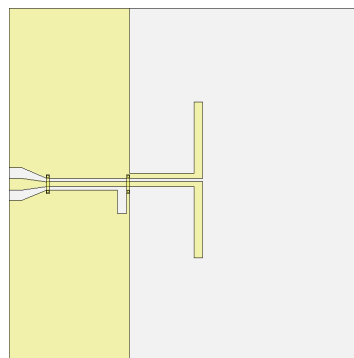
Elevated circular patch antenna



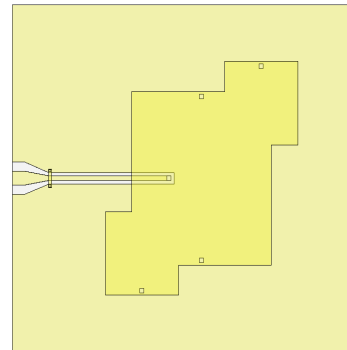
Slot antenna



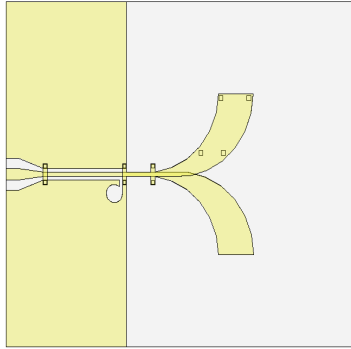
CPW fed notched patch antenna



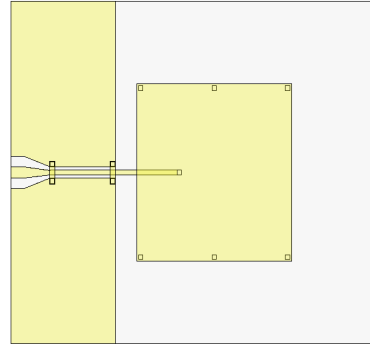
Printed dipole antenna



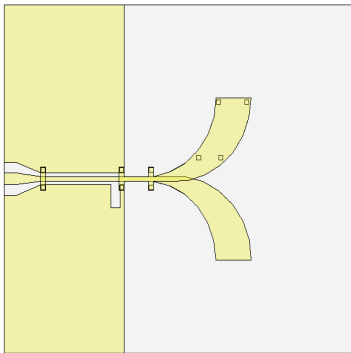
Elevated patch antenna



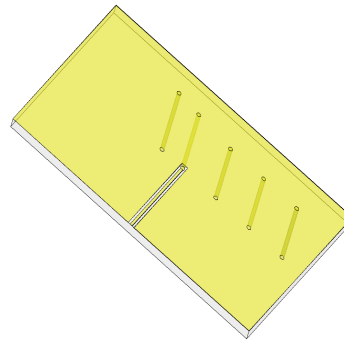
Elevated Vivaldi antenna with circular transition



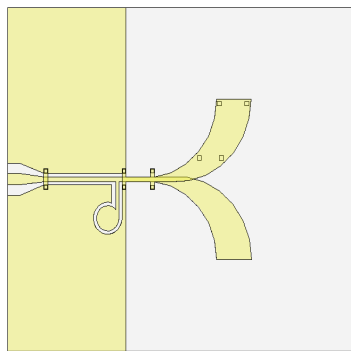
Monopole elevated patch antenna



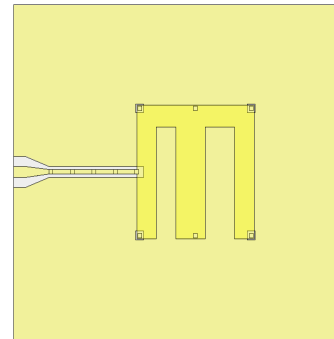
Elevated Vivaldi antenna with rectangular transition



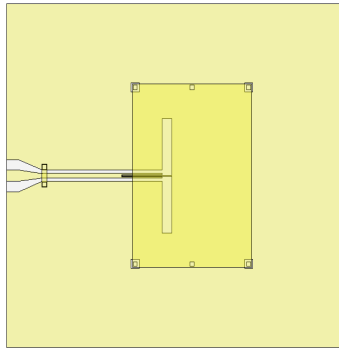
Elevated Yagi-uda antenna



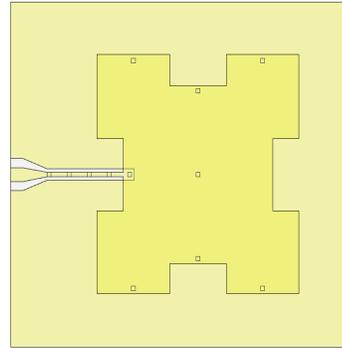
Elevated Vivaldi antenna with ring transition



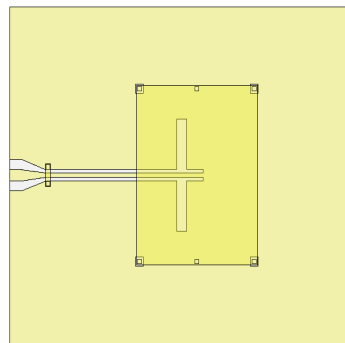
Elevated E-shape antenna



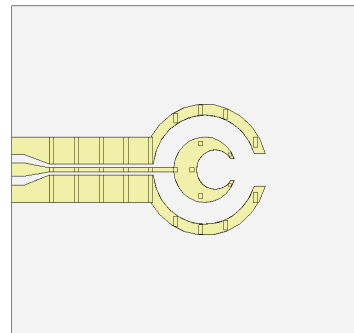
Approximately coupled antenna



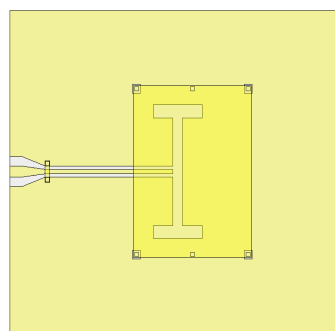
EC-CPW fed notched patch antenna



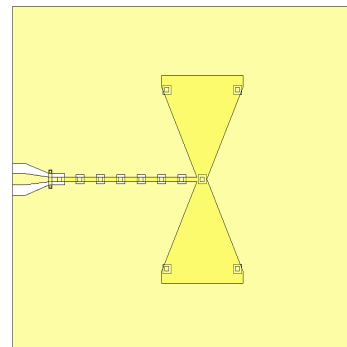
Approximately coupled antenna



Crescent elevated antenna

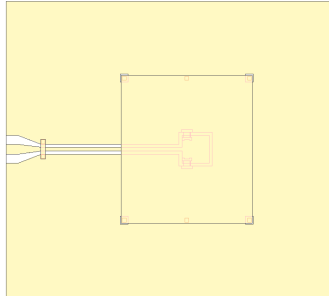


Approximately coupled antenna

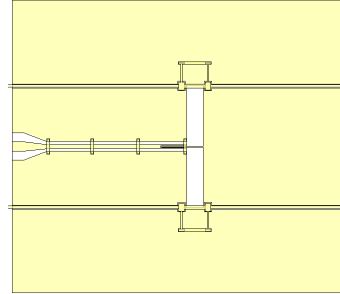


Elevated microstrip line feed elevated bowtie dipole antenna

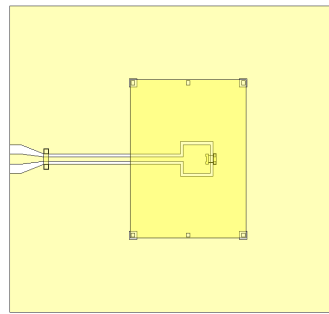
Appendix B



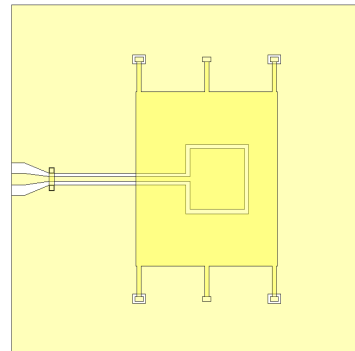
Reconfigurable elevated patch antenna using
two switches



Reconfigurable slot antenna



Reconfigurable elevated patch antenna using
one switch



Reconfigurable patch antenna without switch